NASA/TM–2013–216604

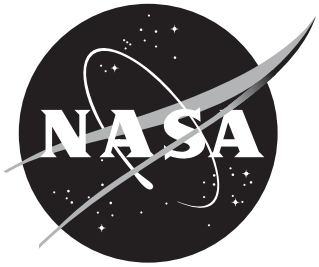

Experimental Database with Baseline CFD Solutions: 2-D and Axisymmetric Hypersonic Shock-Wave/Turbulent-Boundary-Layer Interactions

Joseph G. Marvin
ERC-Ames Research Center, Moffett Field, CA

James L. Brown
NASA Ames Research Center, Moffett Field, CA

Peter A. Gnoffo,
NASA Langley Research Center, Moffett Field, CA

November 2013

NASA STI Program ... in Profile

Since its founding, NASA has been dedicated to the advancement of aeronautics and space science. The NASA scientific and technical information (STI) program plays a key part in helping NASA maintain this important role.

The NASA STI Program operates under the auspices of the Agency Chief Information Officer. It collects, organizes, provides for archiving, and disseminates NASA's STI. The NASA STI Program provides access to the NASA Aeronautics and Space Database and its public interface, the NASA Technical Report Server, thus providing one of the largest collection of aeronautical and space science STI in the world. Results are published in both non-NASA channels and by NASA in the NASA STI Report Series, which includes the following report types:

- TECHNICAL PUBLICATION. Reports of completed research or a major significant phase of research that present the results of NASA programs and include extensive data or theoretical analysis. Includes compilations of significant scientific and technical data and information deemed to be of continuing reference value. NASA counterpart of peer-reviewed formal professional papers, but having less stringent limitations on manuscript length and extent of graphic presentations.
- TECHNICAL MEMORANDUM. Scientific and technical findings that are preliminary or of specialized interest, e.g., quick release reports, working papers, and bibliographies that contain minimal annotation. Does not contain extensive analysis.
- CONTRACTOR REPORT. Scientific and technical findings by NASA-sponsored contractors and grantees.
- CONFERENCE PUBLICATION. Collected papers from scientific and technical conferences, symposia, seminars, or other meetings sponsored or co-sponsored by NASA.
- SPECIAL PUBLICATION. Scientific, technical, or historical information from NASA programs, projects, and missions, often concerned with subjects having substantial public interest.
- TECHNICAL TRANSLATION. English- language translations of foreign scientific and technical material pertinent to NASA's mission.

Specialized services also include creating custom thesauri, building customized databases, and organizing and publishing research results.

For more information about the NASA STI Program, see the following:

- Access the NASA STI program home page at ***http://www.sti.nasa.gov***
- E-mail your question via the Internet to help@sti.nasa.gov
- Fax your question to the NASA STI Help Desk at 443-757-5803
- Phone the NASA STI Help Desk at 443-757-5802
- Write to:
  NASA STI Help Desk
  NASA Center for AeroSpace Information
  7115 Standard Drive
  Hanover, MD 21076–1320

NASA/TM–2013–216604

Experimental Database with Baseline CFD Solutions: 2-D and Axisymmetric Hypersonic Shock-Wave/Turbulent-Boundary-Layer Interactions

Joseph G. Marvin
ERC-Ames Research Center, Moffett Field, CA

James L. Brown
NASA Ames Research Center, Moffett Field, CA

Peter A. Gnoffo,
NASA Langley Research Center, Moffett Field, CA

National Aeronautics and
Space Administration

Ames Research Center
Moffett Field, CA 94035-1000

November 2013

Acknowledgments

This work was sponsored by NASA's Fundamental Aeronautics Hypersonics (FAH) and Hypersonic Entry Descent and Landing (HEDL/STMD) projects.

The interest, leadership and support of Dr. Deepak Bose (Associate Project Investigator, Hypersonics) and of Dr. Michael J. Wright (Project Manager, HEDL) are gratefully acknowledged. The authors acknowledge Dr.'s E. Schülein, R. Hillier, N. Murray, S. Willams and M. Holden for their kind permission to permit inclusion of their data in this document. We also acknowledge D. Prabhu for permission to use portions of his CFD HiFire simulation, and M. Olsen for permission to use his adapted grid for the Kussoy-Horstman cylinder/flare case.

Should the reader choose to use data extracted from this database, this database report and the original source documents reporting the experiment should be cited.

Available from:

NASA Center for AeroSpace Information
7115 Standard Drive
Hanover, MD 21076-1320
443-757-5802

NASA TM-2013-216604

Experimental Database with Baseline CFD Solutions: 2-D and Axisymmetric Hypersonic Shock-Wave/Turbulent-Boundary-Layer Interactions

Joseph G. Marvin, *ERC-Ames Research Center*
James L. Brown, PhD, *NASA-Ames Research Center*
Peter A. Gnoffo, PhD, *NASA-Langley Research Center*

November 2013

Summary

A database compilation of hypersonic shock-wave/turbulent boundary layer experiments is provided. The experiments selected for the database are either 2D or axisymmetric, and include both compression corner and impinging type SWTBL interactions. The strength of the interactions range from attached to incipient separation to fully separated flows. The experiments were chosen based on criterion to ensure quality of the datasets, to be relevant to NASA's missions and to be useful for validation and uncertainty assessment of CFD Navier-Stokes predictive methods, both now and in the future. An emphasis on datasets selected was on surface pressures and surface heating throughout the interaction, but include some wall shear stress distributions and flowfield profiles. Included, for selected cases, are example CFD grids and setup information, along with surface pressure and wall heating results from simulations using current NASA real-gas Navier-Stokes codes by which future CFD investigators can compare and evaluate physics modeling improvements and validation and uncertainty assessments of future CFD code developments. The experimental database is presented tabulated in the Appendices describing each experiment. The database is also provided in computer-readable ASCII files located on a companion DVD. For selected cases, included on the companion DVD are example CFD grids and wall pressure and heating CFD results, and PDF files of NASA source documents.

Introduction

NASA's Hypersonics Uncertainty working group, tasked by the Fundamental Aerodynamics Program, recently completed an initial assessment of current hypersonic aerothermodynamics prediction capability for NASA mission relevant problems (Ref. 1). Part of that study consisted of examining the predictive capabilities of NASA's state-of-the-art aerothermodynamics real-gas Navier-Stokes codes applied to existing unit physics shock-wave/turbulent-boundary-layer interaction experiments relevant to scramjet design. In particular, geometries generating either 2D or axisymmetric, impinging or compression corner shock waves, which then interact with fully developed turbulent boundary layer flows, including those leading to separation, were studied (Refs. 2 and 3). Uncertainty measures were determined by comparing aspects of the numerical simulations from state-of-the-art computer codes with experimental data.

The working group conducted an extensive search for suitable hypersonic SWTBLI experiments. This search consisted of examination of existing experimental database sources, which covered earlier time periods, followed by a literature search for more recent experiments. The first source was the NASA-funded Penn State University compilation (reported in Ref. 4, with the complete database in Ref. 5), covering the time period prior to 1994, of supersonic and hypersonic data. In Reference 4, eight necessary and five desirable criteria for selecting the experiments were recommended. The necessary criteria, still relevant today, are: *1) baseline*

applicability, 2) simplicity, 3) specific applicability, 4) well defined experimental error bounds, 6) consistency, 7) adequate documentation of data, and 8) adequate spatial resolution of data. The database included five experiments conducted at hypersonic conditions. The Settles and Dodson database was compiled on now-outdated floppy-disk digital format. Another source was the Roy and Blottner (Ref. 6) study of hypersonic flow modeling that summarized the Settles and Dodson experimental database, but also identified a few additional ones. Next, European sources (Refs. 7-11) were identified that provided more recent data. The final source was from updated CUBRC SWBLI experimental data provided to NASA by Dr. M. Holden and summarized in Ref. 12. All of these experiments were performed in ground-based facilities and meet the Settles and Dodson criteria mentioned above. After reviewing these data sources, the uncertainty studies focused on a portion of the database in order to meet computational resource and individual time constraints. A specific shortcoming, which should be addressed in the future, in the hypersonic experimental database, is a lack of real-gas/dissociating data at flight relevant enthalpies.

The primary purpose of this document, then, is to compile this hypersonic SWTBLI database in one resource so as to facilitate future assessments of computer code development and physics modeling improvements. There are good reasons for compiling this foundational database into a single resource: for example, the Settles and Dodson SWBLI database, although providing several good hypersonic cases, are stored on outdated floppy disks that take specialized reading procedures and the updated CUBRC data replace some of the cases in their compilation; the new data sources are contained in thesis documents that are difficult to obtain and not digitized; and finally, the cases have all had computations attempted thereby establishing that input and boundary conditions are unambiguous.

Reynolds Averaged Navier-Stokes computations made during and subsequent to NASA's uncertainty studies are also included in order to facilitate future CFD assessments and provide a baseline for future comparisons. The provided computations include input and boundary conditions, grids, and reference baseline turbulence model descriptions and code implementations. All of this information is compiled on a DVD to make setting up future studies easier, and to provide a consistent basis for comparison with current CFD status.

General Description of the Validation Database

Table 1 summarizes the database and relevant measurements. In all cases the test Reynolds number was sufficiently high to preclude any necessity of boundary layer tripping and resulted in fully developed turbulent flows ahead of the location of the interaction. A brief description of the experiments is given as an introduction to more detailed and relevant information that follows.

2D Compression Corner:

Two sets of experimental data for two-dimensional geometries are listed. The first set of experiments were performed by Coleman and co-workers (Refs. 13-15) at M= 9 in a gun tunnel with Nitrogen (N_2) as the flow medium. Various ramp angles were employed to gather data from incipient to fully separated flow. In addition to surface pressures and heat transfer through the interaction, velocity profile data were obtained on the flat plate. The data herein were taken directly from Settles and Dodson (Ref. 5).

Holden (Ref. 12) provided a second set of experimental data to NASA with recently recommended data from CUBRC. A series of tests at M=8.2 were performed in a shock tunnel in air wherein the ramp angle was varied. The data taken at M=11.3 provided a case of separated flow. In addition, a flat plate velocity profile was provided at M=11.3.

Axisymmetric Cone-Cylinder-Flare:

The Kussoy and Horstman experiment (Ref. 16) was vetted and added to the Settles and Dodson database. The data herein were taken from Ref. 5. The tests were performed at M= 7 in a blow-down wind tunnel in air heated to prevent liquefaction in the test section. The forebody on the cylinder is a 10 degree cone adapted to the cylinder by a circular arc fairing. Various flares were used to provide data on incipient to fully separated flow. Since the experimental geometry is axisymmetric there are minimal issues of possible 3-D effects. Pressure, heat transfer and boundary layer profiles were measured ahead and along one flared section.

Holden (Ref. 12) provided NASA with experimental data taken on the HiFire configuration, a cone-cylinder-flare. These ground-based data were taken at M=7.19 and prior to flight tests of the HiFire flight vehicle. The geometry was a 7 degree cone followed by a cylindrical section and terminated with a 33 degree short flare. Since the experimental geometry is axisymmetric there are minimal issues with 3-D effects. Pressure, heat transfer and skin friction were measured.

Axisymmetric Hollow-Cylinder-Flare:

Williams performed an experiment using a hollow-cylinder-flare geometry in the Imperial College gun tunnel at M= 9. Nitrogen (N_2) was used as the test gas. The results were first reported in his Ph.D. Thesis (Ref. 9) and later by Murray, et al. in Ref. 8. The cylindrical section was located near the nozzle exit and its diameter was sufficient to swallow the oncoming flow resulting in a significant high Reynolds number turbulent flow over the cylinder's exterior. Since the experimental geometry is axisymmetric there are minimal issues with 3-D effects. Surface pressures and heat transfer were measured over the cylinder and the 36-degree flare. Separated flow existed near the junction of the cylinder and flare.

Axisymmetric Cone-Flare:
Experiments on a large cone-flare geometry were performed in a CUBRC shock tunnel and reported by Holden (Refs. 12, and 17-19). Pressure and heating rate distributions along the cone and the flare were measured at Mach 11 and 13 at very high Reynolds numbers and some boundary layer profile data were obtained at the junction of the cone and flare. Two test cases for a 6 degree cone, fitted with flares of 30 and 36 degrees, were vetted by Settles and Dodson and accepted in their original database (Ref. 5). This experiment was re-examined by Holden (Ref. 12). He provided updated information as to test conditions, geometry and tabulated data for the 36 degree flare case at M=11 to NASA (Ref. 2). These latter data are included herein.

2D Impinging Shock Wave on a Flat Plate:
Three separate experiments are listed for incident shock waves impinging on a flat plate. Pressures and heating rates along with some boundary layer profiles are provided. The Kussoy and Horstman experiment (Ref. 20) was performed in a blowdown wind tunnel at M = 8 using air heated sufficiently to prevent liquefaction in the test section. The Holden experiment (Ref. 12) was performed in a shock tunnel at Mach = 11. The Schülein experiment (Ref. 7) was performed in a Ludwieg tube wind tunnel at Mach=5. In all cases run time was sufficient to establish steady flow.

Axisymmetric Impinging-Shock on Hollow Centerbody:
This experiment was carried out by Murray (Ref. 10) at M=9 in a gun tunnel using Nitrogen (N_2) as the test gas. See also Ref. 8. Using the hollow cylinder that swallowed the oncoming flow provided an analogous case to the impinging shock wave on a flat plate described above, but with the added potential of elimination of undesirable 3-dimensional effects. For the high Reynolds number conditions of this experiment, obtained by using a long centerbody, there exists a mild axial pressure gradient within the test section that needs to be taken into account when performing numerical simulations. A careful calibration of the facility was carried out by Mallinson et al. (Ref. 11) and provides means to account for this gradient. For example, Brown (Ref. 3) used the calibration data to generate a radial free stream boundary condition for his simulations. Other means can be found in Ref. 10.

General Description of Computer Codes

Baseline computations using state-of-the art NASA production computer codes will be presented later to facilitate future code and model development. In the spirit of production code implementation, these computations include the complete geometry and include boundary layer transition zones. A brief description of the codes follows.

DPLR Code

The DPLR (Data-Parallel Line Relaxation) code, one of several NASA hypersonic aerothermodynamics production codes, is used in the later Appendices to provide baseline computations. It is a three-dimensional (3D) implicit finite-volume, structured-block real-gas Navier-Stokes code that incorporates non-equilibrium finite-rate gas chemistry, modified Steger-Warming flux splitting with upwind Jacobians and higher-order spatial differencing. An extensive set of gas chemistry options is available, including options for single- and multiple-temperatures, various gas-diffusion modeling for mixtures of reacting gases, including those suitable for the atmospheres of several atmospheric planetary bodies, but also that of perfect gases of various composition. Several turbulence models with compressibility modification appropriate to hypersonic flows are available as options, including the Baldwin-Lomax, the SST, the Wilcox K-Omega and the Spalart-Allmaras turbulence models. Details of model implementation are discussed in Ref. 3. The location of transition to turbulence can be specified. More details can be found in the DPLR users manual, Ref. 21.

LAURA Code

The LAURA Code is another of NASA's hypersonic aerothermodynamics production codes used in the later Appendices to provide baseline computations. It is a finite volume, structured, multi-block, computational Navier-Stokes code for three-dimensional, viscous, compressible flows. It is capable of handling perfect and real gas chemistry, single and multi-equation eddy viscosity turbulence models including compressibility, ablation and radiation. Turbulence models include Baldwin-Lomax, Cebeci-Smith, Spalart-Allmaras 1-equation, Menter 2-equation, Menter-SST 2-equation, and Wilcox k-omega 2 equation models. Details of model implementation can be found in Ref. 2. The location of transition to turbulence can be specified. More details can be found in the LAURA users manual, Ref. 22.

Database and Baseline Computations

Data selected from each of the experiments listed in Table 1 and organized by flow topology are presented in a separate Appendix for each experiment. In each case the data are tabulated in measuring units consistent with those provided in the original reference document. For each such experiment, a general description, experimental arrangement, facility characteristics, measurements with accuracy estimates, and data tables are provided. In this way, users will be able to access one resource to obtain all the pertinent information needed to undertake their own computations. Users are strongly encouraged to consult the original references for more detail on what was measured and how it was accomplished. Together, the selected experiments provide a comprehensive set of data for each flow topology in answer to the belief that no single experiment should be used to evaluate code development. Whenever available, upstream, undisturbed data are also tabulated.

Following the data tables, RANS computations for selected cases are provided as a baseline from which to measure future improvements that, for example, might include consideration of flow unsteadiness or modeling approaches combining Large Eddy Simulation and RANS. The majority of these RANS computations were used in NASA's uncertainty studies (Ref. 1, 2 and 3). Additional simulations performed subsequent to the published uncertainty studies are also provided by the second author, J. L. Brown, with one further simulation by D. Prabhu.

The experimental dataset, CFD solutions, and CFD grids described in the Appendices are also tabulated in computer-readable ASCII files on a DVD released along with this report. In addition, the complete Settles and Dodson database is included as a separate folder in the DVD as a replacement inasmuch as it was released on a floppy disc media that is difficult to read with currently available computers.

Concluding Remarks

Experimental data taken from a selection of 2D and axisymmetric Hypersonic Shock-Wave/Turbulent-Boundary-Layer Interactions of both the compression corner and impinging shock wave type are provided. Included are representative attached, incipient separation and fully separated cases. The data emphasizes surface pressures and heat transfer measurements and are tabulated with a separate Appendix for each experimental case, supplemented with CFD computations accomplished for that case. For each experimental case, sufficient information is given so as to facilitate setup and accomplish the CFD computations based on the published experimental descriptions. The selection of the experiments included in this database was made with consideration of applicability to NASA's mission needs and as to criterion to ensure the quality of the data. The experimental dataset, CFD solutions and grids described in the Appendices are also tabulated in computer-readable ASCII files on a DVD released along with this report.

Acknowledgements

This work was sponsored by NASA's Fundamental Aeronautics–Hypersonics (FAH) and Hypersonic Entry Descent and Landing (HEDL/STMD) projects. The interest, leadership and support of Dr. Deepak Bose (Associate Project Investigator, Hypersonics) and Dr. Michael J. Wright (Project Manager, HEDL) are gratefully acknowledged. The authors acknowledge Dr.'s E. Schülein, R. Hillier, N. Murray, S. Willams and M. Holden for their kind permission to permit inclusion of their data in this document. We also acknowledge D. Prabhu for permission to use portions of his CFD HiFire simulation, and M. Olsen for permission to use his adapted grid for the Kussoy-Horstman cylinder/flare case. Should the reader choose to use data extracted from this database, this database report and the original source documents reporting the experiment should be cited.

Main Text References

1. Bose, D., Brown, J.L., Prabhu, D.K., Gnoffo, P.A., Johnston, C.O. and Hollis, B., "Uncertainty Assessment of Hypersonic Aerothermodynamics Prediction Capability," AIAA Paper 2011-3141, 42nd AIAA Thermophysics Conference, Honolulu, Hawaii, June 27-30, 2011.

2. Gnoffo, P.A., Berry, S.A. and Van Norman, J.W., "Uncertainty Assessments in Simulations of 2D and Axisymmetric Hypersonic Shock Wave-Turbulent Boundary Layer Interactions at Compression Corners," 42nd AIAA Thermophysics Conference, Honolulu, Hawaii, Jun 27-30, 2011.

3. Brown, J.L., "Shock Wave Impingement on Boundary Layers at Hypersonic Speeds: Computational Analysis and Uncertainty," AIAA Paper 2011-3143, 42nd AIAA Thermophysics Conference, Honolulu, Hawaii, Jun 27-30, 2011.

4. Settles, G.S. and Dodson, L.J., "Supersonic and Hypersonic Shock/Boundary-Layer Interaction Database," AIAA Journal, Vol. 32, No. 7, July 1994, pp. 1377-1383.

5. Settles, G.S. and Dodson, L.J., "Hypersonic Shock/Boundary-Layer Interaction Database," NASA CR 177577, April 1991.

6. Roy, C.J. and Blottner, F.G., "Review and assessment of turbulence models for hypersonic flows," *Progress in Aerospace Sciences,* Vol. 42, 2006, pp. 469-530.

7. Schülein, E., Krogmann, P. and Stanewsky, E., "Documentation of Two-Dimensional Impinging Shock/Turbulent Boundary Layer Interaction Flow," DLR, German Aerospace Center, Report IB 223-96 A 49, Gottingen, Germany, Oct., 1996.

8. Murray, N., Hillier, R. and Williams, S., "Experimental Investigation of Axisymmetric Hypersonic Shock-Wave/Turbulent Boundary-Layer Interactions," Journal of Fluid Mechanics, Vol. 714, Jan. 2, 2013, pp. 152-189.

9. Williams, N., "Three-Dimensional Separation of a Hypersonic Boundary-Layer," PhD. Thesis, Department of Aeronautics, Imperial College of Science, Technology and Medicine, University of London, 2004.

10. Murray, N., "Three-Dimensional Turbulent Shock-Wave/Boundary-Layer Interactions in Hypersonic Flows," PhD. Thesis, Department of Aeronautics, Imperial College of Science, Technology and Medicine, University of London, 2007.

11. Mallinson, S.G., Hillier, R., Jackson, A.P., Kirk, D.C., Soltani, S. and Zanchetta, M., "Gun tunnel flow calibration: defining input condition for hypersonic flow computations," Shock Waves, Vol. 10, pp. 313-322, 2000.

12. Holden, M.S., MacLean M., Wadhams, T. and Mundy, E., "Experimental Studies of Shock Wave/Turbulent Boundary Layer Interaction in High Reynolds Number Supersonic and Hypersonic Flows to Evaluate the Performance of CFD Codes," AIAA Paper 2010-4468, 40th Fluid Dynamics Conference and Exhibit, Chicago, Illinois, June 28-July 1, 2010.

13. Coleman, G.T., "Hypersonic Turbulent Boundary Layer Studies," Ph.D. Thesis, Department of Aeronautics, University of London, London, 1973.

14. Coleman G.T. and Stollery, J.L., "Heat transfer from hypersonic turbulent flow at a wedge compression corner," Journal of Fluid Mechanics, Vol. 56, part 4, 1972, pp. 741-752.

15. Elfstrom, G.M.," Turbulent hypersonic flow at a wedge-compression corner", Journal of Fluid Mechanics, Vol. 53, part 1, 1972, pp 113-127.

16. Kussoy, M.I. and Horstman, C.C., "Documentation of Two-and Three-Dimensional Hypersonic Shock Wave/Turbulent Boundary Layer Interaction Flows," NASA TM 101075, Jan. 1989.

17. Holden, M.S., Bergman, R.C., Duryea, G.R., Harvey, J. and Moselle, J.R., "Studies of the Structure of Attached and Separated Regions of Viscous/Inviscid Interaction and the Effects of Combined Surface Roughness and Blowing in High Reynolds Number Hypersonic Flows," AFOSR 89-0033TR, 1988.

18. Holden, M.S., Havener, A.G. and Lee, C.H., "Shock-Wave/Turbulent Boundary-Layer Interaction in High-Reynolds-Number Hypersonic Flow," Calspan-University of Buffalo Research Center, CUBRC-86681, Buffalo NY, 1986.

19. Holden, M.S., "Studies of the Mean and Unsteady Structure of Turbulent Boundary Layer Separation in Hypersonic Flow," AIAA Paper 91-1778, AIAA 22nd Fluid Dynamics, Plasma Dynamics & Lasers Conference, Honolulu, HI June 24-26, 1991.

20. Kussoy, M.I. and Horstman, K.C., "Documentation of Two- and Three-Dimensional Shock-Wave/Turbulent-Boundary-Layer Interaction Flows at Mach 8.2," NASA TM 103838, May 1991.

21. Wright, M.J., White, T.R. and Mangini, N.L., "Data Parallel Line Relaxation Code User Manual, Acadia-Version 4.01.1", NASA TM-2009-215388, Oct. 2009.

22. Mazaheri, A., Gnoffo, P.A., Johnston, C.O. and Kleb, B., "LAURA Users Manual: 5.3-48528," NASA TM 216836, August 2010.

Hypersonic Experiments	References	Mach Number	Data Type
2D-Compression Corner 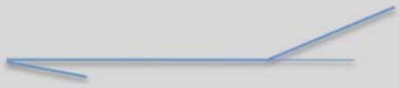	Coleman & Elfstrom (13,14 &15) Holden(12)	9 8.2,11.3	p_w, q_w p_w, q_w,, c_f Schlieren, limited surveys
Cone-Cylinder-Flare 	Kussoy & Horstman(16) Holden(12)	7.2 7.19	p_w, q_w, limited surveys p_w, q_w, c_f
Hollow-Cylinder-Flare 	Williams(9), Murray et al.(8)	8.9	p_w, q_w,
Axisymmetric Cone-Flare 	Holden(12,17,18 &19)	11,13	p_w, q_w, Schlieren, limited surveys
2-D Incident Shock Wave 	Kussoy & Horstman(20) Holden(12) Schülein(7)	8.2 8, 11 5	p_w, q_w, p_w,q_w, Schlieren p_w, q_w, c_f Surveys, Shadowgraph
Axisymmetric Impinging Shock on Hollow Center Body 	Murray(8 & 10), Mallinson(11)	8.9	p_w, q_w, Schlieren

Table 1. Two-Dimensional and Axisymmetric Hypersonic SWBLI Experiments

Appendix A: Compression Surfaces (2-D and Axisymmetric)

A1. Coleman & Elfstrom – 2D Compression Ramp

Ref. A1-1. Coleman, G.T., "Hypersonic Turbulent Boundary Layer Studies," Ph.D. Thesis, Department of Aeronautics, Univ. of London, 1973.

Ref. A1-2. Coleman, G.T. and Stollery, J.L., "Heat transfer from hypersonic turbulent flow at a wedge compression corner," Journal of Fluid Mechanics, Vol. 56, part 4, 1972, pp. 741-752.

Ref. A1-3. Elfstrom, G.M., "Turbulent hypersonic flow at a wedge-compression corner," Journal of Fluid Mechanics, Vol. 53, part 1, 1972, pp. 113-127.

Ref. A1-4. Settles, G.S. and Dodson, L.J., Hypersonic Shock/Boundary-Layer Interaction Database, NASA CR 177577, April 1991.

Ref. A1-5. Horstman, C.C., "Hypersonic Shock-Wave Turbulent Boundary-Layer Interactions Flows - Experiment and Computation," AIAA Paper 91-1760, June 1991.

Ref. A1-6. Coakley, T.J., Horstman, C.C., Marvin, J.G., Viegas, J.R., Bardina, J.E., Huang, P.G. and Kussoy, M.I., Turbulence Compressibility Corrections, NASA TM 108827, May 1994.

General description. The experiment was conducted in the Imperial College Gun Tunnel no 2 at a nominal Mach number of 9.22 and a free stream Reynolds number of 47 x 10^6 per meter. The model was a sharp plate with an adjustable trailing-edge flap. The experiment was selected for the Database assembled by Settles (Ref. A1-4). The data were taken in separate studies with different models. Refs. A1-1 and A1-2 provided heat transfer results and Ref. A1-3, an earlier study, provided the pressure data. The distance to the flap for the experiment for pressure (at 43 cm) was less than that for the heat transfer (at 56 cm). The difference is not significant provided the measurement locations are compared on the basis of the distance from the ramp leading edge rather than the leading edge. In both experiments there was no boundary layer tripping ahead of the flap. Measurements from Ref A1-3 indicated the flow was fully turbulent ahead of the interaction regions. The plate and the flap were instrumented along the centerline with temperature and pressure instrumentation in the separate tests and provide surface pressure and heat transfer distributions ahead of and along the compression surface. A range of compression corner angles provides flow situations from attached through separated. The data tables below were taken directly from Ref. A1-4.

Experimental arrangement. The arrangement shown below is for the heat transfer model used by Coleman.

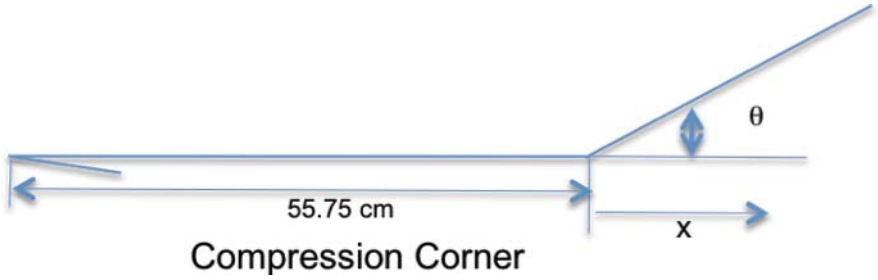

The sharp plate extended 55.75 cm. to the compression corner where the 10 inch flap surface deflected the oncoming flow. The plate with was 17 cm wide and end effects were considered negligible along the center of the plate. Corner compression surface angles were varied to create a range of flow conditions from attached to fully separated flow. The x dimension was measured from the origin of the flap leading edge and in the streamwise direction, even for the flap. Negative values of x indicate measurements on the flat plate.

Facility. Tests were performed in the Imperial College Gun Tunnel no 2. The working gas for this facility is Nitrogen, N_2. The tunnel is comprised of three components: a driver section, a piston driven section and a contoured nozzle and dump-tank section. Burst disks that sequentially initiate the flow separate the sections. Nominal test conditions for the data tabulated herein were: M=9.22, $Re_\infty/m = 47 \times 10^6$, $T_{0,\infty} = 1070°K$, $T_\infty = 64.5°K$, and $T_w = 295°K$. Stagnation and free-stream pressure conditions were not reported explicitly. Settles (Ref. A1-4) surmised that this omission and the fact that data are reported in normalized form may be typical for shock tunnels experiments where constant total pressure is not always achieved. He suggests that users of these pressure data should bear in mind the possible adverse effect of such a procedure on the accuracy of the data. The total run-time was 25 milliseconds. Subsequent experiments in the facility indicated that useful test time was about 5 ms. Instrumentation response time was adequate to capture data during this short time. (See Ref A1-5.)

Measurements. Pressure and heat transfer measurements were taken along the centerline of the test plate and flap. Pressures were measured with un-bonded strain gage transducers. Heat transfer measurements were taken using platinum on glass thin film resistance temperature gauges. No specific accuracy estimates were reported, but subsequent experiments using similar instrumentation indicated worst case scenario total errors in the pressure and heat-transfer measurements were $\pm$ 2.3% and + 8.7%, – 2.2% respectively. (See Ref A1-5.)

A boundary layer profile was taken near the end of a 76 cm flat plate model (without

the flare) using pitot pressure rake measurements, assuming constant static pressure across the layer and the Rayleigh Pitot formula.

Data tables. Below are tables of normalized pressure and heat transfer taken from Ref. A1-4, along with an undisturbed flat plate boundary layer profile.

Table A1-1. Test Conditions

M_∞	9.22
Re_∞/m	47.E+06
ReL	26.2E+06
Tstagnation	1070° K
T_∞	64.5° K
Twall	295° K
δ_0	0.72 cm

Table A1-2. Boundary Layer Profile – X~76 cm

y/Delta	M/M_∞	U/U_∞
0.040	0.253	0.620
0.078	0.349	0.760
0.083	0.370	0.780
0.125	0.365	0.780
0.142	0.386	0.795
0.189	0.404	0.812
0.210	0.470	0.860
0.230	0.473	0.862
0.277	0.509	0.884
0.294	0.539	0.900
0.322	0.561	0.910
0.332	0.574	0.915
0.341	0.578	0.917
0.364	0.584	0.918
0.406	0.599	0.924
0.424	0.658	0.941
0.461	0.667	0.944
0.490	0.679	0.947
0.517	0.672	0.945
0.525	0.696	0.952
0.542	0.720	0.957
0.560	0.760	0.965
0.578	0.760	0.965
0.590	0.775	0.968
0.640	0.802	0.974
0.669	0.847	0.981
0.709	0.868	0.984
0.730	0.902	0.989
0.770	0.952	0.995
0.794	0.960	0.996
0.798	0.966	0.997
0.859	0.974	0.998
0.888	0.980	0.998
0.920	0.988	0.998
0.978	0.990	0.999
0.998	0.995	0.999
1.040	0.996	0.999
1.130	1.000	1.000
1.250	1.000	1.000

Table A1-3: Coleman Compression Corner (15°, Mach=9.22) Wall Pressure Distribution.

X, cm	P/P_∞		X, cm	P/P_∞		X, cm	P/P_∞
-1.90	0.99		0.84	4.70		2.67	11.50
-1.40	1.00		1.10	5.86		3.20	11.80
-0.90	1.02		1.60	7.40		3.45	11.90
-0.40	1.04		1.87	7.40		4.24	11.90
0.30	3.47		2.40	10.40			

Table A1-4: Coleman Compression Corner (15°, Mach=9.22) Wall Heat Transfer Distribution, Q_∞= 6.07 W/cm².

X, cm	Q/Q_∞		X, cm	Q/Q_∞		X, cm	Q/Q_∞
-4.20	1.06		-0.60	0.80		2.60	6.65
-3.65	1.11		0.35	3.16		3.15	7.69
-3.10	0.96		0.60	2.91		3.40	8.05
-2.60	0.96		0.85	3.78		3.90	8.50
-2.05	1.03		1.35	4.27		4.40	8.44
-1.65	0.86		1.60	4.68		4.90	8.61
-1.35	0.94		1.85	5.42		6.70	8.65
-1.10	1.00		2.10	6.30		7.20	8.04
-0.85	0.92		2.35	6.67			

Table A1-5: Coleman Compression Corner (30°, Mach=9.22) Wall Pressure Distribution.

X, cm	P/P_∞		X, cm	P/P_∞		X, cm	P/P_∞
-1.65	1.05		0.25	7.45		2.61	36.20
-0.14	1.05		0.56	15.80		2.89	36.40
-1.14	1.06		0.84	24.20		3.50	36.40
-0.89	1.08		1.15	31.80		3.80	36.00
-0.64	1.11		1.73	34.20		4.65	36.00
-0.38	1.28		2.00	36.00		5.60	36.40

Table A1-6: Coleman Compression Corner (30°, Mach=9.22) Wall Heat Transfer Distribution, Q_∞= 6.17 W/cm².

X, cm	Q/Q_∞		X, cm	Q/Q_∞		X, cm	Q/Q_∞
-5.70	0.99		-0.85	0.96		2.50	19.60
-4.85	0.96		-0.60	0.81		2.70	18.60
-4.40	1.09		-0.35	0.77		3.00	18.50
-4.20	0.94		0.25	5.80		3.30	17.70
-3.65	1.00		0.45	6.70		3.60	17.50
-3.10	0.94		0.70	8.60		3.70	17.00
-2.60	0.95		1.00	10.60		4.10	15.90
-2.35	0.87		1.20	13.10		4.25	16.60
-2.05	0.95		1.50	15.60		4.70	17.10
-1.90	0.95		1.70	15.70		5.30	16.30
-1.35	0.93		2.05	17.70		6.10	14.80
-1.10	0.94		2.24	18.10		6.60	15.40

Table A1-7: Coleman Compression Corner (34°, Mach=9.22) Wall Pressure Distribution.

X, cm	P/P_∞		X, cm	P/P_∞		X, cm	P/P_∞
-2.67	1.02		-0.88	4.98		1.47	26.90
-2.40	1.02		-0.64	4.75		1.78	53.00
-2.16	1.33		-0.38	5.31		2.08	62.30
-1.90	1.90		0.25	6.97		2.40	49.30
-1.65	2.55		0.56	9.90		3.00	51.00
-1.40	3.36		0.87	12.60		3.63	46.80
-1.15	4.56		1.17	19.10		3.94	46.20

Table A1-8: Coleman Compression Corner (34°, Mach=9.22) Wall Heat Transfer Distribution, Q_∞= 6.29 W/cm².

X, cm	Q/Q_∞		X, cm	Q/Q_∞		X, cm	Q/Q_∞
-7.60	0.95		-1.90	2.16		1.70	14.30
-6.65	1.03		-1.65	2.08		2.05	18.00
-5.70	0.98		-1.35	1.80		2.24	21.10
-5.15	1.03		-1.10	1.67		2.50	26.40
-4.65	1.03		-0.85	1.71		2.70	27.60
-4.20	1.00		-0.60	1.52		3.00	29.30
-3.90	0.89		-0.35	2.14		3.30	24.30
-3.65	0.93		0.25	3.22		3.60	23.90
-3.35	0.77		0.45	2.85		3.70	21.80
-3.10	0.90		0.70	5.85		4.25	20.30
-2.85	1.74		1.00	6.04		4.70	21.40
-2.60	1.35		1.20	9.91		5.30	21.40
-2.35	1.79		1.50	11.10		7.10	19.20
-2.05	2.24						

Table A1-9: Coleman Compression Corner (38°, Mach=9.22) Wall Pressure Distribution.

X, cm	P/P_∞		X, cm	P/P_∞		X, cm	P/P_∞
-4.70	1.03		-1.40	6.20		2.00	59.00
-4.45	1.11		-1.14	6.20		2.25	75.50
-4.20	1.24		-0.89	6.20		2.54	86.00
-3.93	1.46		-0.64	6.60		2.80	93.00
-3.68	1.44		-0.38	6.70		3.05	77.50
-3.43	2.54		0.25	7.20		3.30	69.50
-3.18	2.67		0.50	8.50		3.81	59.00
-2.92	4.45		0.75	11.40		4.06	61.50
-2.66	5.25		1.00	15.10		4.32	59.60
-2.41	5.70		1.25	20.80		4.57	57.50
-2.16	5.70		1.50	29.00		5.33	59.00
-1.90	5.70		1.75	49.00			

Table A1-10: Coleman Compression Corner (38°, Mach=9.22) Wall Heat Transfer Distribution, Q_∞= 6.56 W/cm².

X, cm	Q/Q_∞		X, cm	Q/Q_∞		X, cm	Q/Q_∞
-11.20	0.90		-2.60	1.82		2.50	18.70
-10.20	0.90		-2.35	1.65		2.70	23.30
-7.60	1.00		-2.05	1.93		3.00	29.00
-7.10	1.02		-1.90	1.83		3.15	27.20
-6.65	0.95		-1.65	1.70		3.30	31.30
-6.10	1.10		-1.35	1.89		3.60	31.00
-5.70	0.86		-1.10	1.88		3.70	28.50
-5.45	1.22		-0.85	1.98		4.25	25.10
-5.15	1.86		-0.60	1.94		4.40	23.70
-4.85	1.80		0.25	2.86		4.65	25.20
-4.65	2.22		0.45	3.25		4.70	23.70
-4.40	2.40		0.70	4.16		4.90	24.30
-4.20	2.05		1.00	4.82		5.20	22.90
-3.90	2.24		1.20	6.47		5.30	23.40
-3.65	2.15		1.60	10.00		5.45	22.50
-3.35	2.18		1.70	10.60		5.75	22.40
-2.85	1.92		2.24	16.40		6.70	22.70

Baseline Computations. The tabulated results for this compression corner experiment of Coleman and Stollery, and of Elfstrom are an example of results from the previously published database of Settles and Dodson, but are herein duplicated in this report and on the associated DVD. Additional experiments of the Settles and Dodson database are also included in the DVD associated with this report (but without CFD computations) inasmuch as the Settles and Dodson database was released on a floppy media that is now difficult to read with much of the available computer equipment.

In contrast to the remaining experiments described in the subsequent Appendices of this report, baseline computations specific to this database report are not provided for the Coleman/Elfstrom case of this Appendix. Rather, the reader is referred to the previously published computations of Horstman et al. (Figure 10 of Ref. A1-5) and of Coakley et al. (Figure 8 of Ref. A1-6). The reader is referred to the original documents (Ref. A1-5 and A1-6) for explanations of the turbulence model corrections indicated in legends for these figures. In both these prior computations, the upstream flat plate development arising from considering the whole model geometry was not computed, but rather a truncated grid in the vicinity of the compression corner was employed with the measured boundary layer just upstream of the interaction being imposed as the inlet condition. In the remaining flow cases of the database, the CFD results that are provided compute the complete geometry including the upstream boundary layer development. For convenience to the reader, both of these latter reports (being of NASA/US Government origin) are included as PDF files on the associated DVD.

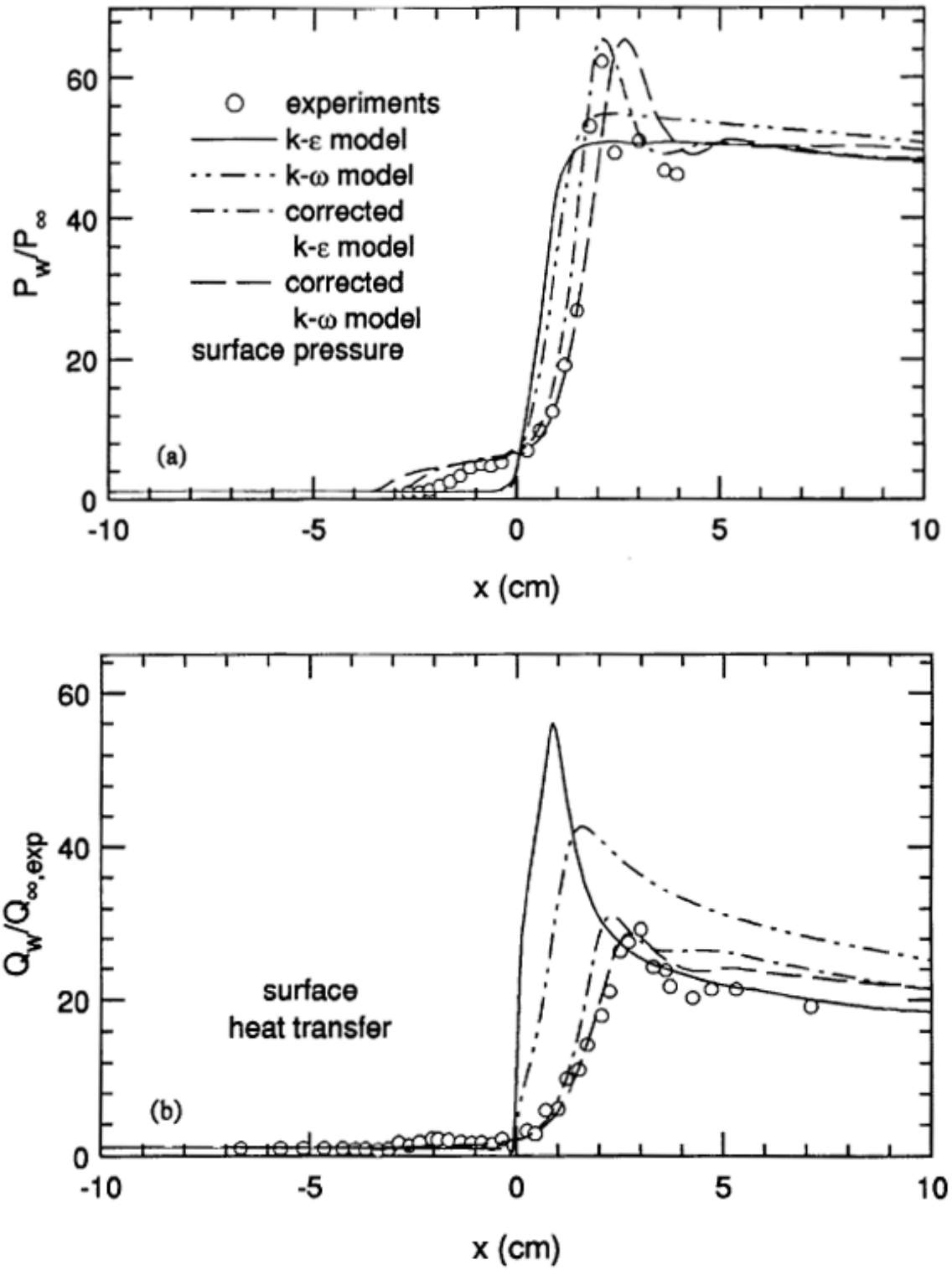

Fig A1-1. Wall Pressure (a) and Wall Heating (b) distribution comparison of Computations of Coakley, et al. (Fig 8 of Ref. A1-6) with Experimental results of Elfstrom (a) and Coleman (b) for 34° Compression Corner at M=9.22.

A2. Holden, et al. – 2D Compression Ramp

Ref. A2-1. Holden, M., MacLean, M., Wadhams, T. and Mundy, E., "Experimental Studies of Shock Wave/Turbulent Boundary Layer Interaction in High Reynolds Number Supersonic and Hypersonic Flows to Evaluate the Performance of CFD Codes", AIAA Paper 2010-4468, 40th Fluid Dynamics Conference and Exhibit, Chicago, Illinois, June 28 – July 1, 2010.

Ref. A2-2. Gnoffo, P.A., Berry, S.A. and Van Norman, J.W., "Uncertainty Assessments of 2D and Axisymmetric Hypersonic Shock Wave – Turbulent Boundary Layer Interaction Simulations at Compression Corners", AIAA Paper 2011-3142, 42nd AIAA Thermophysics Conference, Honolulu, HI, June 27-30, 2011.

Ref. A2-3. Anon, "Large Energy National Shock Tunnel (LENS)", CALSPAN-UB Research Center, Accession no 5690, Dec. 1, 1990.

General description. Over time CUBRC has performed numerous experiments dealing with SWBLI, both laminar and turbulent. A reexamination of the resulting data (Ref. A2-1) led to recommendations for data to be used in validation. These data were provided to NASA for its uncertainty analysis studies (see e.g. Ref. A2-2) and were chosen for documentation herein. Table A2-1 provides the conditions for all these recommended data. The Flat Plate and Compression Ramp data runs are presented further in this Appendix. Subsequent Appendices will present and discuss the hypersonic cone-cylinder-flare (Run 30) and the 20 deg impinging Shock Generator runs 44 and 49.

Table A2-1: Holden Hypersonic Run Conditions

TM Section	*Run*	*Shock*	*Flow*	*Mach*	*U, m/s*	*ρ, Kg/m³*	*T, K*
A3	4	Cone-Flare	Turbulent	11	1804.1	0.03270	67.2
A2	7	Flat Plate	Transition	11.1	1780	0.09483	64
A2	10	Flat Plate	Transition	10.6	1739	0.09637	67
A2	22	12° Ramp	Laminar	11.7	1905	0.00141	66
A2	54	36° Ramp	Turbulent	11.3	1769	0.08246	61
A2	12	27° Ramp	Turbulent	8.2	1390	0.5090	71.1
A2	16	30° Ramp	Turbulent	8.3	1375	0.5060	68.9
A2	19	33° Ramp	Turbulent	8.1	1379	0.4910	71.7
A2	24	36° Ramp	Turbulent	8.2	1378	0.4990	70
A4	30	ConeCylFlare	Turbulent	7.19	2170	0.0670	226
A4	36	ConeCylFlare	Turbulent	7.16	2359.2	0.0608	262
B4	44	5° Generator	Laminar	11.7	1905	0.00139	66
B4	49	20° Generator	Turbulent	11.4	1814	0.08910	63

The compression corner or ramp test runs were performed at nominal Mach numbers in the range between 7 and 11 and at high Reynolds numbers resulting in substantial lengths of naturally developing turbulent boundary layer flow ahead of the interaction regions.

Flat plate data, obtained as part of a CUBRC study on boundary layer transition, and are also included in data tables. These data provide a means for checking CFD simulations of onset and end of transition and upstream boundary layer properties ahead of the shock interactions on the compression corner and incident shock cases.

Experimental arrangement. A flat plate model was tested to provide undisturbed boundary layer data. The plate had a sharp tip and was 12" wide and 52" long. Investigative tests were performed that showed no influence of end effects. (See Ref. A2-1)

Flat Plate

The compression corner model arrangement for the turbulent Mach 11.3 condition is given below. At nominal M=8.2, the wedge angles, θ, were 27^0, 30^0, 33^0 and 36^0 for turbulent run numbers 12, 16, 19 and 24 respectively, and at nominal M=11.3 it was 12^0 for laminar run 22 and 36^0 for turbulent run 54 that resulted in separated flow in the corner region. The compression corner was located at X=17.3 inch for laminar run 22, and at X=40.3 inch for the turbulent compression corner Mach 11 run 54. (See sketch below.) For the Mach 8 compression corner runs 12, 16, 19 and 24, the corner is located at X=39.2 inch. The authors state that additional testing indicated plate leading edge end effects were minimal.

Compression Corner

Facility. The experimental data were obtained in the CUBRC shock tunnel facilities described in Refs. A2-1 and A2-3. Ref. A2-1 describes the three shock tunnels that comprise the facility. The basic tunnel components are a driver tube, a driven section, a contoured nozzle and a test section connected to a receiver tank and vacuum system. The operation of the tunnel begins by charging the driver tube to a high pressure and subsequently rupturing a diaphragm that separates the driver

tube and driven section. Then, the high-pressure gas in the driver expands into the driven section. A normal shock wave is generated that creates high pressure and high enthalpy air that subsequently expands into the nozzle and test section. Operated at tailored interface conditions (See Ref. A2-3) and depending on the driver gas, test times on the order of 10 milliseconds are obtained. Test times are sufficient to establish steady flow over the model.

Measurements. The flat plate was instrumented with thin film heat transfer gages and floating element piezoelectric skin friction gages. (See Ref. A2-3). Surface heat transfer and skin friction were reported and are given in the data tables below. Accuracy of the heat transfer was estimated as ±5% and skin friction between ±7 to ±12%, see Refs. A2-1 and A2-2. Free stream dynamic pressure and stagnation enthalpy were accurate to ±5% and Mach number to ±1.5%. Test conditions varied from the nominal Mach 11 for the two flat plate runs as listed in Table A2-1.

The plate and wedge compression surfaces were also instrumented with piezoelectric pressure transducers, thin film heat transfer gages and floating element piezoelectric skin friction gages. Instrumentation response times are sufficient to provide measurements during the short test time. Surface pressures, surface heat transfer and skin friction were reported and are give in the data tables below. Accuracy of the pressure measurements was estimated as ±3%, heat transfer as ±5%, and skin friction between ±7 to ±12%, see Refs. A2-1 and A2-3. Free stream dynamic pressure and stagnation enthalpy were accurate to ±5% and Mach number to ±1.5%. Test conditions varied for each run case as listed in Table A2-1.

Working fluid for this experiment was dry Air.

Data tables.

Table A2-2: Holden Flat Plate (Run 7, Mach=11.1)
Wall Heating Distribution

X, in	Q, btu/ft²-sec		X, in	Q, btu/ft²-sec		X, in	Q, btu/ft²-sec
2.00	4.0795		18.00	7.3385		39.13	4.7687
4.00	2.8689		19.00	6.8085		39.28	4.6480
5.00	2.7185		22.00	6.3676		39.59	4.7092
6.00	2.3389		23.00	5.5384		40.56	4.5483
7.00	2.3896		25.00	5.8988		41.21	4.7495
8.00	2.5191		26.00	5.9093		41.85	4.8982
10.00	3.0194		27.00	6.0492		42.50	4.6095
11.00	3.5792		32.52	4.8282		43.67	4.8282
12.00	4.8195		35.04	5.2795		44.31	4.5395
13.00	6.4690		36.69	4.4486		45.59	4.3681
14.00	6.7787		37.76	4.4380		47.5	4.4188
16.00	7.3385		38.29	4.5693		48.79	4.3086
17.00	7.2388		38.82	4.3681		50.07	4.4083

Table A2-3: Holden Flat Plate (Run 7, Mach=11.1)
Wall Skin Friction Distribution

X, in	τ, psi
32.53	0.014691
36.72	0.011762
37.21	0.011346
37.75	0.013161
38.27	0.012089
39.56	0.01397
41.43	0.012898
42.39	0.012396
43.32	0.012002
44.31	0.013838
45.27	0.012221
47.19	0.012111

Table A2-4: Holden Flat Plate (Run 10, Mach=10.6)
Wall Heating Distribution

X, in	Q, btu/ft²-sec		X, in	Q, btu/ft²-sec		X, in	Q, btu/ft²-sec
2.00	3.9291		18.00	6.8676		39.13	4.4382
4.00	2.7987		19.00	6.8290		39.28	4.5682
5.00	2.7795		20.00	7.1983		39.59	4.4590
6.00	1.9798		22.00	5.9491		40.56	4.2984
7.00	2.2689		25.00	5.6087		41.21	4.4285
8.00	2.0890		26.00	5.2682		41.85	4.4992
10.00	3.3992		27.00	5.4593		42.50	4.2390
11.00	4.9488		32.52	4.6693		43.67	4.1684
12.00	6.7679		35.04	5.1286		44.31	4.1587
13.00	8.5583		36.69	4.2984		47.50	4.2390
14.00	7.6575		37.76	4.9985		48.79	4.0383
16.00	7.2480		38.29	5.2089		50.07	3.9484
17.00	6.9478		38.82	4.3787		51.36	4.1186

Table A2-5: Holden Flat Plate (Run 10, Mach=10.6)
Wall Skin Friction Distribution

X, in	τ, psi
32.53	0.013884
36.72	0.012083
37.21	0.012983
37.75	0.010994
38.27	0.013193
39.56	0.012837
40.48	0.012292
41.43	0.012523
42.39	0.011748
43.32	0.011999
44.31	0.013654
45.27	0.011685
47.19	0.011895

Table A2-6: Holden 12° Compression Corner-Laminar (Run 22, Mach=11.7)
Wall Pressure Distribution

X, in	P, psia		X, in	P, psia		X, in	P, psia
14.92	0.00665		16.61	0.0114		20.83	0.0325
15.08	0.00658		16.94	0.0112		21.47	0.0389
15.43	0.00715		17.12	0.0121		22.75	0.0416
15.59	0.00677		17.63	0.0133		24.67	0.0474
15.94	0.00694		18.27	0.0157		25.95	0.0532
16.10	0.00874		19.55	0.0235		27.23	0.0457
16.44	0.00935		20.19	0.0259		28.51	0.0477

Table A2-7: Holden 12° Compression Corner-Laminar (Run 22, Mach=11.7)
Wall Heating Distribution

X, in	Q, btu/ft²-sec		X, in	Q, btu/ft²-sec		X, in	Q, btu/ft²-sec
7.24	0.367		16.38	0.172		18.34	0.341
10.25	0.286		16.67	0.138		19.55	0.539
12.24	0.269		16.87	0.130		20.83	0.717
13.51	0.256		17.06	0.121		22.10	0.945
14.73	0.226		17.26	0.110		23.40	1.170
15.45	0.248		17.41	0.144		24.67	1.180
15.65	0.228		17.60	0.184		25.96	1.230
15.85	0.232		17.80	0.204		27.24	1.250
16.04	0.21		18.00	0.239		28.50	1.310
16.24	0.202		18.19	0.244			

Table A2-8: Holden 12° Compression Corner-Laminar (Run 22, Mach=11.7)
Wall Shear Stress Distribution

X, in	τ, psi		X, in	τ, psi		X, in	τ, psi
8.29	0.000782		15.40	0.000387		17.05	-6.84E-05
10.29	0.000636		15.73	0.00027		17.62	-1.71E-04
12.29	0.000634		16.06	0.0000605		18.59	-0.000102
14.41	0.000512		16.39	-0.0000221		19.54	0.0000991
15.07	0.000534		16.72	-0.000119		21.47	0.000972

Table A2-9: Holden 36° Compression Corner (Run 54, Mach=11.3)
Wall Pressure Distribution

X, in	P, psia		X, in	P, psia		X, in	P, psia
32.53	0.206		39.56	1.08		45.59	14.9
35.02	0.221		41.78	10.2		46.22	14.6
36.72	0.204		42.38	16.5		47.5	14.5
37.31	0.198		43.02	16.6		48.79	16.5
37.75	0.327		43.67	14.3		50.07	15.0
38.27	0.76		44.31	14.9		51.36	14.4
38.82	1.15		44.94	15.4			

Table A2-10: Holden 36° Compression Corner (Run 54, Mach=11.3)
Wall Heating Distribution

X, in	Q, btu/ft²-sec		X, in	Q, btu/ft²-sec		X, in	Q, btu/ft²-sec
32.52	4.39		39.28	9.81		42.50	181.00
34.02	4.82		39.42	10.20		43.02	160.00
35.04	4.50		39.59	9.91		43.67	146.00
35.93	4.00		39.68	10.90		44.31	142.00
36.13	4.13		39.89	12.00		44.94	125.00
36.48	4.19		40.36	33.10		45.59	116.00
36.69	4.10		40.56	56.50		46.22	107.00
37.56	4.00		41.01	94.20		46.87	107.00
37.76	3.98		41.21	107.00		47.50	99.90
38.08	9.50		41.66	176.00		48.79	105.00
38.61	8.85		41.85	210.00		50.07	97.70
38.82	10.50		42.30	195.00		51.36	88.70
39.13	10.40						

Table A2-11: Holden 36° Compression Corner (Run 54, Mach=11.3)
Shear Stress Distribution

X, in	τ, psi		X, in	τ, psi		X, in	τ, psi
32.53	0.00615		38.27	-0.00299		43.32	0.400
36.72	0.00868		39.56	-0.00550		45.27	0.245
37.21	0.01000		40.48	0.01140		47.19	0.247
37.75	0.00204		42.39	0.57100			

Table A2-12: Holden 27° Compression Corner (Run 12, Mach=8.2)
Wall Pressure Distribution

X, in	P, psia		X, in	P, psia		X, in	P, psia
30.130	1.49		38.785	1.56		40.860	39.20
32.130	1.69		38.965	1.45		41.025	38.70
37.270	1.62		39.335	13.80		41.205	39.30
37.430	1.50		39.500	17.30		41.535	39.30
37.610	1.52		40.015	35.50		41.715	41.10
37.780	1.61		40.180	38.10		42.220	38.00
37.940	1.35		40.335	41.50		42.730	40.90
38.285	1.52		40.525	39.30		43.240	38.40
38.450	1.50		40.690	36.70			

Table A2-13: Holden 27° Compression Corner (Run 12, Mach=8.2)
Wall Heating Distribution

X, in	Q, btu/ft^2-sec		X, in	Q, btu/ft^2-sec		X, in	Q, btu/ft^2-sec
29.085	13.90		38.615	13.20		40.150	173.00
32.180	13.40		38.710	13.00		40.250	173.00
34.085	13.90		38.810	13.30		40.360	174.00
35.355	13.70		38.905	13.10		40.550	176.00
36.570	13.80		39.005	12.80		40.745	179.00
37.295	12.40		39.100	10.10		40.940	177.00
37.495	12.70		39.370	126.00		41.130	177.00
37.690	13.10		39.470	139.00		41.360	178.00
37.885	12.90		39.565	144.00		41.555	180.00
37.985	12.80		39.665	153.00		41.750	171.00
38.085	13.40		39.760	153.00		42.330	163.00
38.225	13.30		39.860	164.00		42.920	168.00
38.420	12.80		39.955	167.00		43.550	163.00
38.515	13.10		40.055	173.00			

Table A2-14: Holden 27° Compression Corner (Run 12, Mach=8.2)
Wall Shear Stress Distribution

X, in	τ, psia		X, in	τ, psia		X, in	τ, psia
30.130	0.0254		37.570	0.0393		40.060	0.1890
32.130	0.0400		37.900	0.0351		40.385	0.7170
34.130	0.0415		38.230	0.0397		40.720	0.5660
36.250	0.0366		38.560	0.0331		41.050	0.6820
36.910	0.0393		38.890	0.0240		41.380	0.6820
37.240	0.0267		39.390	0.1740		43.355	0.6510

Table A2-15: Holden 30° Compression Corner (Run 16, Mach=8.3)
Wall Pressure Distribution

X, in	P, psia		X, in	P, psia		X, in	P, psia
30.130	1.36		38.785	1.56		40.690	45.20
32.130	1.54		38.965	1.52		40.860	44.90
37.270	1.52		39.335	14.00		41.025	45.10
37.430	1.42		39.500	19.60		41.205	44.30
37.610	1.31		39.670	29.20		41.535	45.40
37.780	1.52		40.015	41.80		41.715	48.40
37.940	1.30		40.180	40.90		42.220	45.90
38.285	1.50		40.335	47.20		42.730	47.00
38.450	1.48		40.525	46.50		43.240	44.50

Table A2-16: Holden 30° Compression Corner (Run 16, Mach=8.3)
Wall Heating Distribution

X, in	Q, btu/ft²-sec		X, in	Q, btu/ft²-sec		X, in	Q, btu/ft²-sec
29.085	13.0		38.710	11.0		40.150	183.0
34.085	13.2		38.810	11.5		40.250	178.0
35.355	12.0		38.905	12.1		40.360	173.0
36.570	12.0		39.100	16.3		40.550	182.0
37.295	11.7		39.180	91.5		40.745	178.0
37.495	11.5		39.370	186.0		40.940	178.0
37.690	11.8		39.470	174.0		41.130	178.0
37.885	11.9		39.565	178.0		41.360	178.0
38.085	12.2		39.665	207.0		41.555	187.0
38.225	11.9		39.760	178.0		41.750	172.0
38.420	12.1		39.860	175.0		42.330	162.0
38.515	11.6		39.955	178.0		42.920	162.0
38.615	12.4		40.055	176.0		43.550	159.0

Table A2-17: Holden 30° Compression Corner (Run 16, Mach=8.3)
Wall Shear Stress Distribution

X, in	τ, psia		X, in	τ, psia		X, in	τ, psia
30.130	0.0226		37.570	0.0348		40.060	0.213
32.130	0.0376		37.900	0.0328		40.385	0.660
34.130	0.0378		38.230	0.0366		40.720	0.610
36.250	0.0335		38.560	0.0283		41.050	0.723
36.910	0.0364		38.890	0.0238		41.380	0.619
37.240	0.0238		39.390	-0.00502		43.355	0.621

Table A2-18: Holden 33° Compression Corner (Run 19, Mach=8.1)
Wall Pressure Distribution

X, in	P, psia		X, in	P, psia		X, in	P, psia
30.130	1.32		38.785	6.29		40.690	55.10
32.130	1.51		38.965	6.98		40.860	62.80
37.270	1.53		39.335	7.90		41.025	59.70
37.430	1.43		39.500	10.10		41.205	56.20
37.780	2.95		39.670	16.30		41.535	55.40
37.940	4.70		40.015	28.70		41.715	54.30
38.285	5.68		40.180	39.10		42.220	49.50
38.450	6.63		40.335	63.90		42.730	69.10
38.620	5.20		40.525	63.70		43.240	78.50

Table A2-19: Holden 33° Compression Corner (Run 19, Mach=8.1)
Wall Heating Distribution

X, in	Q, btu/ft²-sec		X, in	Q, btu/ft²-sec		X, in	Q, btu/ft²-sec
29.085	12.5		38.710	21.7		40.055	151.0
32.180	11.5		38.810	23.6		40.150	174.0
34.085	12.4		38.905	23.8		40.250	194.0
35.355	12.1		39.005	27.1		40.360	213.0
36.570	11.9		39.100	35.9		40.550	255.0
37.295	11.3		39.180	41.3		40.745	262.0
37.495	11.3		39.275	63.1		40.940	251.0
37.690	12.3		39.370	83.5		41.130	233.0
37.885	22.0		39.470	110.0		41.360	234.0
37.985	21.5		39.565	119.0		41.555	232.0
38.085	25.2		39.665	123.0		41.750	216.0
38.225	22.9		39.760	123.0		42.330	204.0
38.420	22.5		39.860	125.0		42.920	208.0
38.515	21.4		39.955	135.0		43.550	208.0
38.615	23.8						

Table A2-20: Holden 33° Compression Corner (Run 19, Mach=8.1)
Wall Shear Stress Distribution

X, in	τ, psia		X, in	τ, psia		X, in	τ, psia
30.130	0.0230		37.240	0.0239		40.720	1.670
32.130	0.0357		37.900	0.0453		41.050	0.992
34.130	0.0371		38.230	0.0329		41.380	0.895
36.250	0.0334		39.390	-0.128		43.355	0.917
36.910	0.0389		40.060	-0.180			

Table A2-21: Holden 36° Compression Corner (Run 24, Mach=8.2)
Wall Pressure Distribution

X, in	P, psia		X, in	P, psia		X, in	P, psia
30.130	1.35		38.620	6.52		40.690	67.7
32.130	1.53		38.785	7.63		40.860	82.8
36.920	1.75		38.965	8.21		41.025	70.4
37.270	5.12		39.335	9.69		41.205	61.4
37.430	5.62		39.500	10.9		41.535	66.7
37.610	5.09		39.670	18.7		41.715	65.2
37.780	6.02		40.015	28.0		42.220	53.1
37.940	6.51		40.180	38.2		42.730	64.5
38.285	7.02		40.335	61.8		43.240	62.7
38.450	7.80		40.525	75.4			

Table A2-22: Holden 36° Compression Corner (Run 24, Mach=8.2)
Wall Heating Distribution

X, in	Q, btu/ft²-sec		X, in	Q, btu/ft²-sec		X, in	Q, btu/ft²-sec
29.085	13.0		38.420	24.5		40.250	180.0
32.180	12.9		38.515	24.3		40.360	186.0
34.085	12.6		38.615	24.8		40.550	249.0
35.355	12.5		38.710	25.4		40.745	273.0
36.570	12.4		38.810	28.1		40.940	282.0
37.295	20.4		38.905	28.8		41.130	283.0
37.495	21.9		39.005	29.4		41.360	243.0
37.690	21.5		39.100	42.3		41.555	234.0
37.885	22.3		39.760	133.0		41.750	219.0
37.985	22.9		39.955	160.0		42.330	232.0
38.085	22.9		40.055	168.0		42.920	228.0
38.225	24.4		40.150	181.0		43.550	227.0

Table A2-23: Holden 36° Compression Corner (Run 24, Mach=8.2)
Wall Shear Stress Distribution

X, in	τ, psia		X, in	τ, psia		X, in	τ, psia
30.130	0.0235		37.900	0.00647		40.720	-1.84
32.130	0.0391		38.230	0.0379		41.050	-0.776
34.130	0.0389		38.560	-0.0114		42.040	0.917
36.250	0.0351		39.390	-0.183		43.355	1
37.240	0.00981		40.060	0.835			
37.570	0.0418		40.385	-3.8			

Baseline Computations. Selected computations follow that provide a baseline for those wanting to compute the experiments documented above. The baseline is intended to facilitate and gage new code development and turbulence model improvements. These were previously obtained and published by NASA during their assessment of uncertainty related to hypersonic simulations of SWBLI. See Ref. A2-2.

Baseline simulation results for the flow over a flat plate are given in Ref. A2-2 and will not be shown here. These simulation results were used to establish credibility for transition onset and end for the compression corner computations. Grid resolved simulations for the compression corner using several turbulence models are shown below for the 36 degree case at Mach 11.

Figures A2-1 to A2-2 show computed pressure, heating and shear stress distributions compared to experimental data for the Spalart-Allmaras, Menter-SST, k-omega (1998), and k-omega (2006) models, respectively. The grid was 264 by 94 and the solution was considered grid-converged. See Ref. A2-2 for further discussion. The Spalart-Allmaras model has the best prediction of extent of separation for this case though all of the models under-predict its extent. All of the models over-predict heating and under-predict shear after flow re-attachment.

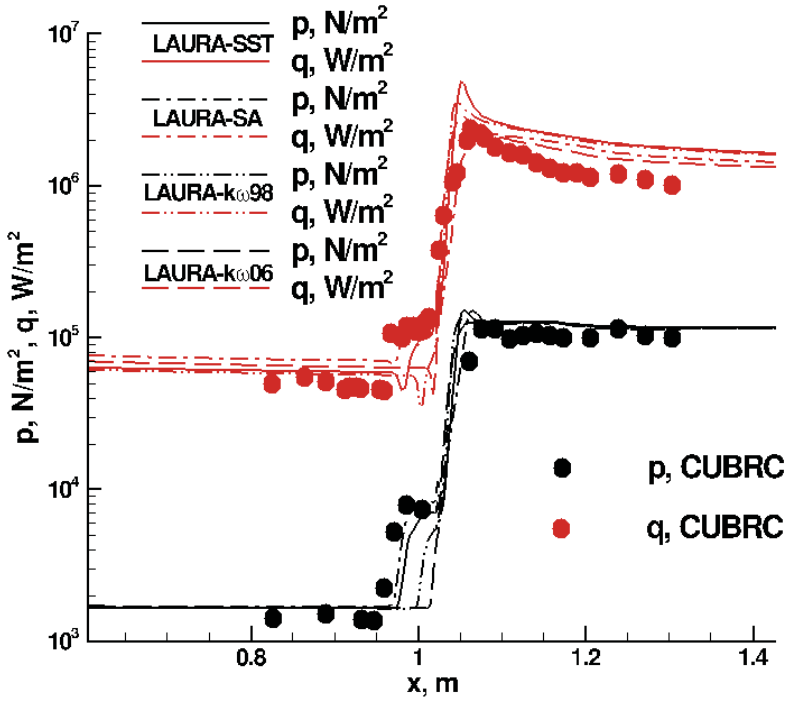

Figure A2-1. Pressure and heating distributions for the Holden 36º compression corner (Run 54) at Mach 11.3 with various turbulence models on baseline grid (264 x 94).

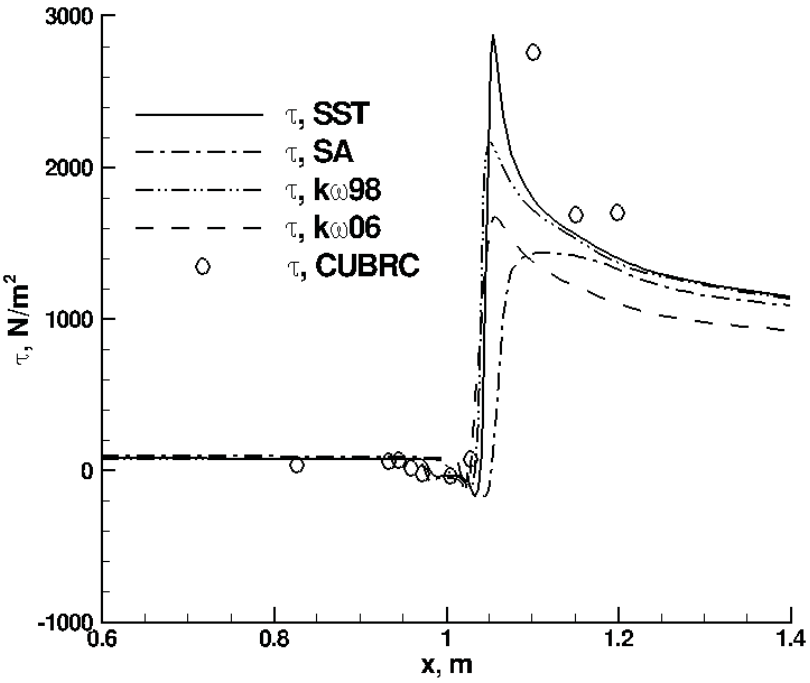

Figure A2-2. Shear Stress distributions for the Holden 36º compression corner (Run 54) at Mach 11.3 with various turbulence models on baseline grid (264 x 94).

A3. Holden, et al. – Axisymmetric Cone-Flare

Ref. A3-1. Holden, M., MacLean, M., Wadhams, T. and Mundy, E., "Experimental Studies of Shock Wave/Turbulent Boundary Layer Interaction in High Reynolds Number Supersonic and Hypersonic Flows to Evaluate the Performance of CFD Codes", AIAA Paper 2010-4468, 40th Fluid Dynamics Conference and Exhibit, Chicago, Illinois, June 28 – July 1, 2010.

Ref. A3-2 Settles, G.S. and Dodson, L.J., "Hypersonic Shock/Boundary-Layer Interaction Database," NASA CR 177577, April 1991.

Ref. A3-3. Settles, G.S. and Dodson, L.J., "Supersonic and Hypersonic Shock/Boundary-Layer Interaction Database," AIAA Journal, Vol. 32, No. 7, July 1994.

Ref. A3-4. Holden, M.S., "Studies of the Mean and Unsteady Structure of Turbulent Boundary Layer Separation in Hypersonic Flow", AIAA Paper 91-1778, AIAA 22nd Fluid Dynamics, Plasma Dynamics & Lasers Conference, Honolulu, Hawaii, June 24-26, 1991.

Ref. A3-5. Gnoffo, P.A., Berry, S.A. and Van Norman, J.W. "Uncertainty Assessments of 2D and Axisymmetric Hypersonic Shock Wave – Turbulent Boundary Layer Interaction Simulations at Compression Corners", AIAA Paper 2011-3142, 42nd AIAA Thermophysics Conference, Honolulu, Hawaii, June 27-30, 2011.

Ref. A3-6 Anon, "Large Energy National Shock Tunnel (LENS)", CALSPAN-UB Research Center, Accession no. 5690, Dec. 1, 1990.

General description. The CUBRC cone-flare data were vetted and made part of the original Settles-Dodson database (Ref.A3-2). Subsequently the geometry, test conditions and data for one flare angle were reexamined (Ref.A3-1) and later recommended to NASA for inclusion in their uncertainty studies. These data were obtained at a nominal Mach number of 11 and at a high Reynolds number resulting in substantial length of naturally developing turbulent boundary layer flow ahead of the flare section and separation in the cone-flare junction. Prior publications of the data and data for other flare angles can be found in Ref.'s A3-2 and A3-4. The model was positioned so that the cone tip protruded into the contoured nozzle but it is believed that the test rhombus provided uniform free stream flow over the entire cone-flare model. See Ref. A3-4.

Experimental Arrangement. The sharp cone-flare geometry for M=11 separated flow case is shown below. The flare angle relative to the cone surface was 36^0 and separation occurred in the corner region.

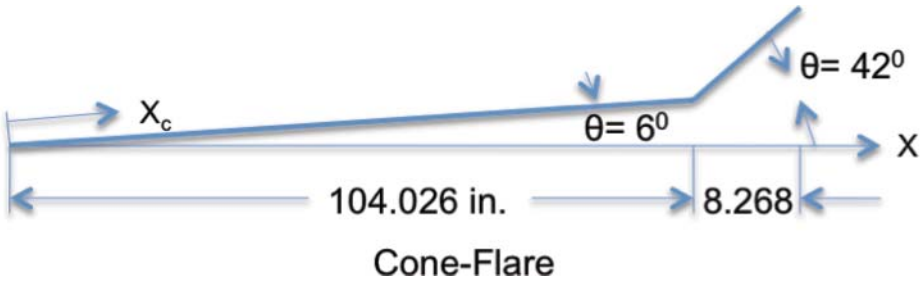

Cone-Flare

Facility. The experimental data was obtained in the CUBRC 96 in. shock tunnel. See Facility description in Appendix A-2, Ref.A3-4 and Ref.A3-6.

Measurements. The cone –flare model was instrumented with piezoelectric pressure gages and thin film heat transfer gages. Surface pressures and heat transfer were reported and are given below in Table A3-4. Distance is measured along the 6^0 cone surface, $x_c=x/\cos(6^0)$, even for locations beyond the junction of the flare with the cone. Accuracy of the pressure measurements was estimated as $\pm$3%, heat transfer as $\pm$5%, and skin friction between $\pm$7 to $\pm$12%. (See Refs. A3-1 and A3-4.) Test conditions were: M=11, ρ_∞= .032354 kg/m^3, T_∞= 67.4^{0}K, u_∞=1807 m/s and $\alpha=0^0$. Wall temperature is $T_w=300^0$K. Free stream dynamic pressure and stagnation enthalpy were accurate to $\pm$5% and Mach number to $\pm$1.5%. Working fluid for this experiment was dry Air.

Data tables. The data tables below are directly from Settles and Dodson, Ref.A3-2. Holden reexamined the data, found them to be acceptable for validation studies and presented the same data as normalized pressures and heating in Ref A3-1.

Table A3-1: Holden Cone-Flare, Run 4, Mach=11 Wall Pressure Distribution

X_C, inch	P, psia
98.9105	0.26728
100.1195	0.28851
101.9185	0.34467
102.5125	0.80524
103.1135	1.29314
103.7165	1.38824
104.0165	1.53297
104.6765	1.30152
106.1825	14.9127
106.6825	15.1135
107.1835	12.6621
107.6835	13.9913
108.6805	14.5525
109.6825	15.4217
110.6825	12.9523
111.6825	11.9923
112.6825	12.2768

Table A3-2: Holden Cone-Flare, Run 4, Mach=11 Wall Heating Distribution

X_C, in	Q, Btu/ft2-sec		X_C, in	Q, Btu/ft2-sec
98.9105	5.85107		105.6825	172.171
101.3175	5.71897		106.1825	203.513
101.6065	5.80157		106.6825	197.140
101.9185	6.16079		107.1835	177.999
102.2195	9.01738		107.6835	175.618
102.5125	14.7118		108.1765	165.347
102.8135	14.6640		108.6805	146.599
103.1135	13.2007		109.1835	144.159
103.4165	13.3030		109.6825	136.357
103.7165	11.9369		110.6825	129.164
104.0165	17.4385		111.6825	104.948
105.1835	90.0276		112.6825	102.294

Baseline Computations. Computations follow that provide a baseline for those wanting to compute the experiments documented above. The baseline is intended to facilitate and gage new code development and turbulence model improvements. These were previously obtained and published by NASA during their assessment of uncertainty related to hypersonic simulations of SWBLI. See Ref. A3-5.

Pressure distribution contours across the shock layer in the simulated domain are shown in Figure A3-1. Comparisons to experimental data for pressure and heating using various turbulence models can be found in Ref. A3-4. Herein we have chosen to baseline the solution using the k-omega (2006) model because the implementation of the compressibility correction with M_{t0} = 0.5 provided best agreement with extent of separation in this case though the plateau level of heating in the separated region is poorly predicted. We note that setting M_{t0} = 0.7 resulted in a near total collapse of the separated region (almost no separation) as the larger parameter failed to sufficiently engage the compressibility correction across the boundary layer.

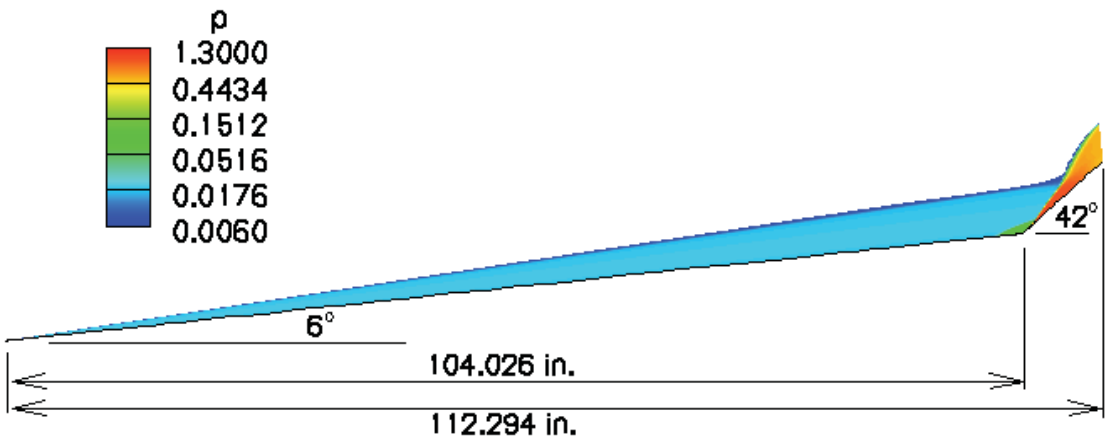

Figure A3-1. Cone-flare geometry with shock layer pressures non-dimensionalized by $(\rho V^2)_\infty$.

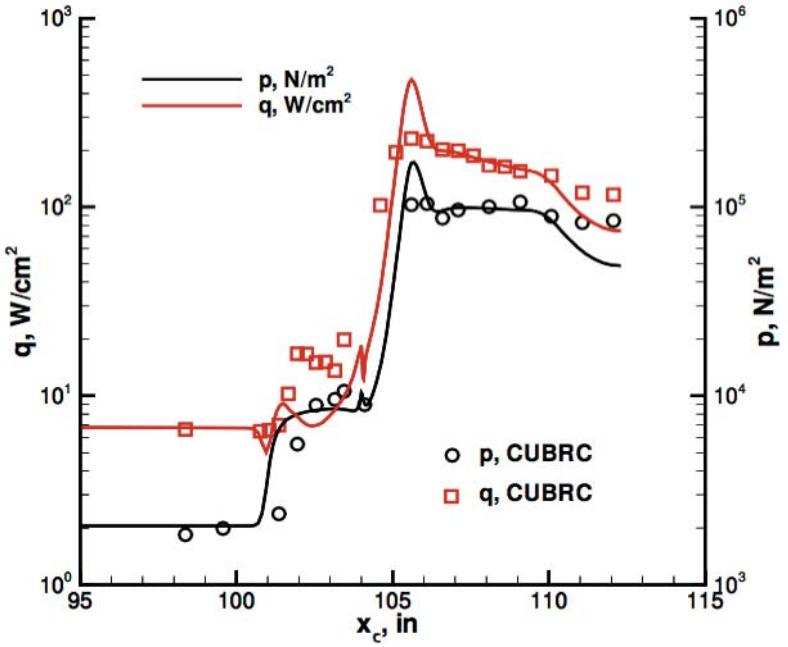

Figure A3-2. Pressure and heating on finest grid (520 x 512) over a 6-degree cone with 36-degree compression at Mach 11 computed with k - omega (2006) model and M_{t0} = 0.5.

A4. Holden, et al. – Axisymmetric HiFire Cone-Cylinder-Flare

Ref. A4 -1. Holden, M., MacLean, M., Wadhams, T. and Mundy, E., "Experimental Studies of Shock Wave/Turbulent Boundary Layer Interaction in High Reynolds Number Supersonic and Hypersonic Flows to Evaluate the Performance of CFD Codes", AIAA Paper 2010-4468, 40th Fluid Dynamics Conference and Exhibit, Chicago, Illinois, June 28 – July 1, 2010.

Ref. A4-2. Wadhams, T., Mundy, E., MacLean. M. and Holden, M., "Ground Test Studies of the HIFiRE-1 Transition Experiment", Journal of Spacecraft and Rockets, vol. 45, no. 6, November–December 2008.

Ref. A4-3. MacLean, M., Wadhams, T. and Holden, M., "Ground Test Studies of the HIFiRE-1 Transition Experiment Part 2: Computational Analysis", Journal of Spacecraft and Rockets, vol. 45, no. 6, November–December 2008.

General Description. Experiments were performed by CUBRC in their LENS1 Shock Tunnel to support development of the HiFire flight vehicle whose purpose was to study boundary layer transition, turbulent separated flow and turbulent SWBLI. See Ref.'s A4-1 and A4-2. The configuration consists of a 7 deg half-angle cone, a cylindrical section, a short 33 deg flare and another short flat cylinder aft end. Tests were performed with both sharp and blunt tips. The tests were performed at Mach 7.19 and at a high Reynolds number so that natural transition occurred on the conical section. Working fluid for this experiment was dry Air.

Experimental arrangement. The model geometry is shown below.

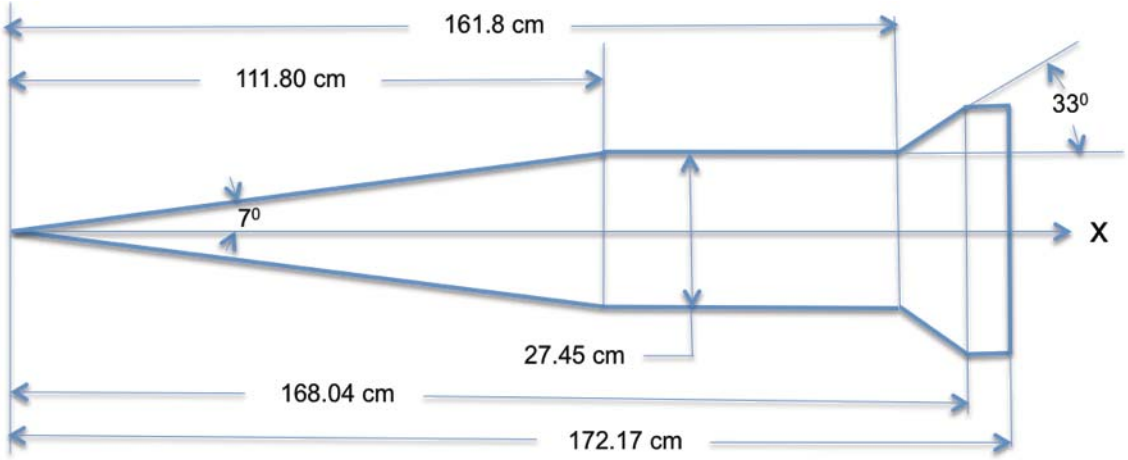

Cone-Cylinder-Flare (HiFire)

The cone tip was replaceable. Tests were performed with a sharp tip and a blunt tip with a 2.5 mm. nose radius. (It should be noted that the data tables list quantities in English units as provided to NASA by the experimenters). The test model was aligned with the free-stream to provide zero incidence data. Some tests were

performed at small angle of attack as part of the program, but no data for these tests are provided herein. (See Ref. A4-2)

Facility. The experimental data was obtained in the CUBRC LENS 1 shock tunnel equipped with a contoured nozzle. See Facility description in Appendix A2, Ref. A4-1 and A4-2. LENS I was constructed with the capability of fully duplicating flight conditions at Mach numbers ranging from 6 to 15 to conduct testing with full-scale versions of missile interceptors and scramjet engines. For the experiments on HiFire listed in this Appendix, the nominal test Mach number was 7.2 and the Reynolds number was 3.1×10^6/ ft. The test conditions were sufficient to cause natural transition on the cone surface and fully developed turbulent flow ahead of the flare.

Measurements. Surface pressure and heat transfer were measured along the entire body surface in a single meridian plane. Additional heat transfer measurements were made along three additional meridian planes. Piezoelectric pressure gauges were employed. These gauges used a diaphragm design and read the model pressure versus a pre-test baseline pressure (differential pressure). In addition, these transducers were mounted close to the surface so that orifice effects and fill times were negligible. The measured pressures were quoted as accurate to within ±3%. Platinum thin-film heat transfer gages, mounted on an insulating substrate, were used to measure heating at closely spaced intervals along the model surface. The quoted estimated accuracy was ± 5%.

Working fluid for this experiment was dry Air.

Data tables.

Table A4-1: Holden HiFire Run Conditions:
Run 30 (2.5mm Radius Blunt Nose Tip) at Mach=7.19; and
Run 36 (Sharp Nose Tip) at Mach=7.163

Condition	Units	Run 30	Run 36
Po	psia	4560	5193
Ho	(ft/sec)**2	2.94E+07	3.37E+07
To	°R	4090	4707.1
M∞	-	7.190	7.163
U∞	ft/sec	7119.5	7740.3
T∞	°R	407.6	471.9
P∞	psia	0.6664	0.6858
Q∞	psia	24.12	24.60
Rho∞	slugs/ft3	1.30E-04	1.18E-04
Re#	1/ft	2.91E+06	2.60E+06
Pitot	psia	44.50	45.40
Qo(F-R)	BTU/Ft2-sec	308.95	382.09
Wall Temperature	°R	534.0	530.6
Nose Radius	mm	2.5	Sharp
Flare Angle	degrees	33	33

Table A4-2: Holden HiFire Wall Pressure Distribution:
Run 30 (2.5mm Radius Blunt Nose Tip) at Mach=7.19; and
Run 36 (Sharp Nose Tip) at Mach=7.163

Location	Run 30	Run 36		Location	Run 30	Run 36
X, inch	P, psia	P, psia		X, inch	P, psia	P, psia
16.892	1.496	1.601		62.503	1.153	1.108
26.834	1.553	1.595		62.658	1.407	1.288
26.834	1.595	1.562		62.813	1.725	1.390
39.342	1.561	1.563		62.968	1.253	1.393
39.342	1.510	1.569		63.123	1.503	1.713
39.342	1.502	1.527		63.278	1.213	1.619
39.342	1.467	1.592		63.433	2.250	2.486
42.217	1.488	1.599		63.588	2.288	2.566
42.217	1.512	1.623		63.813	1.998	2.508
48.516	0.503	0.607		63.943	2.389	4.067
48.516	0.566	0.666		64.073	3.059	5.132
48.516	0.544	0.617		64.203	3.689	5.200
48.516	0.522	0.508		64.333	4.331	6.412
53.266	0.485	0.550		64.463	4.845	7.000
53.266	0.471	0.574		64.593	6.389	7.998
57.516	0.479	0.548		64.723	6.817	9.710
57.516	0.490	0.589		64.853	8.210	10.416
60.643	0.456	0.582		64.983	10.824	11.600
60.953	0.494	0.576		65.113	13.877	14.483
61.108	0.424	0.605		65.503	16.441	18.226
61.263	0.754	0.597		65.633	17.748	19.036
61.418	0.780	0.580		65.763	18.466	19.249
61.573	0.749	0.556		65.893	19.082	18.979
61.728	0.755			66.368	16.831	17.864
61.883	0.835	0.636		66.703	16.972	
62.038	1.542	0.933		67.039	16.605	17.347
62.193	1.343	0.858		67.374	16.598	17.280

Table A4-3: Holden HiFire Wall Heat Transfer Distribution:
Run 30 (2.5mm Radius Blunt Nose Tip) at Mach=7.19; and
Run 36 (Sharp Nose Tip) at Mach=7.163

Location	Run 30	Run 36		Location	Run 30	Run 36
X, inch	Q, Btu/ft2-sec	Q, Btu/ft2-sec		X, inch	Q, Btu/ft2-sec	Q, Btu/ft2-sec
6.848	18.920	24.114		61.883	16.664	14.726
9.892	15.984	37.446		62.038	16.503	16.184
13.892	12.151	62.501		62.193	15.586	21.537
14.892	12.954	60.891		62.348	15.438	24.191
15.892	12.384	57.870		62.503	15.298	26.011
16.892	12.357	56.601		62.658	16.812	25.641
17.892	18.669	54.211		62.813	18.736	22.729
18.892	24.482	51.791		62.968	20.980	25.811
19.892	26.909	52.752		63.123	22.286	28.118
20.892	36.284	51.451		63.278	23.326	33.072
21.892	41.865	51.798		63.433	25.721	30.940
22.761	47.132	49.224		63.588	31.114	38.251
23.631	53.914	49.858		63.813	37.425	49.460
24.672	45.004	50.474		63.943	48.892	64.237
25.257	44.441	49.699		64.073	59.491	80.001
25.842	44.395	50.690		64.203	71.687	101.411
27.827	44.368	48.419		64.333	85.973	126.241
28.842	41.540	49.298		64.463	107.734	150.115
31.842	42.174	48.613		64.593	118.448	165.360
33.342	40.422	47.852		64.723	139.267	191.888
34.842	41.556	48.521		64.853	156.220	212.745
36.342	40.926	48.354		64.983	176.113	236.871
37.842	40.622	46.329		65.113	205.019	267.843
40.842	38.636	46.006		65.243	228.316	276.522
42.217	39.119	46.747		65.373	239.008	295.199
43.592	36.754	45.749		65.503	266.669	309.882
50.016	12.659	15.318		65.633	293.006	331.828
53.016	11.655	14.672		65.763	304.615	331.724
56.016	11.917	15.164		65.893	273.236	324.529
59.016	11.727	14.551		66.368	265.986	308.056
60.643	11.723	15.202		66.535	255.345	304.257
60.798	12.053	15.624		66.703	259.736	310.458
60.953	12.875	16.476		66.871	255.090	306.987
61.108	12.047	14.480		67.039	254.170	301.646
61.263	12.409	14.508		67.206	247.960	291.935
61.418	13.688	15.272		67.374	244.740	278.784
61.573	14.711	14.379		67.542	249.010	271.700
61.728	15.321	12.569		67.710	236.400	261.940

Table A4-4: Holden HiFire Wall Heat Transfer Distribution (90 deg gauges): Run 30 (2.5mm Radius Blunt Nose Tip) at Mach=7.19; and Run 36 (Sharp Nose Tip) at Mach=7.163

Location	Run 30	Run 36		Location	Run 30	Run 36
X, inch	Q, Btu/ft2-sec	Q, Btu/ft2-sec		X, inch	Q, Btu/ft2-sec	Q, Btu/ft2-sec
9.948	15.704	36.302		40.842	38.998	43.482
15.892	12.838	60.467		47.016	15.532	18.407
21.892	43.157	55.283		53.016	11.896	13.679
28.842	42.920	50.140		59.016	11.796	14.028
34.842	39.651	44.929				

Table A4-5: Holden HiFire Wall Heat Transfer Distribution (180 deg gauges): Run 30 (2.5mm Radius Blunt Nose Tip) at Mach=7.19; and Run 36 (Sharp Nose Tip) at Mach=7.163

Location	Run 30	Run 36		Location	Run 30	Run 36
X, inch	Q, Btu/ft2-sec	Q, Btu/ft2-sec		X, inch	Q, Btu/ft2-sec	Q, Btu/ft2-sec
9.948	14.821	33.283		36.342	38.209	46.712
12.892	12.415	62.639		40.842	36.395	41.961
15.892	12.541	60.407		47.016	14.830	17.942
21.892	44.518	53.385		53.016	11.885	14.137
28.842	43.028	51.700		59.016	11.688	13.998
34.842	36.504	45.561				

Table A4-6: Holden HiFire Wall Heat Transfer Distribution (270 deg gauges): Run 30 (2.5mm Radius Blunt Nose Tip) at Mach=7.19; and Run 36 (Sharp Nose Tip) at Mach=7.163

Location	Run 30	Run 36		Location	Run 30	Run 36
X, inch	Q, Btu/ft2-sec	Q, Btu/ft2-sec		X, inch	Q, Btu/ft2-sec	Q, Btu/ft2-sec
9.892	14.436	32.950		40.842	36.707	46.145
15.892	10.386	58.111		47.016	14.428	18.319
21.892	40.647	55.749		53.016	11.854	14.993
28.842	43.399	47.756		59.016	11.694	13.967
34.842	38.742	45.512				

Baseline Computations. Computations follow that provide a baseline for those wanting to compute the experiments documented above. The baseline is intended to facilitate and gage new code development and turbulence model improvements.

These are unpublished solutions provided by D. Prabhu of NASA Ames Research using the 2D/Axisymmetric version of the DPLR Navier-Stokes real-gas code. The single-block grid was 1632 x 364 cells.

Pressures and heat transfer for the 2.5 mm nose radius model is compared with the experiment along the surface as functions of axial distance from the virtual sharp tip in the figures below. Laminar simulations are shown for the conical section. SST turbulence model calculations without compressibility corrections are shown after transition for the remainder of the configuration. Computational transition for the SST model implemented in DPLR occurs as part of the turbulent model kinetic energy development process and, for these calculations the Dhawan-Narasimha transition relation was employed. The first pair of figures shows the values over the entire model length up to and including the flare. The next pair of figures shows the values in the immediate vicinity of the cylinder-flare junction and along the flare to provide a better assessment of the comparison in the turbulent SWBLI region.

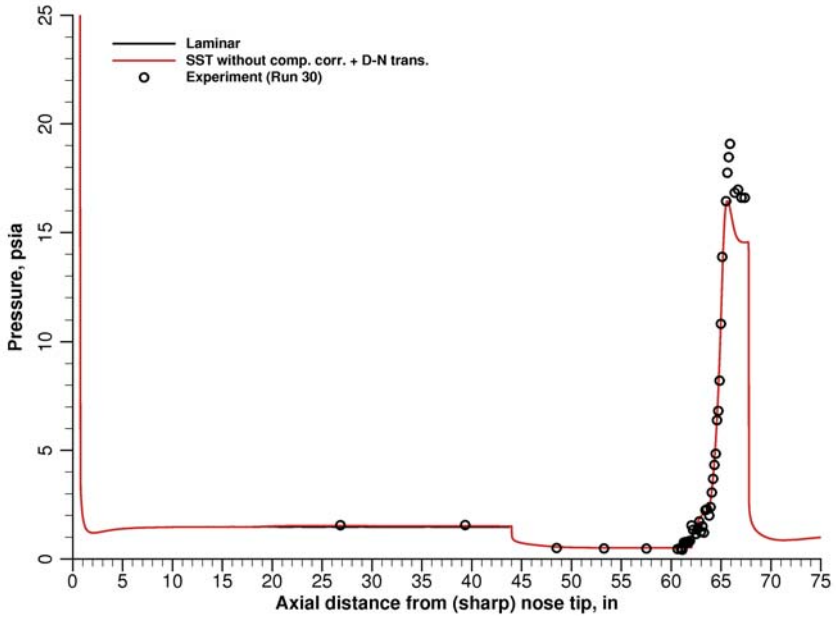

Figure A4-1. Wall Pressure Distribution for Holden Cone-Cylinder-Flare HiFire experiment, Run 30 at Mach 7.19, with 2.5 mm blunt nose tip.

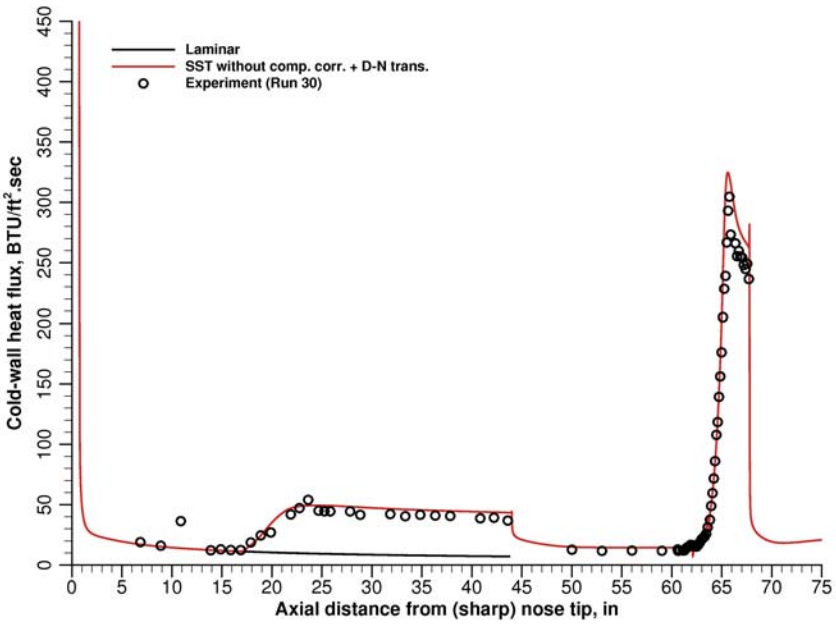

Figure A4-2. Wall Heat Transfer Distribution for Holden Cone-Cylinder-Flare HiFire experiment, Run 30 at Mach 7.19, with 2.5 mm blunt nose tip.

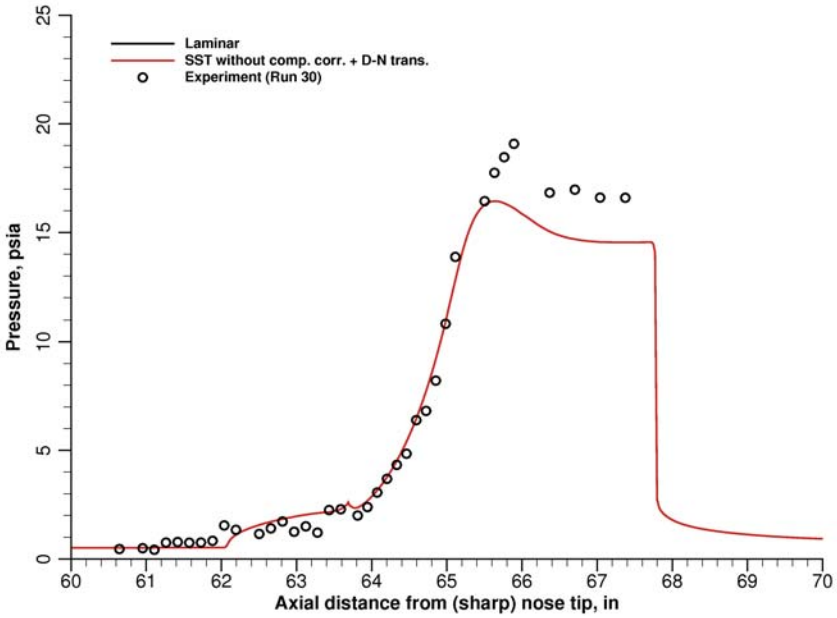

Figure A4-3. Wall Pressure Distribution for Holden Cone-Cylinder-Flare HiFire experiment, Run 30 at Mach 7.19, with 2.5 mm blunt nose tip. . Expanded view about Flare located at X=161.8 cm (~63.7 in).

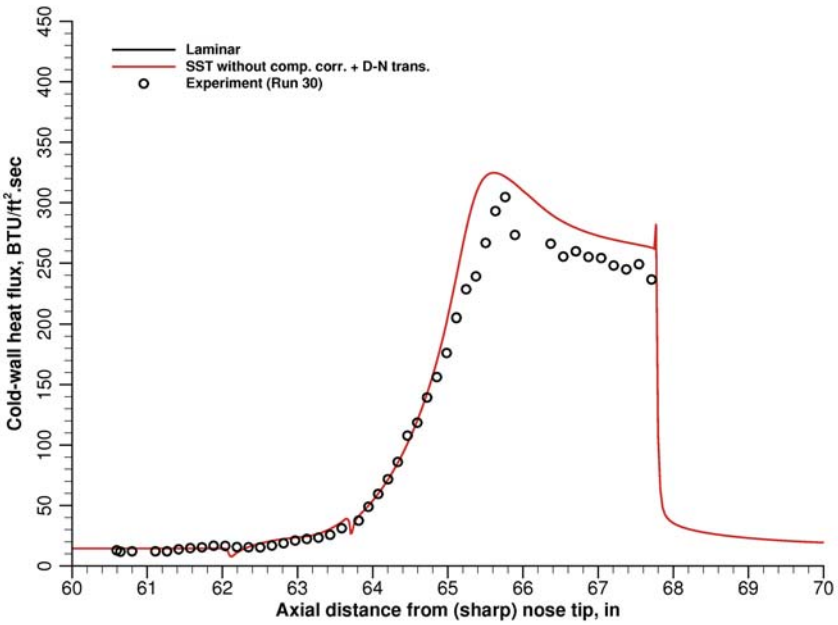

Figure A4-4. Wall Heat Transfer Distribution for Holden Cone-Cylinder-Flare HiFire experiment, Run 30 at Mach 7.19, with 2.5 mm blunt nose tip. Expanded view about Flare located at X=161.8 cm (~63.7 in).

A5. Kussoy and Horstman – Axisymmetric Cone-Cylinder-Flare

Ref. A5-1. Kussoy, M.I. and Horstman, C.C., Documentation of Two- and Three-Dimensional Hypersonic Shock Wave/Turbulent Boundary Layer Interaction Flows, NASA TM 101075, Jan. 1989.

Ref. A5-2. Settles, G.S. and Dodson, L.J., Hypersonic Shock/Boundary-Layer Interaction Database, NASA Contractor Report 177577, April 1991.

Ref. A5-3. Kussoy, M.I. and Horstman, C.C., An Experimental Documentation of a Hypersonic Shock-Wave Turbulent Boundary Layer Interaction Flow - With and Without Separation, NASA TM X-62412, Feb. 1975.

General description This experiment, first reported in Refs. A5-1 and A5-2, was performed in dry Air using an axisymmetric ogive-cylinder body fitted with flares of various angles. Nominal test conditions were M_∞= 7.05, Re_∞= 5.8 x 10^6/m, T_∞= 81.2^{0}K, p_∞= 576 Pa, u_∞=1274m/s, and ρ_∞=0.0252 kg/m^3. Measurements of surface pressure and heat transfer were reported for models with flare angles of 20^0, 30^0, 32.5^0 and 35^0. Also, a boundary layer profile survey was taken on the cylinder ahead of the flare along with three profile surveys throughout the interaction region for the 20^0 flare configuration.

Experimental arrangement. The experimental geometry is shown below.

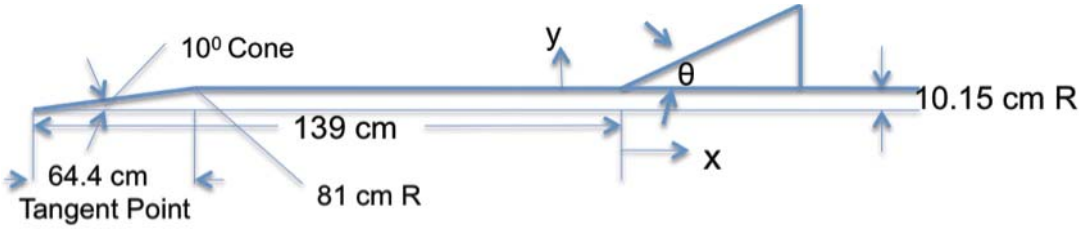

Cone-Ogive-Cylinder-Flare

The model consisted of a 10 degree cone-ogive cylinder, 2 m long and 0.203 m in diameter. The conical forebody was blended onto the cylindrical section at the 64.4 cm location using a circular radius of 81 cm, see Fig. 1 of Ref. A5-3 for details of the ogive nose and cylinder. The model was water-cooled, and model surface temperature was maintained at 310^0 K during each run. Interchangeable instrumentation ports, 12 cm in diameter and specially contoured to fit flush with the cylinder surface, were placed at 25 cm intervals along the cylinder in a single line and at 50 cm intervals in another single line 180^0 away. Individual ports were instrumented with static pressure taps and thermocouples. One port accommodated a survey mechanism to which static pressure, total pressure, and total temperature probes could be attached. Additional static pressure taps and thermocouples were located at 5 cm intervals along the entire length, in a single line 90^0 away from the

instrumentation ports. At several points along the cylinder, static pressure taps were located every 90^0 around it.

Four flares were tested, with half angles (θ) of 20°, 30°, 32.5°, and 35°. The flares were placed on the cylinder at X=139 cm from the cone tip. The flares were fabricated in two halves. A 2.5-cm-wide slit was milled in one of the halves, along its axis. Contoured plates 0.254 cm thick, either blank or instrumented, covered the slit. For the flow survey runs, the 20^0 flare was positioned over the port containing the survey mechanism at the desired stream-wise location and a small access hole was drilled through the contoured cover plate. This access hole accommodated the particular survey probe being used.

Facility. The tests were performed in the Ames Research Center 3.5 Foot Wind tunnel. (Presently inoperable.) This blow-down tunnel consisted of high- pressure cylindrical storage tanks, a ceramic pebble bed heater to prevent air liquefaction, an axisymmetric nozzle with an exit diameter of 1.067 meters, a large free-jet test section and diffuser, and four large diameter evacuated spheres that collected the blown air. The test core diameter was approximately 0.7 m with an axial Mach-number gradient less than 0.12 per meter. The open jet design allowed models to remain outside the stream until the required flow conditions were established. Models were then rapidly inserted, and just as rapidly retracted prior to tunnel shutdown. The test core diameter was approximately 0.7 m. Useful test time was three minutes. Run to run variations in pressure and Mach number was less than 0.5%. The wind tunnel total temperature varied up to 50^0 K from run to run and, in addition, during a single run it varied about 50^0 K over the 3-min test time. These variations required special data reduction procedures described in Ref. A5-1. Natural transition from laminar to turbulent flow is reported to have occurred over the interval of 40 to 80 cm from the model tip.

Measurements. Static pressure taps of 0.16-cm internal diameter were located along the model surface as well as in several instrumentation ports. They were connected with short lengths of stainless steel tubing (10 to 15 cm long) to strain-gauge, absolute-pressure transducers located in the model and calibrated in situ by varying the wind tunnel test-section pressure prior to running the tunnel. A pressure-scanning system was used to obtain accurate measurements of the low static pressures present on the model surface and in the flow field. Before each run, a transducer reading was obtained at the wind tunnel starting pressure (approximately 0.01 am) to determine the zero offset of the gauges. The transducers were water cooled, and all were located within the model.

Surface heat transfer was measured by the transient thin-skin technique. For cylinder surface measurements, chromel-alumel thermocouples were spot-welded to the interior surface, approximately 1 cm apart. These instrumented ports were used to measure the heat transfer upstream of the flare bodies. (In addition, four Schmidt-Boelter heat-transfer gauges were placed in the port upstream of the flares.) Heat transfer was also measured along a ray of each flare surface by

chromel-alumel thermocouples spaced 0.5, 1, or 2 cm apart along the contour plate. For these tests, the entire model was kept at room temperature, then inserted into the flow after the desired flow conditions were obtained. Depending on the thermocouple location, the temperature rise (with model water-cooling system disconnected) varied from 10 to 50 K during a typical 30-sec heat-transfer run. Longitudinal conduction errors were estimated to be less than 5% of the measured convective heat transfer and no corrections were applied.

Pitot and static pressures in the flow field were measured with separate probes calibrated in a free-jet facility by matching Mach number, velocity, and density with the present test conditions. The probes were attached to water-cooled pressure transducers located within the model, connected with a short length (about 8 inch) of stainless steel tubing. See Ref. A5-1 for probe design details.

Total temperatures in the flow field were measured with a probe described in Ref. A5-1 that was comprised of an unshielded, butt-welded chromel-alumel thermocouple supported by tapered chromel and alumel posts. A second chromel-alumel thermocouple was formed at the end of the alumel support to allow simultaneous measurement of the butt-welded thermocouple junction and the probe support. Independent calibrations of these probes in the wind tunnel free stream indicated a maximum total temperature error of 1.5%.

Uncertainties in the surface-pressure and heat-flux measurements were estimated (See Ref. A5.1) to be $\pm$10%. For flow-field quantities, the estimated uncertainties were $\pm$1.5% for the total temperature, $\pm$10% for the static pressure, $\pm$6% for the static temperature, $\pm$12% for the density, and $\pm$3% for the velocity. For the flow-field profiles, the estimated uncertainty in y was $\pm$ 0.02 cm.

Data tables. The data below were taken directly from Ref. A5-1 and repeat the tabulated data from Ref. A5-2. The data files from Ref. A5-2 were provided on a 3-1/4" floppy, now obsolete, and are now duplicated on the DVD accompanying this report. Note for this section on the Kussoy cylinder-flare experiment, X is the stream-wise distance from the cone tip, while S is measured along the wetted test surface, whether along the cylinder or along the flare, from the location of the intersection of the flare with the cylinder (at X=139 cm). Negative S then is simply S=X-139 cm, while positive S is along the flare with S=(X-139)/Cos θ, again in cm, and S=0 indicates the location where the flare is placed on the cylinder. The reported values of Table A5-1 of displacement and momentum thickness for the incoming boundary layer make use of the variation of density in the boundary layer and thus are the compressible displacement and momentum thickness. The tables give wall pressure and heat transfer as normalized by the nominal values for the upstream boundary layer, with P_∞=576 N/m^2 and Q_∞=9300 W/cm^2.

Table A5-1. Free Stream Conditions

M_∞ = 7.05	U_∞= 1274 m/s	T_w= 311° K
ρ_∞= 0.0252 kg/m^3	P_∞= 576 Pa	T_∞= 81.2° K
Re_∞/m = 5.8x 10^6	Pt~34 atm	T_0~ 900° K

Table A5-2. Incoming Boundary Layer Conditions

τ_w=25 N/m^2	$c_{f\infty}$= 1.22E-03	Re_δ = 145000
Qw=9300 W/m^2	$c_{h\infty}$= 0.59E-03	Re_θ = 3800
δ = 2.5 cm	δ^* = 0.74 cm	θ = 0.065 cm

Table A5-3. Separation Location (Oil Flow Method).

θ=Flare Angle	**20°**	**30°**	**32.5°**	**35°**
X_{sep}-X_{flare}	**0**	**0**	**-3.1 cm**	**-6.3 cm**

Table A5-4. Test Cylinder Boundary Layer Profile (X=133 cm).

Y, cm	Mach	u/u_∞	P/P_∞	ρ_0/ρ_∞	T/T_∞	$T_0/T_{0,\infty}$
0.000	0.000	0.000	1.000	0.269	3.711	0.350
0.065	1.547	0.470	1.000	0.217	4.600	0.638
0.093	2.177	0.601	1.000	0.264	3.793	0.690
0.120	2.745	0.699	1.000	0.310	3.223	0.752
0.180	3.111	0.759	1.000	0.338	2.959	0.805
0.250	3.356	0.791	1.000	0.362	2.760	0.830
0.320	3.610	0.822	1.000	0.388	2.576	0.858
0.390	3.835	0.836	1.000	0.424	2.359	0.858
0.460	4.070	0.858	1.000	0.454	2.204	0.877
0.620	4.626	0.896	1.000	0.537	1.862	0.905
0.770	5.248	0.929	1.000	0.643	1.555	0.930
0.940	5.739	0.954	1.000	0.730	1.371	0.954
1.090	6.070	0.967	1.000	0.794	1.260	0.966
1.260	6.340	0.982	1.000	0.839	1.192	0.986
1.450	6.599	0.986	1.000	0.901	1.110	0.986
1.640	6.820	0.992	1.000	0.951	1.051	0.991
1.900	6.962	0.999	1.000	0.978	1.023	1.000
2.150	7.022	1.000	1.000	0.993	1.007	1.000
2.400	7.048	1.000	1.000	1.000	1.000	1.000
2.700	7.050	1.000	1.000	1.000	1.000	1.000
3.000	7.050	1.000	1.000	1.000	1.000	1.000

Table A5-5. Flow Field Surveys - $\theta=20^0$ Flare (S=5.5 cm).

Y, cm	Mach	u/u_∞	P/P_∞	ρ_0/ρ_∞	T/T_∞	$T_0/T_{0,\infty}$
0.000	0.000	0.000	10.539	2.840	3.711	0.350
0.053	2.768	0.763	10.539	2.793	3.774	0.881
0.096	2.800	0.778	10.539	2.745	3.840	0.907
0.145	2.878	0.797	10.539	2.762	3.815	0.931
0.195	2.983	0.812	10.539	2.865	3.679	0.939
0.290	3.266	0.851	10.539	3.126	3.372	0.968
0.395	3.701	0.895	10.120	3.488	2.901	0.992
0.495	3.980	0.914	9.760	3.728	2.618	0.998
0.590	4.043	0.918	9.461	3.692	2.562	1.000
0.790	7.050	1.004	1.000	0.994	1.006	1.006
0.990	7.050	1.004	1.000	0.994	1.006	1.006
1.175	7.050	1.003	1.000	0.996	1.004	1.004
1.360	7.050	1.003	1.000	0.996	1.004	1.004

Table A5-6. Flow Field Surveys - $\theta=20^0$ Flare (S=10.3 cm).

Y, cm	Mach	u/u_∞	P/P_∞	ρ_0/ρ_∞	T/T_∞	$T_0/T_{0,\infty}$
0.000	0.000	0.000	11.976	3.227	3.711	0.350
0.055	2.250	0.718	11.976	2.358	5.079	0.938
0.100	2.859	0.806	11.976	3.031	3.951	0.955
0.140	3.107	0.835	11.976	3.340	3.585	0.963
0.185	3.157	0.840	11.976	3.404	3.519	0.965
0.270	3.253	0.856	11.976	3.485	3.437	0.980
0.360	3.336	0.865	11.976	3.584	3.341	0.986
0.450	3.417	0.875	11.976	3.673	3.260	0.994
0.650	3.605	0.892	11.976	3.939	3.040	1.000
0.850	3.763	0.902	11.976	4.196	2.854	1.000
1.050	3.835	0.904	11.976	4.335	2.763	0.995
1.200	4.089	0.916	9.581	3.848	2.490	0.989
1.420	7.052	1.001	1.000	1.002	0.998	1.001
1.620	7.052	1.001	1.000	1.002	0.998	1.001

Table A5-7. Flow Field Surveys - $\theta=20^0$ Flare (S=15.5 cm).

Y, cm	Mach	u/u_∞	P/P_∞	ρ_0/ρ_∞	T/T_∞	$T_0/T_{0,\infty}$
0.000	0.000	0.000	12.335	3.324	3.711	0.350
0.065	2.533	0.735	12.335	2.948	4.185	0.881
0.083	2.747	0.772	12.335	3.143	3.925	0.906
0.100	2.997	0.810	12.335	3.395	3.633	0.933
0.138	3.121	0.832	12.335	3.495	3.529	0.954
0.169	3.168	0.844	12.335	3.496	3.528	0.972
0.198	3.216	0.852	12.335	3.536	3.489	0.980
0.250	3.286	0.862	12.335	3.606	3.420	0.988
0.300	3.354	0.873	12.335	3.667	3.364	0.999
0.400	3.431	0.880	12.335	3.774	3.268	1.002
0.520	3.486	0.884	12.335	3.861	3.194	1.001
0.660	3.540	0.887	12.335	3.952	3.121	1.000
0.710	3.566	0.889	12.335	3.996	3.087	1.000
0.800	3.613	0.892	12.335	4.072	3.029	1.000
0.900	3.676	0.897	12.335	4.174	2.955	1.000
1.000	3.737	0.901	12.335	4.276	2.885	1.000
1.100	3.777	0.903	12.335	4.344	2.839	1.000
1.200	3.777	0.903	12.335	4.344	2.839	1.000
1.300	3.777	0.903	12.335	4.344	2.839	1.000
1.400	3.777	0.903	12.335	4.344	2.839	1.000
1.500	3.777	0.903	12.335	4.334	2.839	1.000
1.600	3.777	0.901	12.335	4.276	2.885	1.000

Table A5-8. Wall Pressure and Heat Transfer - $\theta=20^0$

S, cm	p_w/p_∞		S, cm	q_w/q_∞
-11.30	0.97		-12.06	0.98
-10.30	0.98		-10.80	1.05
-9.30	0.96		-9.52	1.06
-8.30	0.98		-8.26	1.02
-7.30	0.97		-6.98	1.03
-6.30	0.99		-5.73	1.00
-5.30	1.03		-4.44	1.03
-4.30	1.00		-3.18	1.01
-3.30	1.02		-1.90	0.99
-2.30	1.00		-0.64	0.86
-1.30	1.09		1.10	4.79
1.10	2.02		1.60	4.17
1.60	3.68		2.10	4.99
2.10	5.31		2.60	5.27
2.60	5.96		3.10	5.94
3.60	7.42		3.60	5.74
4.10	8.27		4.60	6.04
4.60	9.10		5.10	7.99
5.10	9.95		6.10	8.59
6.10	10.80		7.10	8.74
7.10	11.30		8.10	8.64
10.10	12.14		9.10	8.77
12.10	12.26		10.10	9.18
14.10	12.50		12.10	9.68
			13.10	9.59
			14.10	9.36
			15.10	8.55

Table A5-9. Wall Pressure and Heat Transfer - $\theta=30^0$

S, cm	p_w/p_∞		S, cm	q_w/q_∞
-11.3	1.00		-12.06	0.99
-10.3	0.98		-10.80	0.99
-9.3	0.97		-9.52	1.00
-8.3	0.98		-8.26	1.00
-7.3	1.00		-6.98	1.01
-6.3	1.00		-5.73	1.01
-5.3	0.98		-4.44	1.00
-4.3	1.02		-3.18	0.99
-3.3	1.09		-1.90	0.99
-2.3	1.39		-0.64	1.02
-1.3	1.73		1.10	8.20
1.1	7.75		1.60	8.97
1.6	9.58		2.10	10.09
2.1	12.85		3.10	12.05
2.6	15.06		3.60	13.42
3.6	19.51		4.60	14.39
4.1	21.33		5.10	15.25
4.6	21.94		6.10	14.86
6.1	22.82		7.10	14.90
7.1	22.88		8.10	14.60
8.1	23.71		9.10	14.75
10.1	24.40		10.10	14.45
12.1	23.62		11.10	14.41
14.1	22.60		12.10	13.98
			13.10	13.02
			14.10	12.87
			15.10	12.21

Table A5-10. Wall Pressure and Heat Transfer - $\theta=32.5^0$

S, cm	p_w/p_∞		S, cm	q_w/q_∞
-11.30	1.01		-12.06	1.00
-10.30	0.99		-10.80	0.99
-9.30	0.98		-9.52	1.00
-8.30	1.01		-8.26	1.01
-7.30	0.97		-6.98	1.03
-6.30	1.01		-5.73	1.01
-5.30	1.03		-4.44	1.05
-4.30	1.12		-3.18	1.09
-3.30	1.23		-1.90	1.33
-2.30	1.71		-0.64	2.16
-1.30	2.56		1.05	6.79
0.55	5.85		1.55	7.44
1.05	7.50		2.05	9.23
1.55	8.42		2.55	10.64
2.05	12.02		3.05	12.82
2.55	14.40		3.55	14.55
3.55	21.19		4.55	16.28
4.05	23.57		5.05	17.05
4.55	25.83		6.05	17.05
6.05	27.14		7.05	16.67
7.05	27.74		8.05	16.41
8.05	27.62		9.05	16.54
10.05	27.74		10.05	15.90
			11.05	15.77

Table A5-11. Wall Pressure and Heat Transfer - $\theta=35^0$

S, cm	p_w/p_∞		S, cm	q_w/q_∞
-11.30	0.97		-12.06	0.99
-10.30	0.98		-10.80	1.07
-9.30	1.00		-9.52	1.00
-8.30	1.15		-8.26	1.04
-7.30	1.45		-6.98	1.02
-6.30	2.01		-5.73	1.26
-5.30	2.53		-4.44	1.83
-4.30	3.25		-3.18	2.39
-3.30	3.63		-1.90	2.63
-2.30	4.41		-0.64	2.55
-1.30	4.56			
1.07	6.95		1.07	6.40
1.57	8.82		1.57	7.90
2.07	11.07		2.07	9.65
2.57	14.05		2.57	11.75
3.07	18.45		3.07	13.82
3.57	21.79		3.57	16.10
4.07	25.71		5.07	20.03
4.57	28.93		6.07	21.96
7.07	33.68		7.07	21.37
8.07	33.69		9.07	19.72
10.07	30.04		10.07	19.97

Baseline Computations. Computations follow that provide a baseline for those wanting to compute the experiments documented above. The baseline is intended to facilitate and gage new code development and turbulence model improvements.

The solution for the Kussoy-Horstman 35 degree compression ramp were conducted by James L. Brown of NASA Ames using DPLR, with a single-block grid specifically adapted for this case by Mike Olsen of NASA Ames. The grid was specified as 3D, but the geometry is axisymmetric. The number of grid cells along the direction of the cylinder was 351, with 256 normal to the cylinder and ramp surface. In the azimuthal direction, the grid covered the quarter-plane (90°) with 18 cells, spaced 5 degrees. Figure A5-1 and A5-2 compare the wall pressure and wall heating along the streamwise direction for DPLR/SST solutions relative to the experimental results. The extent of separation and the level of the wall pressures and wall heating through the separation region agree quite well. At reattachment, however, the SST solutions for both wall pressure and wall heating are significantly overpredicted.

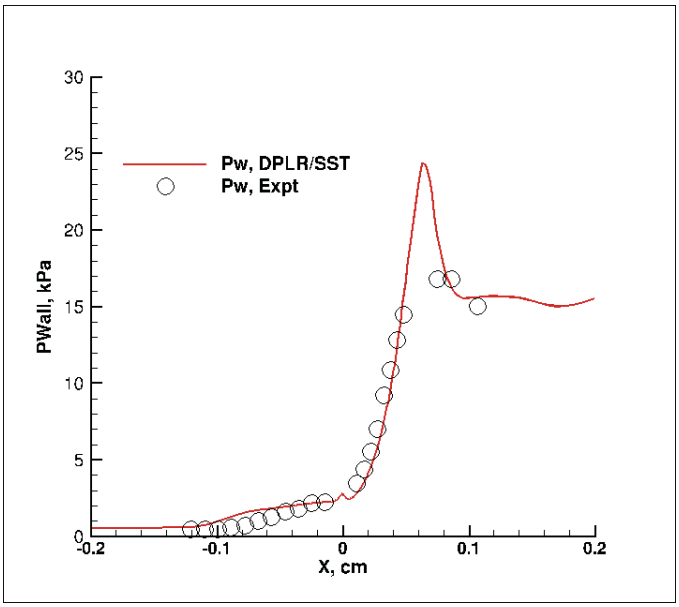

Figure A5-1. Kussoy 35 degree compression corner wall pressure distribution

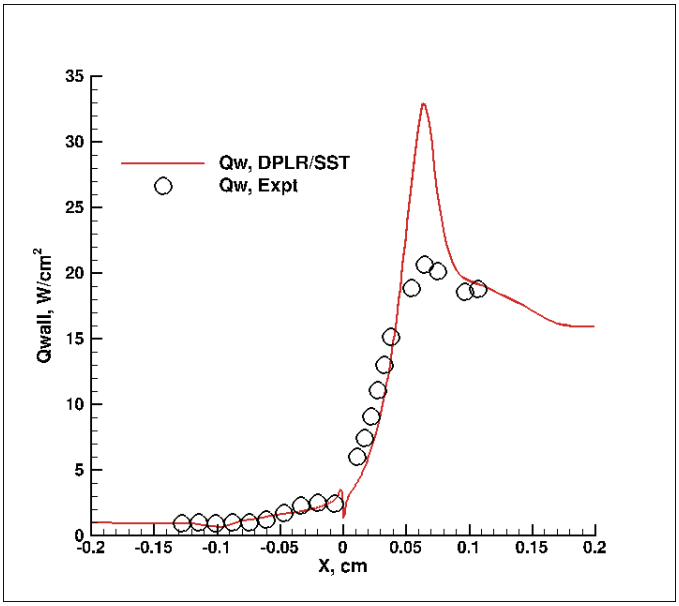

Figure A5-2. Kussoy 35 degree compression corner heat transfer distribution

A6. Hillier-Williams – Axisymmetric Hollow-Cylinder-Flare

Ref. A6-1. Murray, N., Hillier, R. and Williams, S., "Experimental Investigation of Axisymmetric Hypersonic Shock-Wave/Turbulent Boundary-Layer Interactions," Journal of Fluid Mechanics, Vol. 714, Jan. 2, 2013, pp. 152-189.

Ref. A6-2. Williams, N., "Three-Dimensional Separation of a Hypersonic Boundary-Layer," PhD. Thesis, Department of Aeronautics, Imperial College of Science, Technology and Medicine, University of London, 2004.

Ref. A6-3. Mallinson, S.G., Hillier, R., Jackson, A.P., Kirk, D.C., Soltani, S. and Zanchetta, M., "Gun tunnel flow calibration: defining input condition for hypersonic flow computations," Shock Waves, Vol. 10, pp. 313-322, 2000.

Ref. A6-4. Brown, J.L., "Shock Wave Impingement on Boundary Layers at Hypersonic Speeds: Computational Analysis and Uncertainty," AIAA Paper 2011-3143, 42nd AIAA Thermophysics Conference, Honolulu, Hawaii, Jun 27-30, 2011.

General description. The experiment was conducted in the Imperial College Gun Tunnel at a nominal Mach number of 8.9 and free stream Reynolds number of 48 x 10^6 per meter. For this facility, Nitrogen (N_2) is the working fluid. The test surface was a hollow axisymmetric cylinder. The test cylinder axis was aligned lengthwise in the free stream direction, positioned in the center of the test section. An advantage of the axisymmetric configuration is in the elimination of potential spanwise effects. The leading edge protruded slightly into the nozzle exit. A 36 deg flare was positioned on the cylinder at 720 mm from the cylinder leading edge. Naturally developed turbulent flow was achieved well ahead of the interaction. Measurements of cylinder and flare surface pressure and heat transfer along with schlieren photos were taken. Test duration was sufficient to establish steady flow in the interaction region. Database users are encouraged to consult Refs. A6-1 and A6-2 for a complete discussion of these data.

Experimental arrangement. The arrangement is shown in the figure below. The center body is a hollow cylinder 75mm in diameter. It is made up of a combination of sections to provide the desired length with typical total chord length of 800 mm. An instrumented section of the center body allows pressure or heat transfer modules to be inserted along the cylinder so measurements can be made along the entre cylinder. It has a sharp leading edge, with the chamfer directed internally. A 36 deg flare, 86 mm long was mounted at the 720 mm station and instrumented with pressure and heat transfer gages. Measurements were taken at various meridian planes and revealed the flow field was axisymmetric.

Cylinder-Flare

Facility. Tests were performed in the Imperial College Gun Tunnel. See Ref. A6 -3. The tunnel is comprised of three components: a driver section, a piston driven section and an axisymmetric nozzle and dump-tank section. Burst disks that sequentially initiate the flow separate the sections. The nozzle, whose exit diameter is 350 mm, expands the flow to a nominal Mach number of 8.9 test rhombus extending 1.5 m into the tank. The tests were conducted at the highest of three possible pressure conditions to insure a high Reynolds number turbulent flow over the cylindrical centerbody. The resulting nominal conditions in the test rhombus were: $ReU_\infty = 48 \times 10^6$ /m, $T_{(0,\infty)} = 1150^\circ K$, and $P_{(0,\infty)} = 60.8\ MPa$. Nominal wall temperature was $T_{wall}=293^\circ K$. The total run-time was approximately 16 milliseconds, which includes a ramp-up to steady test conditions, steady conditions of 5 milliseconds and a ramp-down. The high-pressure condition leads to a favorable streamwise pressure gradient in the test rhombus, and which is also measured on the test cylinder. (See Ref. A6-3 on the facility calibration.)

Measurements. Pressure measurements along the surface of the cylinder and flare at three meridian planes were taken using Kulite QC series sensors. Care was taken to minimize the sensor response time. Cells were calibrated in situ by adjusting dump tank pressure. Heat transfer measurements were taken using "in-house designed" thin film resistance temperature gauges. Manufacture and module mounting procedures are detailed in Refs. A6-1and A6-2. The heat-transfer gauges were calibrated by wrapping the module in protective latex, immersing them in water heated over an appropriate temperature range, and then determining the corresponding output voltage. An estimate for the worst-case scenario total errors in the pressure and heat-transfer measurements were reported as ±2.3% and +8.7% to –2.2% respectively. Schlieren images of the flow field were recorded with a digital camera during the tests and used to visualize shock interaction structure.

Data tables. Below are data-tables, provided with permission by Dr. Richard Hillier of Imperial College, that give wall pressures and heat transfer on the cylinder and flare surfaces. The nominal tunnel conditions are given in Table A6-1. Note that distance X is the wetted distance along the centerbody surface (parallel to the cylinder axis) and then along the flare surface (tilted at 36°) and that X_{jct} is the wetted distance from the cylinder-flare junction.

Table A6-1: Williams Nominal Tunnel Conditions, N_2 Working Gas.

M_∞=8.9	ReU_∞=48 x10^6/m	$H_{0,\infty}$=1.19 MJ/kg
P_T=60.8 MPa	T_0=1150^{0}K	T_w=293^{0}K
U_∞=1499 m/s	ρ_∞ =0.1510 kg/m^3	T_∞=68.3^{0}K

Table A6-2: Williams Cylinder-Flare Wall Pressure Distribution.

X, mm	X_{jct}, mm	P, kPa		X, mm	X_{jct}, mm	P, kPa		X, mm	X_{jct}, mm	P, kPa
620.0	-100.0	3.10		648.0	-72.0	2.92		679.8	-40.2	4.47
620.5	-99.5	3.11		648.5	-71.5	2.92		680.0	-40.0	3.50
621.0	-99.0	3.10		649.0	-71.0	2.91		680.0	-40.0	3.58
622.0	-98.0	3.07		650.0	-70.0	2.94		680.5	-39.5	3.98
623.0	-97.0	3.09		650.0	-70.0	2.92		680.8	-39.2	5.15
623.5	-96.5	3.08		650.5	-69.5	2.94		681.0	-39.0	3.79
624.0	-96.0	3.08		651.0	-69.0	2.94		681.8	-38.2	4.64
625.0	-95.0	2.98		652.0	-68.0	2.90		682.0	-38.0	4.48
625.0	-95.0	3.10		653.0	-67.0	2.92		682.3	-37.7	5.85
625.5	-94.5	3.01		653.5	-66.5	2.92		682.8	-37.2	4.99
626.0	-94.0	3.01		654.0	-66.0	2.91		683.0	-37.0	5.25
627.0	-93.0	2.95		655.0	-65.0	2.97		683.5	-36.5	4.89
628.0	-92.0	2.98		655.0	-65.0	2.93		683.8	-36.2	6.55
628.5	-91.5	2.98		655.5	-64.5	2.95		684.0	-36.0	5.00
629.0	-91.0	2.97		656.0	-64.0	2.95		685.0	-35.0	6.33
630.0	-90.0	2.96		657.0	-63.0	2.91		685.5	-34.5	7.22
630.0	-90.0	2.98		658.0	-62.0	2.91		686.0	-34.0	7.09
630.5	-89.5	3.00		658.5	-61.5	2.92		687.0	-33.0	7.00
631.0	-89.0	3.00		659.0	-61.0	2.92		688.0	-32.0	8.19
632.0	-88.0	2.96		660.0	-60.0	2.96		688.5	-31.5	8.24
633.0	-87.0	2.98		660.0	-60.0	2.93		688.8	-31.2	8.87
633.5	-86.5	2.98		660.5	-59.5	2.97		689.0	-31.0	8.41
634.0	-86.0	2.97		661.0	-59.0	2.96		689.3	-30.7	10.70
635.0	-85.0	2.95		662.0	-58.0	2.93		689.8	-30.2	10.46
635.0	-85.0	2.99		663.0	-57.0	2.93		690.0	-30.0	10.74
635.5	-84.5	2.99		663.5	-56.5	2.95		690.0	-30.0	10.02
636.0	-84.0	2.99		664.0	-56.0	2.94		690.5	-29.5	10.45
637.0	-83.0	2.94		665.0	-55.0	2.96		690.8	-29.2	12.10
638.0	-82.0	2.97		668.8	-51.2	2.88		691.0	-29.0	11.12
638.5	-81.5	2.97		669.3	-50.7	2.89		691.8	-28.2	10.94
639.0	-81.0	2.96		669.8	-50.2	2.88		692.0	-28.0	10.05
640.0	-80.0	2.97		670.8	-49.2	2.84		692.3	-27.7	12.51
640.0	-80.0	2.97		671.8	-48.2	2.83		693.0	-27.0	11.13
640.5	-79.5	2.97		672.3	-47.7	2.85		693.5	-26.5	11.69
641.0	-79.0	2.96		672.8	-47.2	2.84		693.8	-26.2	12.88
642.0	-78.0	2.93		673.8	-46.2	2.92		694.0	-26.0	11.73
643.0	-77.0	2.94		675.0	-45.0	2.95		695.0	-25.0	11.75
643.5	-76.5	2.95		675.5	-44.5	3.22		695.0	-25.0	12.04
644.0	-76.0	2.94		676.0	-44.0	2.93		695.5	-24.5	11.80
645.0	-75.0	2.94		677.0	-43.0	2.94		696.0	-24.0	12.65
645.0	-75.0	2.96		678.0	-42.0	3.10		697.0	-23.0	12.09
645.5	-74.5	2.94		678.5	-41.5	3.00		698.0	-22.0	12.40
646.0	-74.0	2.94		678.8	-41.2	3.26		698.5	-21.5	13.09
647.0	-73.0	2.89		679.0	-41.0	3.13		698.8	-21.2	12.80

Table A6-2 Continued: Williams Cylinder-Flare Wall Pressure Distribution.

X, mm	X_{jct}, mm	P, kPa		X, mm	X_{jct}, mm	P, kPa		X, mm	X_{jct}, mm	P, kPa
699.0	-21.0	12.84		718.0	-2.0	14.66		750.0	30.0	145.46
699.3	-20.7	12.87		718.5	-1.5	15.18		750.5	30.5	151.12
699.8	-20.2	13.02		719.0	-1.0	15.84		751.5	31.5	150.79
700.0	-20.0	12.95		720.0	0.0	15.34		752.0	32.0	139.82
700.0	-20.0	13.00		724.5	4.5	15.00		752.5	32.5	155.58
700.5	-19.5	12.81		725.0	5.0	14.76		753.0	33.0	169.24
700.8	-19.2	13.08		725.5	5.5	15.65		753.5	33.5	182.99
701.0	-19.0	13.13		726.0	6.0	16.32		754.5	34.5	187.89
701.8	-18.2	12.98		727.5	7.5	17.87		755.0	35.0	183.40
702.0	-18.0	13.06		728.0	8.0	16.89		755.5	35.5	179.06
702.3	-17.7	13.50		728.5	8.5	17.45		756.0	36.0	181.46
702.8	-17.2	13.40		729.0	9.0	20.50		756.5	36.5	196.89
703.0	-17.0	13.16		729.5	9.5	20.12		757.5	37.5	189.97
703.5	-16.5	13.81		730.5	10.5	21.92		758.0	38.0	189.73
703.8	-16.2	13.45		731.0	11.0	22.26		758.5	38.5	178.30
704.0	-16.0	13.46		731.5	11.5	23.40		759.0	39.0	154.85
705.0	-15.0	13.23		732.0	12.0	23.76		759.5	39.5	156.66
705.0	-15.0	13.48		732.5	12.5	23.84		760.5	40.5	148.92
705.5	-14.5	13.31		733.5	13.5	29.39		761.0	41.0	145.46
706.0	-14.0	13.77		734.0	14.0	25.99		761.5	41.5	147.12
707.0	-13.0	13.28		734.5	14.5	26.27		762.0	42.0	146.31
708.0	-12.0	13.64		735.0	15.0	33.25		762.5	42.5	145.00
708.5	-11.5	13.93		736.5	16.5	36.32		763.5	43.5	148.94
709.0	-11.0	13.79		737.0	17.0	37.39		764.0	44.0	149.23
709.0	-11.0	14.49		737.5	17.5	38.74		764.5	44.5	144.59
710.0	-10.0	13.91		738.0	18.0	41.16		765.0	45.0	135.13
710.0	-10.0	13.87		738.5	18.5	41.34		765.5	45.5	136.05
710.0	-10.0	14.19		739.5	19.5	47.30		766.5	46.5	132.40
710.5	-9.5	14.06		740.0	20.0	42.47		767.0	47.0	131.61
711.0	-9.0	14.27		740.5	20.5	45.93		767.5	47.5	132.17
711.0	-9.0	14.19		741.0	21.0	57.50		768.0	48.0	130.13
712.0	-8.0	13.77		742.5	22.5	68.34		768.5	48.5	127.99
712.0	-8.0	14.38		743.0	23.0	67.41		769.5	49.5	130.37
712.5	-7.5	14.63		743.5	23.5	74.52		770.0	50.0	131.51
713.0	-7.0	14.01		744.0	24.0	74.39		770.5	50.5	128.52
713.0	-7.0	14.48		744.5	24.5	79.51		771.0	51.0	126.88
713.5	-6.5	14.18		745.5	25.5	85.94		771.5	51.5	125.86
714.0	-6.0	14.11		746.0	26.0	77.34		772.5	52.5	125.81
714.0	-6.0	14.81		746.5	26.5	86.59		773.0	53.0	123.81
715.0	-5.0	14.05		747.0	27.0	104.92		773.5	53.5	124.54
715.0	-5.0	14.22		747.5	27.5	114.32		774.0	54.0	123.24
715.5	-4.5	14.23		748.5	28.5	132.46		774.5	54.5	118.85
716.0	-4.0	14.70		749.0	29.0	129.88		775.5	55.5	125.67
717.0	-3.0	14.57		749.5	29.5	137.55		776.0	56.0	126.87

Table A6-2 Concluded: Williams Cylinder-Flare Wall Pressure Distribution.

X, mm	X_{jct}, mm	P, kPa		X, mm	X_{jct}, mm	P, kPa		X, mm	X_{jct}, mm	P, kPa
776.5	56.5	126.32		782.5	62.5	125.38		788.5	68.5	123.21
777.0	57.0	123.53		783.0	63.0	123.81		789.0	69.0	122.35
777.5	57.5	122.74		783.5	63.5	123.76		789.5	69.5	122.55
778.5	58.5	123.34		784.5	64.5	123.26		790.5	70.5	122.62
779.0	59.0	122.51		785.0	65.0	122.16		791.0	71.0	122.69
779.5	59.5	122.59		785.5	65.5	122.76		791.5	71.5	122.11
780.0	60.0	122.16		786.0	66.0	120.74		792.0	72.0	121.60
780.5	60.5	119.28		786.5	66.5	118.37		792.5	72.5	120.37
781.5	61.5	124.08		787.5	67.5	122.70				
782.0	62.0	125.84		788.0	68.0	122.93				

Table A6-3: Williams Cylinder-Flare Wall Heat Transfer Distribution.

X,mm	X_{jct},mm	Q, W/cm^2		X,mm	X_{jct},mm	Q, W/cm^2		X,mm	X_{jct},mm	Q, W/cm^2
644.9	-75.2	6.04		663.9	-56.2	5.75		682.4	-37.7	13.44
645.4	-74.7	6.02		664.4	-55.7	5.87		682.8	-37.3	13.14
645.9	-74.2	6.10		664.9	-55.2	5.93		683.3	-36.8	13.23
646.4	-73.7	5.99		665.3	-54.8	5.85		683.8	-36.3	11.64
646.9	-73.2	5.79		665.4	-54.7	5.88		684.3	-35.8	14.40
647.4	-72.7	5.98		665.8	-54.3	5.86		684.8	-35.3	14.20
647.9	-72.2	6.05		666.3	-53.8	5.82		685.3	-34.8	14.32
648.3	-71.8	6.15		666.8	-53.3	5.88		685.7	-34.4	14.83
648.4	-71.7	5.92		667.3	-52.8	5.67		685.8	-34.3	15.50
648.8	-71.3	6.09		667.8	-52.3	5.84		686.2	-33.9	15.47
649.3	-70.8	6.12		668.3	-51.8	5.87		686.7	-33.4	15.13
649.8	-70.3	6.13		668.7	-51.4	5.87		687.2	-32.9	15.10
650.3	-69.8	5.82		668.8	-51.3	5.82		687.7	-32.4	14.34
650.8	-69.3	6.02		669.2	-50.9	5.90		688.2	-31.9	13.98
651.3	-68.8	6.09		669.7	-50.4	5.82		688.7	-31.4	15.09
651.7	-68.4	5.90		670.2	-49.9	5.93		689.1	-30.9	14.60
651.8	-68.3	6.02		670.7	-49.4	5.62		689.2	-30.9	14.16
652.2	-67.9	5.94		671.2	-48.9	5.80		689.6	-30.5	14.05
652.7	-67.4	5.80		671.7	-48.4	5.88		690.1	-30.0	15.05
653.2	-66.9	5.90		672.1	-48.0	5.69		690.6	-29.4	15.18
653.7	-66.4	5.64		672.2	-47.9	5.75		691.1	-29.0	12.80
654.2	-65.9	5.81		672.6	-47.5	5.81		691.6	-28.5	12.65
654.7	-65.4	5.86		673.1	-47.0	5.52		692.1	-28.0	13.18
655.1	-65.0	6.18		673.6	-46.5	5.82		692.5	-27.6	13.40
655.2	-64.9	5.73		674.1	-46.0	5.46		692.6	-27.5	13.11
655.6	-64.5	6.17		674.6	-45.5	5.74		693.0	-27.1	11.44
656.1	-64.0	6.14		675.1	-45.0	5.66		693.4	-26.6	12.53
656.6	-63.5	6.14		675.5	-44.6	6.00		694.0	-26.1	12.63
657.1	-63.0	5.96		675.6	-44.5	5.33		694.5	-25.6	10.93
657.6	-62.5	6.07		676.0	-44.1	5.24		695.0	-25.1	11.93
658.1	-62.0	6.17		676.5	-43.6	5.76		695.5	-24.6	12.26
658.5	-61.6	5.85		677.0	-43.1	5.23		695.9	-24.2	12.18
658.6	-61.5	6.03		677.5	-42.6	7.01		695.9	-24.1	12.01
659.0	-61.1	5.92		678.0	-42.1	7.25		696.4	-23.7	10.86
659.5	-60.6	5.76		678.5	-41.6	5.30		696.9	-23.2	11.87
660.0	-60.1	5.91		678.9	-41.2	6.92		697.4	-22.7	12.42
660.5	-59.6	5.65		679.0	-41.1	8.85		697.9	-22.2	10.72
661.0	-59.1	5.79		679.4	-40.7	7.66		698.4	-21.7	11.12
661.5	-58.6	5.93		679.9	-40.2	7.51		698.9	-21.2	11.17
661.9	-58.2	5.96		680.4	-39.7	6.37		699.3	-20.8	11.49
662.0	-58.1	5.79		680.9	-39.2	11.86		699.4	-20.7	10.77
662.4	-57.7	5.92		681.4	-38.7	11.06		699.8	-20.3	11.46
662.9	-57.2	5.86		681.9	-38.2	8.59		700.3	-19.8	11.08
663.4	-56.7	5.96		682.3	-37.8	11.90		700.8	-19.3	10.97

Table A6-3 Continued: Williams Cylinder-Flare Wall Heat Transfer Distribution.

X,mm	X_{jct},mm	Q, W/cm^2		X,mm	X_{jct},mm	Q, W/cm^2		X,mm	X_{jct},mm	Q, W/cm^2
701.3	-18.8	10.56		725.8	5.8	26.00		752.3	32.3	203.20
701.8	-18.3	11.15		726.8	6.8	25.50		752.8	32.8	188.00
702.3	-17.8	11.13		727.3	7.3	28.30		753.8	33.8	227.50
702.7	-17.4	9.82		727.8	7.8	31.00		754.3	34.3	228.10
702.8	-17.3	10.83		728.3	8.3	35.40		754.8	34.8	220.30
703.2	-16.9	9.39		728.8	8.8	37.70		755.3	35.3	221.00
703.7	-16.4	10.39		729.8	9.8	34.60		755.8	35.8	191.20
704.2	-15.9	10.45		730.3	10.3	38.10		756.8	36.8	225.40
704.7	-15.4	9.56		730.8	10.8	41.90		757.3	37.3	214.30
705.2	-14.9	9.79		731.3	11.3	45.90		757.8	37.8	210.10
705.7	-14.4	9.98		731.8	11.8	50.10		758.3	38.3	194.40
706.1	-14.0	10.83		732.8	12.8	46.30		758.8	38.8	187.60
706.2	-13.9	10.37		733.3	13.3	50.00		759.8	39.8	197.70
706.6	-13.5	11.09		733.8	13.8	52.50		760.3	40.3	195.50
707.1	-13.0	11.23		734.3	14.3	58.20		760.8	40.8	188.60
707.6	-12.5	11.89		734.8	14.8	61.10		761.3	41.3	179.70
708.1	-12.0	11.37		735.8	15.8	64.00		761.8	41.8	174.60
708.6	-11.5	11.36		736.3	16.3	64.40		762.8	42.8	183.20
709.1	-11.0	11.92		736.8	16.8	69.50		763.3	43.3	184.40
709.5	-10.6	11.81		737.3	17.3	76.70		763.8	43.8	176.20
709.6	-10.5	12.26		737.8	17.8	81.90		764.3	44.3	169.20
710.0	-10.1	11.54		738.8	18.8	77.30		764.8	44.8	171.80
710.5	-9.6	11.89		739.3	19.3	81.10		765.8	45.8	172.70
711.0	-9.1	11.84		739.8	19.8	88.20		766.3	46.3	172.70
711.5	-8.6	12.57		740.3	20.3	93.80		766.8	46.8	165.80
712.0	-8.1	12.59		740.8	20.8	100.00		767.3	47.3	156.30
712.5	-7.6	12.82		741.8	21.8	96.40		767.8	47.8	160.30
712.9	-7.2	12.71		742.3	22.3	107.60		769.3	49.3	166.40
713.0	-7.1	13.70		742.8	22.8	106.00		769.8	49.8	160.30
713.4	-6.7	13.22		743.3	23.3	126.60		770.3	50.3	161.40
713.9	-6.2	12.99		743.8	23.8	124.30		771.8	51.8	161.50
714.4	-5.7	13.89		744.8	24.8	123.10		772.3	52.3	164.30
714.9	-5.2	14.34		745.3	25.3	128.10		772.8	52.8	157.70
715.4	-4.7	14.84		745.8	25.8	137.20		773.3	53.3	152.90
716.3	-3.8	14.35		746.3	26.3	145.10		773.8	53.8	158.30
716.8	-3.3	15.76		746.8	26.8	159.50		774.8	54.8	157.00
717.3	-2.8	15.80		747.8	27.8	155.30		775.3	55.3	158.60
717.8	-2.3	16.66		748.3	28.3	163.60		775.8	55.8	153.50
722.3	2.3	17.80		748.8	28.8	174.50		776.3	56.3	149.20
722.8	2.8	18.70		749.3	29.3	179.70		776.8	56.8	151.80
723.8	3.8	17.60		749.8	29.8	185.40		777.8	57.8	155.40
724.3	4.3	20.40		750.8	30.8	192.10		778.3	58.3	154.00
724.8	4.8	20.80		751.3	31.3	199.00		778.8	58.8	152.80
725.3	5.3	24.10		751.8	31.8	203.30		779.3	59.3	147.40

Table A6-3 Concluded: Williams Cylinder-Flare Wall Heat Transfer Distribution.

X,mm	X_{jct},mm	Q, W/cm^2		X,mm	X_{jct},mm	Q, W/cm^2		X,mm	X_{jct},mm	Q, W/cm^2
779.8	59.8	150.50		784.3	64.3	142.00		788.3	68.3	136.60
780.8	60.8	149.40		784.8	64.8	142.20		788.8	68.8	140.00
781.3	61.3	147.70		785.3	65.3	135.60		789.8	69.8	142.70
781.8	61.8	147.90		785.8	65.8	138.90		790.3	70.3	141.30
782.3	62.3	141.60		786.8	66.8	144.30		790.8	70.8	137.50
782.8	62.8	145.30		787.3	67.3	142.80		791.3	71.3	131.60
783.8	63.8	143.60		787.8	67.8	141.60		791.8	71.8	138.20

Baseline Computations. Selected computations follow that provide a baseline for those wanting to compute the experiments documented above. These computations were accomplished using the NASA DPLR real-gas Navier-Stokes code and SST turbulence model similar to the approach used for the related Murray impinging SWBLI of Ref. A6-4.

Although the flow is axisymmetric, all solutions provided made use of the 3D formulation of DPLR. The grid for the separated case made use of a single grid block having 992 cells streamwise and 256 cells normal to the test surface. A quarter-plane (90°) grid was used for the axisymmetric problem with cells placed every 10°. The spacing of the first cell off the cylinder surface was at $y_1^+ \cong 0.01$. Transition was specified to agree with the location and extent observed in the wall heating data from Ref. A6-1.

The facility calibration data presented by Mallinson et al. was used in the baseline DPLR solutions to account for the "weak" favorable pressure gradient in the facility test section, present at the high Reynolds number condition used for these test data. One method for accounting for this is discussed in Ref. A6-4 and herein in Appendix B3 for the related Murray experiment.

Keyes viscosity relationship for Nitrogen, N_2, was used for all computations, where:

$$\mu = A\, T^{0.5}/(1.0+(B/T)*10^{(-C/T)})$$

Keyes viscosity constants for molecular Nitrogen(N_2) are: A =1.418 10^{-6}, B =116.4 K, and C = 5.0 K; while for dry air, they are A =1.458 10^{-6}, B =122.1 K, and C = 5.0 K. The units for dynamic viscosity are kg/(m-sec) (also Pa-sec, or equivalently N-sec/m^2), and temperature is specified in degrees Kelvin.

Example DPLR input files, inlet pointwise boundary condition files and ascii plot3d grid files may be found on the companion DVD of this document. (For the present simulation, the nominal freestream conditions appearing in the DPLR input deck are not used as they are overwritten by the values appearing in the pointwise boundary condition files generated so as to describe the slight divergence of the freestream streamlines, see the program BCFaceGen.f located on the accompanying DVD.)

Figures A6-1 and A6-2 compare the experimental and DPLR simulation for the wall pressure and wall heating, respectively. Separation extent on the cylinder, peak pressures and heating on the flare are over predicted.

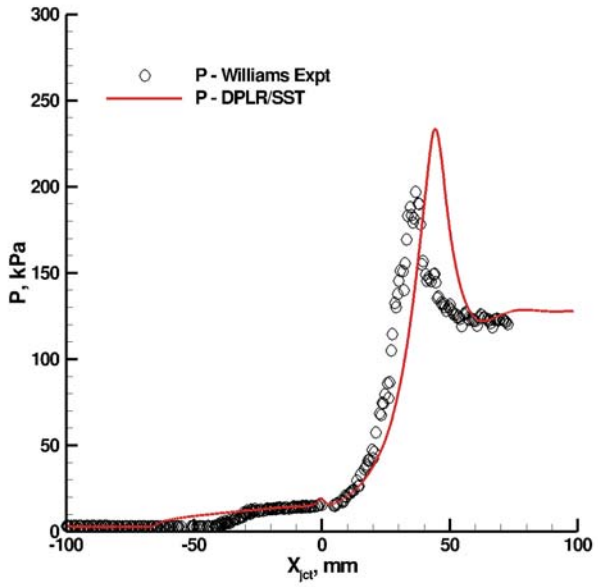

Figure A6-1. Wall Pressure Distribution for Williams 36° Compression Corner at Mach 8.9

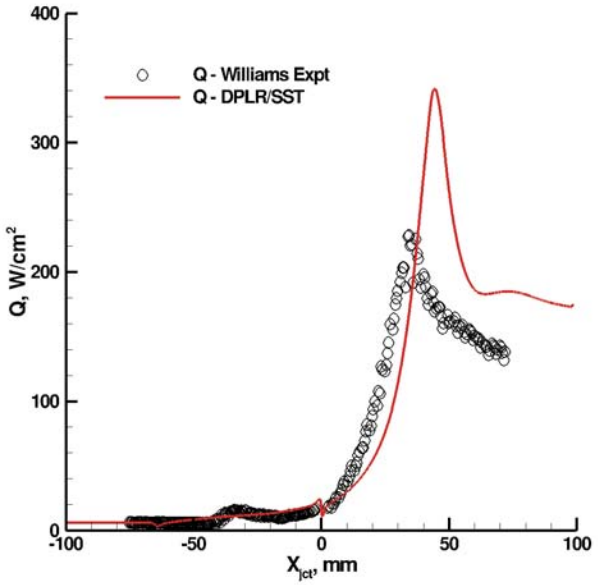

Figure A6-2. Wall Heat Transfer Distribution for Williams 36° Compression Corner at Mach 8.9

Appendix B: Impinging Shock Waves (2-D and Axisymmetric)

B1. Schülein - 2D Impinging Shock

Ref. B1-1. Schülein, E., Krogmann, P. and Stanewsky, E., "Documentation of Two-Dimensional Impinging Shock/Turbulent Boundary Layer Interaction Flow," DLR, German Aerospace Center, Report IB 223-96 A 49, Gottingen, Germany, Oct., 1996.

Ref. B1-2. Schülein, E., "Skin-Friction and Heat Flux Measurements in Shock/Boundary-Layer Interaction Flows," AIAA Journal, Vol. 44, No. 8, August 2006, pp. 1732-1741.

Ref. B1-3. Ludwig, H., Hottner, Th. and Grauer-Carsten, H., Der Rohrwindkanal der Areodynamischen Versuchsansstalt Gottingen. Jahrbuch 1969 der DGLR (1970). Pp. 52-58.

Ref. B1-4. Tanner, L. and Blows, L., "A Study of the Motion of Oil Films on Surfaces in Air Flow, with Application to the Measurement of Skin Friction," Journal of Physics, E: Scientific Instruments, Vol. 8, No. 3, 1976, pp. 194-202.

Ref. B1-5. Naughton, J.W. and Sheplak, M. "Modern Developments in Shear Stress Measurement," Progress in Aerospace Sciences, Vol. 38, Issue 6-7, pp. 515-570, 2002.

Ref. B1-6. Bose, D., Brown, J.L., Prabhu, D.K., Gnoffo, P.A., Johnston, C.O. and Hollis, B., "Uncertainty Assessment of Hypersonic Aerothermodynamics Prediction Capability," AIAA Paper 2011-3141, 42nd AIAA Thermophysics Conference, Honolulu, Hawaii, June 27-30, 2011.

Ref. B1-7. Brown, J.L., "Shock Wave Impingement on Boundary Layers at Hypersonic Speeds: Computational Analysis and Uncertainty", AIAA Paper 2011-3143, 42nd AIAA Thermophysics Conference, Honolulu, Hawaii, June 27-30, 2011.

General Description. Experiments were conducted in the DLR Gottingen Ludwieg Tube Wind Tunnel (RWG, Tunnel B) at a nominal Mach number of 5.0 and free stream Reynolds number of 37 x 10^6 per meter. The facility was equipped with an axisymmetric contoured nozzle and test section. A sharp leading edge test plate was positioned in the center of the test rhombus. The shock generator plate was positioned above the test plate and located axially so that the generated shock impinged on the surface at the same distance from the test plate leading edge for all shock generator angles. Test results are reported in references B1-1 and B1-2.

Experimental Arrangement. A sketch of the test arrangement taken from Ref. B1-2 is shown below. The test plate was 500 mm long and 400 mm wide. The shock

generator plate was 300 mm long and 400 mm wide. The generator was inclined at various angles, β, to generate shock interactions that created attached through separated flows. Generator angles employed were 0, 6, 8, 10, 12, and 14 degrees. The generator axial and normal position with respect to the test plate was varied for each test arrangement such that the location of the inviscid shock interaction was always fixed at 350mm from the plate leading edge. The plate was instrumented for measuring pressures, heat transfer and skin friction and encompassed the entire flow region ahead and throughout the interaction. The test model wall temperature was 300 $\pm$ 5^0K. Boundary layer surveys were made at 10 stream-wise positions along the plate and encompassed the flow locations ahead of and throughout the interaction.

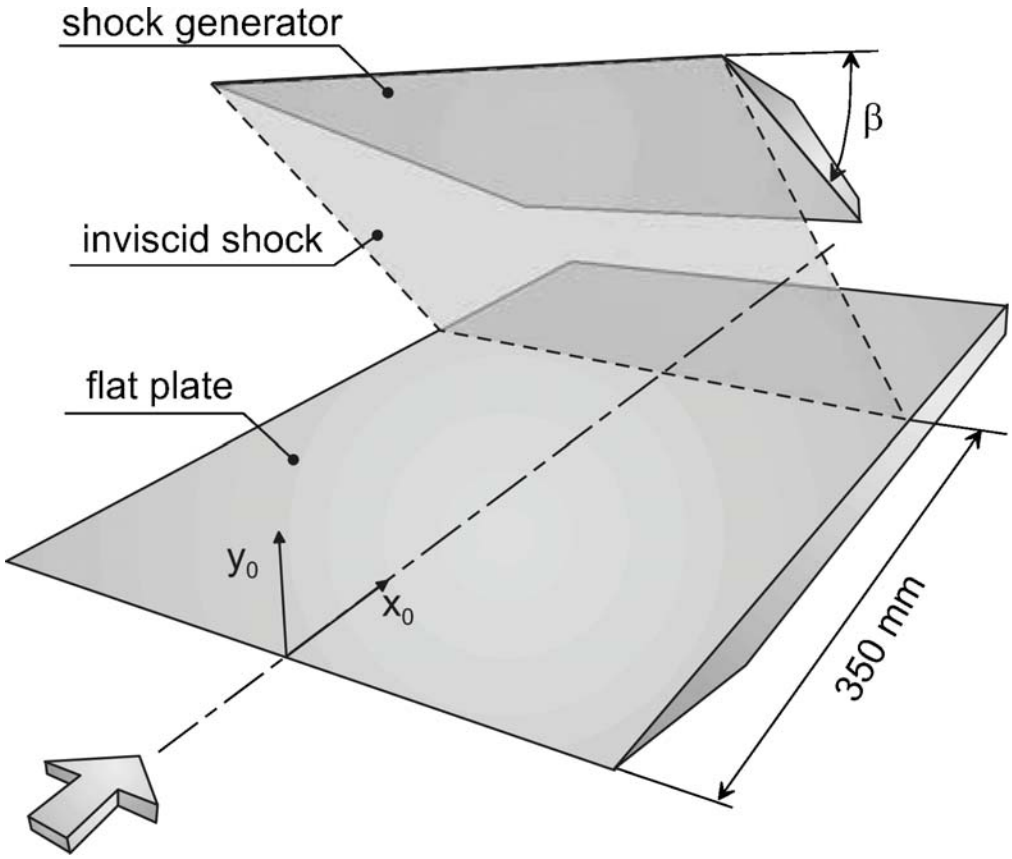

Facility. The experiments were performed in the DLR Ludwieg Tube Wind Tunnel (RWG, Tunnel B). See Ref. B1-2. The tunnel operational concept was developed by Ludwig (Ref. B1-3) for high Reynolds number supersonic testing. The facility was comprised of a 80 m long storage tube, a contoured axisymmetric nozzle equipped with a quick opening gate valve ahead of the throat, a 500 mm diameter test section and a vacuum dump tank. The test medium was dry Air and perfect gas conditions apply. Test times were about 300ms. The nominal free stream test section conditions were: M= 5, T_0=410K, P_0=2.12 MPa, and free stream Re=37x10^6/m. Run-to-run uncertainty in free stream Mach number and velocity are estimated to be less than 0.5% and 2% for static temperature.

Measurements. Surface pressures, skin friction, heat transfer, schlieren and velocity profiles were measured on the test plate. The upstream boundary layer was developed over a distance of 0.350 m ahead of the interaction in order to insure a naturally and fully developed turbulent boundary layer. The instrumentation included Pressure Systems, Inc. 32-port modules for the measurement of pressures. A total of 67 surface pressures were measured along the plate and at four span locations to confirm 2-dimensionality. Pitot and static pressures were measured ahead and throughout the interaction region. Endevco and Kulite transducers were employed. Probe position was reported to within +/-0.05mm. The skin friction measurements were obtained by independent redundant approaches; (1) (GISF) Global Interferometer Skin Friction, a surface oil-film technique(Refs. B1-4 and B1-5) and, (2) using the well-established indirect log-law-wall deduction of wall skin friction from the static and pitot probe measurements. The wall heating was measured with the thin skin thermocouple technique. The experimental uncertainties are quoted as approximately 2% for pressures, 4% to 10% for skin friction, and 5% for heat transfer. High-quality schlieren flow visualization was obtained for all cases.

Data tables. Below are data-tables, provided with permission by Dr. Erich Schülein of DLR, that give wall pressures, heat transfer, and skin friction along with corresponding boundary layer profile quantities inferred from measured pitot-static pressure probes. An explanation of the method used to infer the profile data is given in Ref. B1-1.

Table B1-1: Tunnel Conditions

M_∞=5	ReU_∞=37x10^6/m	$H_{0,\infty}$=0.41 MJ/kg
P_T=2.12 MPa	T_0=410^{0}K	T_w=300^{0}K
U_∞=830 m/s	ρ_∞ =0.20674 kg/m^3	T_∞=68.79^{0}K

Table B1-2: Shock Generator Geometry

Gen. Angle°	X_{gen} LE, mm	Y_{gen} LE, mm	X_{gen} TE, mm	Y_{gen} TE, mm
6	18	94.5	316.4	63.1
10	23	115	318.4	62.9
14	36	135.5	327.1	62.9

Table B1-3: Shock Impingement and Separation Bubble Properties

Gen. Angle °	X_{shock} , mm	P2/P1	X_{sep} , mm	$X_{reattach}$, mm
6	349.9	3.78	-	-
10	349.8	7.64	334	345
14	350.5	13.65	314	347

Table B1-4: Wall Pressure Distributions, β=0⁰, z=25mm(span)

X, mm	Pw, Pa		X, mm	Pw, Pa		X, mm	Pw, Pa
241.0	4132		320.2	4079		365.8	4178
248.5	4065		324.0	4105		369.6	4198
256.0	4089		327.8	4121		373.4	4154
263.5	4057		331.6	4139		377.2	4141
271.0	4079		335.4	4164		388.6	4175
278.5	4114		338.0	4292		400.0	4129
286.0	4077		339.2	4209		412.5	4118
293.5	4027		343.0	4180		425.0	4158
301.0	4115		346.8	4173		437.5	4075
305.0	4102		350.6	4200		450.0	3892
308.8	4065		354.4	4261		462.5	3863
312.6	4133		358.2	4212		481.3	4028
316.4	4081		362.0	4223			

Table B1-5: Wall Pressure Distributions, β=6⁰, z=25mm(span)

X, mm	Pw, Pa		X, mm	Pw, Pa		X, mm	Pw, Pa
241.0	4330		335.4	8571		396.2	16851
248.5	4341		338.0	11951		400.0	16894
256.0	4311		339.2	12432		406.3	16902
263.5	4345		343.0	13800		412.5	16810
271.0	4359		346.8	14966		418.8	16950
278.5	4388		350.6	15683		425.0	16905
286.0	4321		354.4	16020		431.3	17212
293.5	4380		358.2	16264		437.5	16670
301.0	4326		362.0	16483		443.8	16630
305.0	4316		365.8	16588		450.0	16709
308.8	4337		369.6	16672		456.3	16642
312.6	4336		373.4	16726		462.5	16680
316.4	4363		377.2	16754		468.8	16563
320.2	4348		381.0	16806		475.0	16455
324.0	4387		384.8	16802		481.3	16442
327.8	4426		388.6	16786		487.5	15953
331.6	4479		392.4	16806		493.8	16408

Table B1-6: Wall Pressure Distributions, β=10⁰, z=25mm(span)

X, mm	Pw, Pa		X, mm	Pw, Pa		X, mm	Pw, Pa
241.0	4280		331.6	4760		392.4	33211
248.5	4278		335.4	9713		396.2	33281
256.0	4311		339.2	13843		400.0	33245
263.5	4276		343.0	18093		406.3	32956
271.0	4327		346.8	22300		412.5	33252
278.5	4312		350.6	26132		418.8	33242
286.0	4339		354.4	28100		425.0	33207
293.5	4345		358.2	29925		431.3	33365
301.0	4336		362.0	31433		437.5	33220
305.0	4290		365.8	32120		443.8	33204
308.8	4349		369.6	32500		450.0	33329
312.6	4329		373.4	33090		456.3	33223
316.4	4350		377.2	33081		462.5	32564
320.2	4340		381.0	33357		468.8	30500
324.0	4340		384.8	33389		475.0	28262
327.8	4440		388.6	33407		481.3	25836

Table B1-7: Wall Pressure Distributions, β=14⁰, z=25mm(span)

X, mm	Pw, Pa		X, mm	Pw, Pa		X, mm	Pw, Pa
241.0	4300		335.4	15782		396.2	57977
248.5	4340		338.0	17200		400.0	57924
256.0	4327		339.2	18172		406.3	58574
263.5	4329		343.0	22132		412.5	58595
271.0	4323		346.8	26806		418.8	58384
278.5	4307		350.6	32720		425.0	58277
286.0	4346		354.4	38493		431.3	58010
293.5	4298		358.2	44129		437.5	58103
301.0	4322		362.0	48773		443.8	55418
305.0	4294		365.8	51500		450.0	51373
308.8	4325		369.6	54830		456.3	46164
312.6	4862		373.4	56507		462.5	41614
316.4	8733		377.2	57160		468.8	37379
320.2	12451		381.0	57690		475.0	33991
324.0	13811		384.8	58187		481.3	30957
327.8	14752		388.6	58144		487.5	28661
331.6	15327		392.4	58012		493.8	26605

Table B1-8: Wall Heating Distributions, β=6⁰, z=25mm(span)

	Run 41				Run 42				Run 43	
X, mm	Q, W/m²	Twall, K		X, mm	Q, W/m²	Twall, K		X, mm	Q, W/m²	Twall, K
203.8	9601	297.7		161.5	9621	298.0		147	9584	298.2
223.8	9402	297.9		181.5	9354	298.2		167	9241	298.4
243.8	8971	299.1		201.5	8770	299.3		187	8715	299.5
263.8	8665	297.7		221.5	8837	297.9		207	8653	298.1
283.8	9489	297.7		241.5	9370	297.9		227	9365	298.1
303.8	9153	297.7		261.5	9001	297.8		247	8920	298.1
323.8	8599	297.5		281.5	8527	297.7		267	8576	297.9
343.8	20185	299.7		301.5	7857	297.6		287	7916	297.8
363.8	21696	300.1		321.5	7898	297.6		307	7963	297.8
383.8	23928	300.6		341.5	18480	299.9		327	8004	297.8
388.8	24216	300.6		346.5	21100	300.1		332	8113	297.8
393.8	24429	300.5		351.5	21132	299.9		337	10071	297.9
398.8	24415	300.4		356.5	21956	300.1		342	20716	300.3
403.8	24455	300.4		361.5	22482	300.2		347	21085	300.1
408.8	23704	300.3		366.5	22164	300.2		352	20274	300.0
413.8	24379	300.7		371.5	23202	300.6		357	21352	300.4
418.8	23872	301.9		376.5	23101	301.9		362	21469	301.8
423.8	22744	300.2		381.5	22530	300.3		367	21089	300.3
428.8	23178	300.3		386.5	23185	300.5		372	21890	300.5
433.8	23566	300.4		391.5	23793	300.6		377	22619	300.6
438.8	23126	300.3		396.5	23853	300.6		382	22710	300.6
443.8	23346	300.5		401.5	24034	300.8		387	23295	300.8
448.8	22882	300.3		406.5	23707	300.7		392	23142	300.8
453.8	22337	300.2		411.5	23224	300.6		397	22982	300.8
458.8	22390	300.1		416.5	23550	300.5		402	23282	300.6
463.8	23082	300.1		421.5	23883	300.6		407	23676	300.7
468.8	23054	300.3		426.5	24009	300.7		412	23777	300.9
473.8	23484	300.1		431.5	24516	300.6		417	24454	300.7

Table B1-9: Wall Heating Distributions, β=10⁰, z=25mm(span)

	Run 39				Run 40	
X, mm	Q, W/m²	Twall, K		X, mm	Q, W/m²	Twall, K
144.7	9606	297.0		212	10047	297.5
164.7	9524	297.3		232	10186	297.7
184.7	8964	298.4		252	9140	298.9
204.7	8994	297.0		272	9102	297.5
224.7	9269	296.9		292	9585	297.5
244.7	9150	297.0		312	9404	297.5
264.7	8585	296.8		332	10673	297.6
284.7	8011	296.7		352	32120	301.9
304.7	8050	296.9		372	38331	303.4
324.7	8526	296.9		392	41439	304.1
329.7	13189	298.1		397	41870	304.1
334.7	17872	298.4		402	42631	304.1
339.7	19528	298.7		407	44983	304.4
344.7	26454	300.3		412	46083	304.5
349.7	30287	301.1		417	44944	304.1
354.7	34720	302.3		422	41743	304.1
359.7	37121	304.3		427	40587	305.3
364.7	38522	303.0		432	39139	303.4
369.7	40234	303.4		437	39783	303.6
374.7	41396	303.7		442	40366	303.6
379.7	41460	303.7		447	39835	303.5
384.7	42123	303.9		452	40092	303.6
389.7	41729	303.8		457	38948	303.4
394.7	41180	303.8		462	37343	303.2
399.7	41805	303.7		467	36080	302.7
404.7	42167	303.8		472	35036	302.4
409.7	42554	303.9		477	33631	302.2
414.7	43138	303.8		482	32621	301.7

Table B1-10: Wall Heating Distributions, β=14⁰, z=25mm(span)

	Run 35				Run 36	
X, mm	Q, W/m²	Twall, K		X, mm	Q, W/m²	Twall, K
194.9	10764	295.6		202.9	10533	296.6
214.9	10506	295.8		222.9	10115	296.8
234.9	9849	297.0		242.9	9209	297.9
254.9	9413	295.6		262.9	9009	296.6
274.9	10023	295.6		282.9	9978	296.6
294.9	9675	295.7		302.9	9807	296.7
314.9	18262	297.2		322.9	18155	298.2
334.9	18201	297.1		342.9	28814	300.4
354.9	55526	303.8		362.9	65230	308.9
374.9	73449	307.2		382.9	70551	310.4
379.9	73186	307.1		387.9	69942	310.1
384.9	75086	307.1		392.9	72401	310.2
389.9	77561	307.4		397.9	75761	310.9
394.9	78730	307.3		402.9	76310	310.9
399.9	73541	306.2		407.9	74395	309.8
404.9	68314	306.3		412.9	68078	309.4
409.9	66395	307.2		417.9	64066	310.1
414.9	64828	305.3		422.9	62295	308.1
419.9	65619	305.6		427.9	63159	308.4
424.9	65821	305.6		432.9	63348	308.4
429.9	64970	305.4		437.9	62042	308.1
434.9	65235	305.5		442.9	60783	307.8
439.9	62455	305.0		447.9	56685	306.9
444.9	58009	304.2		452.9	52465	305.9
449.9	55355	303.4		457.9	49803	305.1
454.9	52948	303.0		462.9	47681	304.5
459.9	50259	302.5		467.9	45282	304.0
464.9	48151	301.9		472.9	43633	303.4

Table B1-10-Continued: Wall Heating Distributions, β=14⁰, z=25mm(span)

	Run 37				Run 38	
X, mm	Q, W/m²	Twall, K		X, mm	Q, W/m²	Twall, K
149.9	10096	296.9		157.4	10536	296.5
169.9	9859	297.2		177.4	10389	296.8
189.9	9026	298.2		197.4	9541	297.9
209.9	8710	296.8		217.4	9292	296.4
229.9	9126	296.8		237.4	9865	296.4
249.9	9855	297.0		257.4	9540	296.5
269.9	8956	296.7		277.4	9271	296.3
289.9	8270	296.7		297.4	8533	296.2
309.9	17840	298.7		317.4	17316	298.0
329.9	16010	298.4		337.4	22340	299.0
334.9	18505	298.9		342.4	31066	300.7
339.9	25440	300.0		347.4	44354	303.2
344.9	38213	302.5		352.4	59055	306.5
349.9	50293	305.3		357.4	68075	308.7
354.9	58221	307.2		362.4	71345	309.4
359.9	65430	309.6		367.4	74145	310.9
364.9	68742	311.7		372.4	74311	312.4
369.9	69482	310.3		377.4	73016	310.6
374.9	70277	310.7		382.4	72818	310.7
379.9	69986	310.5		387.4	72207	310.6
384.9	67999	310.1		392.4	70514	310.2
389.9	67365	310.0		397.4	70510	310.2
394.9	65751	309.6		402.4	69307	309.9
399.9	63910	309.3		407.4	67513	309.6
404.9	64226	309.1		412.4	67650	309.3
409.9	65229	309.2		417.4	68301	309.4
414.9	65560	309.3		422.4	68886	309.6
419.9	66862	309.2		427.4	70037	309.6

Table B1-11: Wall Shear Stress Distributions, β=0⁰, Optical Measurements

X, mm	τ_w, *Pa*		*X, mm*	τ_w, *Pa*		*X, mm*	τ_w, *Pa*		*X, mm*	τ_w, *Pa*
59.0	74.8		87.0	149.0		205.0	103.8		298.0	86.6
61.0	109.5		88.0	142.3		206.0	102.7		299.0	91.5
62.0	94.7		92.0	156.8		215.0	98.2		300.0	93.0
64.0	74.7		100.0	151.9		215.0	106.3		305.0	86.5
65.0	91.3		101.0	153.8		216.0	99.2		306.0	88.1
66.0	100.0		102.0	154.3		217.0	96.9		307.0	89.0
67.0	106.4		122.0	157.2		226.0	104.0		308.0	89.6
68.0	90.0		123.0	154.4		227.0	98.0		311.0	91.2
69.0	91.5		124.0	152.9		228.0	98.2		312.0	84.2
75.0	116.6		125.0	152.1		229.0	100.3		312.0	83.7
76.0	129.1		138.0	128.8		232.0	105.1		313.0	87.9
78.0	142.6		139.0	133.1		233.0	105.5		314.0	89.3
79.0	131.3		140.0	134.4		234.0	105.6		315.0	90.0
80.0	132.5		141.0	135.1		243.0	101.8		322.0	85.9
81.0	138.6		142.0	135.5		244.0	102.9		323.0	93.7
74.0	104.4		145.0	128.9		258.0	100.8		324.0	95.9
75.0	88.0		146.0	123.5		259.0	95.7		325.0	96.8
76.0	96.5		147.0	122.8		260.0	102.6		339.0	86.3
79.0	134.4		173.0	117.9		267.0	97.5		340.0	89.8
80.0	136.5		174.0	119.7		268.0	101.1		341.0	91.0
82.0	142.1		185.0	127.9		272.0	91.4		343.0	91.5
85.0	139.3		186.0	124.3		273.0	91.8		344.0	92.5
86.0	144.1		187.0	122.2		274.0	91.9		345.0	92.9
87.0	139.5		188.0	120.7		275.0	92.0		356.0	92.3
88.0	132.8		189.0	119.7		276.0	92.0		357.0	88.5
90.0	146.5		183.0	110.6		277.0	92.0		362.0	92.4
91.0	139.0		184.0	108.2		276.0	99.8		363.0	93.3
92.0	137.4		198.0	100.6		277.0	96.9		364.0	93.6
93.0	135.3		199.0	103.0		278.0	95.4		365.0	93.7
94.0	139.6		200.0	103.8		276.0	95.8		383.0	87.5
95.0	165.5		198.0	104.2		277.0	94.1		380.0	93.2
96.0	162.4		199.0	102.6		278.0	91.9		381.0	83.0
97.0	153.8		200.0	102.0		289.0	90.2		382.0	88.1
73.0	111.5		201.0	101.7		290.0	89.2		382.0	96.5
74.0	113.5		202.0	101.6		284.0	87.7		383.0	93.1
75.0	118.3		203.0	109.1		285.0	88.4		384.0	92.5
76.0	124.1		204.0	105.6		286.0	88.2			

Table B1-12: Wall Shear Stress Distributions, β=10⁰, Optical Measurements

X, mm	τ_w, *Pa*		*X, mm*	τ_w, *Pa*		*X, mm*	τ_w, *Pa*		*X, mm*	τ_w, *Pa*
274.00	91.9		324.37	79.3		346.00	0.0		390.00	440.5
278.00	91.9		326.05	75.9		348.47	34.8		396.45	459.7
286.00	88.2		329.47	60.5		354.89	191.7		405.88	451.1
293.00	89.2		330.62	43.4		358.60	259.3		419.43	412.2
300.00	89.5		330.72	40.2		360.06	284.8		426.59	397.6
305.33	92.8		334.00	0.0		369.87	382.6		433.68	405.4
308.00	89.6		338.35	-26.5		371.92	385.7		443.42	393.1
311.00	91.2		341.82	-32.8		378.81	392.7		454.48	404.5
315.00	90.0		342.42	-34.3		383.70	389.4			
320.22	85.6		343.12	-42.1		384.33	419.9			

Table B1-13: Wall Shear Stress Distributions, β=14⁰, Optical Measurements

X, mm	τ_w, *Pa*		*X, mm*	τ_w, *Pa*		*X, mm*	τ_w, *Pa*		*X, mm*	τ_w, *Pa*
274.00	91.9		305.10	84.3		311.83	17.9		391.72	630.9
278.00	91.9		296.94	92.8		314.00	0.0		408.33	645.1
286.00	88.2		306.48	73.2		336.94	-52.5		420.67	725.9
293.00	89.2		308.27	59.8		343.29	-57.9		429.65	715.2
300.00	89.5		324.86	-14.8		346.68	-27.3		455.38	564.0
236.11	95.5		331.14	-16.1		348.00	0.0		461.42	551.3
214.55	98.4		320.78	-14.0		345.48	-39.2		469.30	542.2
227.82	96.7		327.70	-15.1		369.14	425.4		359.28	205.9
228.44	97.2		332.24	-28.4		355.75	144.4		362.17	263.7
290.54	94.9		307.66	65.1		376.46	578.6			
294.73	95.2		310.10	32.8		381.50	685.9			

Table B1-14: Wall Shear Stress Coefficient Distributions, Cf Probe Measurements

Shock Gen Angle	*X, mm*	*Cf x 1000*
0°	266	1.44015
0°	296	1.34573
0°	316	1.32383
0°	336	1.31128
0°	356	1.29358
10°	266	1.44015
10°	296	1.34573
10°	316	1.32383
10°	376	5.16175
10°	396	6.08474
10°	426	5.33983
10°	449	5.38522
14°	266	1.44015
14°	296	1.34573
14°	376	6.20706
14°	396	7.56285
14°	426	7.43288

Table B1-15: Upstream Boundary Layer Profile , X=266 mm. β=0
x= 266mm, z=25 (span), Re=38454880/m,
P_0=2136066 Pa, T_0=408.2^{0}K, T_w/T_r=.809

Y, mm	*U, m/s*	*Mach*	*T, K*	*ρ, kg/m³*	*Y +*	*U +*
0.00015	500.15	1.636	232.5	0.0640	18.05	11.53
0.00025	589.69	2.095	197.1	0.0755	30.09	13.90
0.00035	612.61	2.239	186.2	0.0799	42.13	14.54
0.00045	640.42	2.427	173.3	0.0859	54.16	15.35
0.00055	657.84	2.557	164.7	0.0903	66.20	15.87
0.00065	665.55	2.616	161.0	0.0924	78.23	16.10
0.00075	680.17	2.735	153.9	0.0967	90.27	16.55
0.00085	689.79	2.824	148.5	0.1002	102.30	16.86
0.00105	700.94	2.924	143.0	0.1041	126.38	17.21
0.00125	722.79	3.153	130.8	0.1138	150.45	17.94
0.00145	734.65	3.287	124.3	0.1198	174.52	18.35
0.00165	753.26	3.526	113.5	0.1311	198.59	19.01
0.00195	767.15	3.728	105.3	0.1413	234.70	19.53
0.00215	771.16	3.792	102.9	0.1446	258.77	19.68
0.00265	794.77	4.213	88.5	0.1681	318.95	20.61
0.00315	809.63	4.542	79.0	0.1883	379.13	21.24
0.00365	819.70	4.792	72.8	0.2044	439.31	21.69
0.00415	823.53	4.897	70.4	0.2115	499.49	21.87
0.00465	825.76	4.961	68.9	0.2159	559.67	21.97

Baseline Computations. Results from simulations for the Schülein fully separated case (14° shock generator) follow that provide a baseline for those wanting to compute the experiments documented above. The baseline is intended to facilitate and gage new code development and turbulence model improvements.

These solutions were previously obtained using the DPLR real-gas Navier-Stokes code and published by NASA during their task of uncertainty assessment of hypersonic simulations of SWBLI. See Ref. B1-6 and B1-7. Only the flat-plate solution and fully separated solutions are described herein, however additional information for the other cases along with grids and input decks are included in the DVD accompanying this TM. Due to the low total temperature, and the absence of dissociation for this case, air as a perfect-gas was assumed for the working fluid. The input conditions were as given in Table B1-1, with Mach number, freestream density and temperature and wall temperature specified. A viscous isothermal wall boundary condition was specified for both the test plate and the shock generator. Solutions for the several turbulence models were obtained, including Baldwin-Lomax, Menter SST, Wilcox K-Omega 2006, and the Spalart-Allmaras models. Transition was specified so as to agree with the 0.06-0.1 m range as observed from the experimental data. Laminar simulations of the flat plate result in $Re\theta \sim 500$ at the transition location.

The boundary layer development upstream of the interactions is obtained from flat-plate experimental runs and DPLR solutions. For these solutions, a simple H-grid of 3 blocks was used, with a total of 528x3x128 cells, and spacing of the 1st grid point from the wall of $y^+_1 \sim 0.05$ and ReCell~0.25. Fig. B1-1 and B1-2 compares the wall shear stress and wall heating, respectively, as obtained from the flat-plate DPLR computations using the several turbulence models with the experimental measurements. The measurements shown in Figs. B1-1 and B1-2 are from upstream regions of the impinging shock cases, truncated to end prior to the interaction, as no separate runs for the flat plate alone were reported. Also shown in Fig. B1-1 is the wall shear stress as obtained from the VanDriest II transformed correlation of White. The source documents, Refs B1-1 and B1-7, should be referred to for further details. The figures were created using the Tecplot graphics package, with its input layout and data files provided in the DVD.

For the Schülein 14° fully separated solutions, a grid of 3 blocks was used, with 256 cells between the flat plate and shock generator, and a total of 1056x3x256 cells. Figure B1-3, -4, and -5 present the wall pressure, wall heat transfer and wall shear stress distributions as obtained from DPLR solutions with the corresponding experimental measurements for the Schülein 14° fully separated case. The grid file, DPLR input deck for this case, as well as for the Schülein 6° attached and 10° incipient separation cases, may be found on the accompanying DVD. As suggested in Ref. B1-7 for all of the impinging SWTBLI cases, important areas of comparison

between experiment and computation to be observed in these figures are pressure and heat transfer levels for the separation bubble and post-reattachment plateau regions, as well as the extent and location of separation. Data files for additional Schülein cases are also included in the DVD.

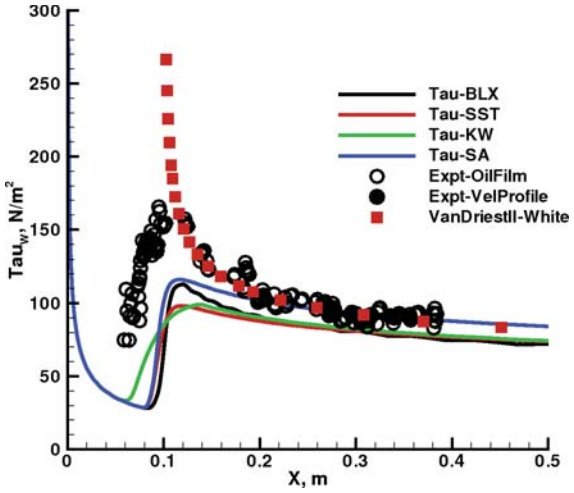

Figure B1-1. Schülein Flat-Plate Wall Shear Stress.

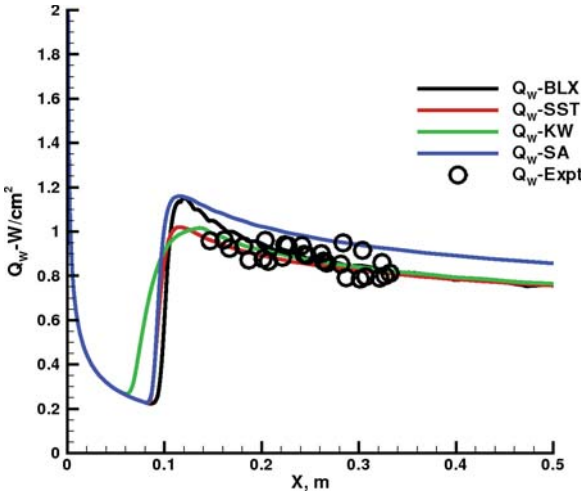

Figure B1-2. Schülein Flat-Plate Wall Heating.

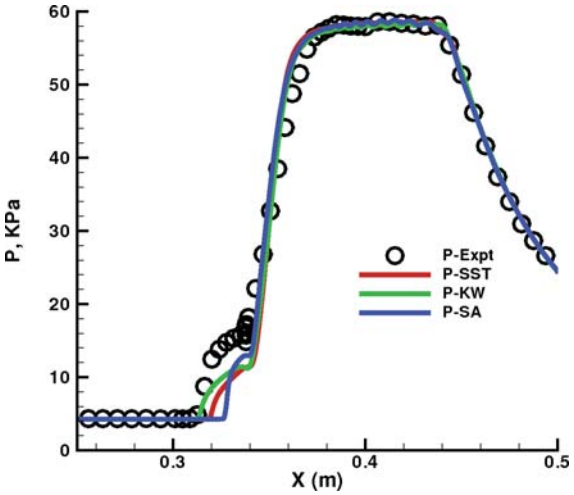

Figure B1-3. Schülein 14° Wall Pressure.

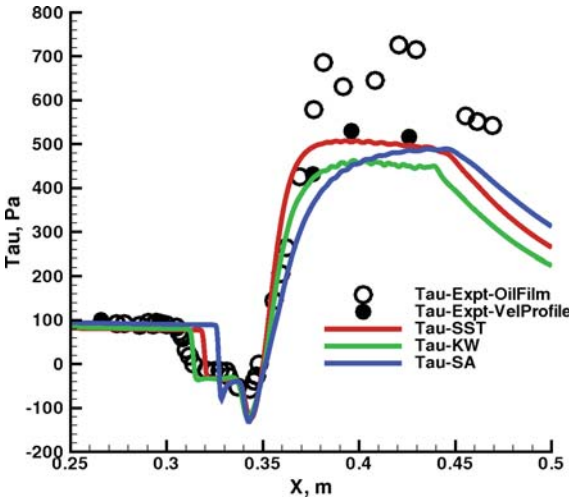

Figure B1-4. Schülein 14° Wall Shear Stress.

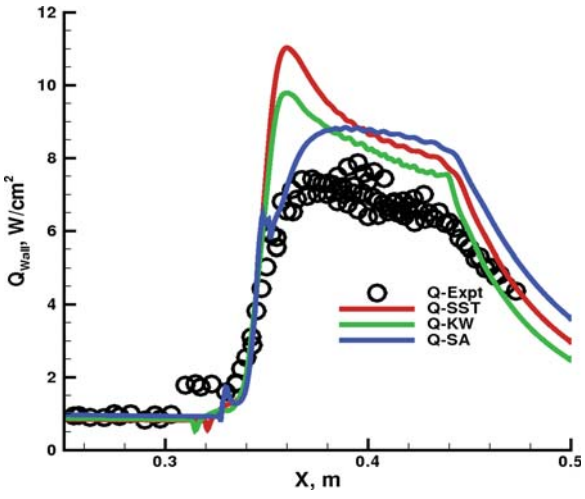

Figure B1-5. Schülein 14° Wall Heating.

B2. Murray – Axisymmetric Impinging Shock

Ref. B2-1. Murray, N., "Three-Dimensional Turbulent Shock-Wave/Boundary-Layer Interactions in Hypersonic Flows," PhD. Dissertation, Imperial College, University of London, 2007.

Ref. B2-2. Murray, N. and Hillier, R., "Separated Shock Wave/Turbulent Boundary Layer Interactions at Hypersonic Speeds," AIAA Paper 2006-3038, June 2006.

Ref. B2-3. Mallinson, S.G., Hillier, R., Jackson, A.P., Kirk, D.C., Soltani, S. and Zanchetta, M., "Gun tunnel flow calibration: defining input condition for hypersonic flow computations," Shock Waves, Vol. 10, pp. 313-322, 2000.

Ref. B2-4. Murray, N., Hillier, R. and Williams, S., "Experimental Investigation of Axisymmetric Hypersonic Shock-Wave/Turbulent Boundary-Layer Interactions," Journal of Fluid Mechanics, Vol. 714, Jan. 2, 2013, pp. 152-189.

Ref. B2-5. Brown, J.L., "Shock Wave Impingement on Boundary Layers at Hypersonic Speeds: Computational Analysis and Uncertainty", AIAA Paper 2011-3143, 42nd AIAA Thermophysics Conference, Honolulu, Hawaii, June 27-30, 2011.

General description. The experiment was conducted in the Imperial College Gun Tunnel at a nominal Mach number of 8.9 and free stream Reynolds number of 48 x 10^6 per meter, see Table B2-1. For this facility, Nitrogen (N_2) is the working fluid. The test surface was a hollow axisymmetric cylinder. The test cylinder axis was aligned lengthwise in the free stream direction, positioned in the center of the test section. An advantage of the axisymmetric configuration is in the elimination of potential spanwise effects. The leading edge protruded slightly into the nozzle exit. An axisymmetric cowl, whose internal surface was beveled at an angle so as to develop a concentric shock wave that impinged on the cylinder surface, was positioned around the cylinder at a sufficient distance downstream from the cylinder leading edge to insure naturally developed turbulent flow ahead of the interaction. Two cowls were used: Cowl-1, which did not cause the flow to separate; and Cowl-2, which caused the flow to separate. Measurements of cylinder surface pressure and heat transfer along with schlieren and some surface oil flow photos were taken. Test duration was sufficient to establish steady flow in the interaction regions. Database users are encouraged to consult Refs. B2-1 through B2-4 for a complete discussion of these data.

Experimental arrangement. The arrangement is shown in the figure below taken with permission from Ref. B2-1. The center body is a hollow cylinder 75mm in diameter. It is made up of a combination of sections to provide the desired length with typical total chord length of 800 mm. An instrumented section of the center body allows pressure or heat transfer modules to be inserted in the interaction zone. It has a sharp leading edge, with the chamfer directed internally. Two cowl

designs were used. Cowl-1 was chamfered internally at 4.7^0. This leads to a condition of attached flow in the interaction region. The second, Cowl-2, was chamfered internally at 10^0. This leads to a condition of separated flow. Cowl-1 length was 137mm. Cowl-2 length was 85 mm. Cowl-1 external radius was 77mm and Cowl-2 external radius was 80mm. Internal geometric details for both cowls are given in Table B2-2. Clearance between the cylinder and cowl was sufficient to allow the flow between to be swallowed. The impinging shock originates at the beveled leading edge of the cowl, whereas an expansion wave originates at the cowl external trailing edge that intersected the flow downstream of the interaction region. The cowl leading edge was located approximately 675 mm from the cylinder leading edge where naturally occurring, fully developed turbulent flow was present.

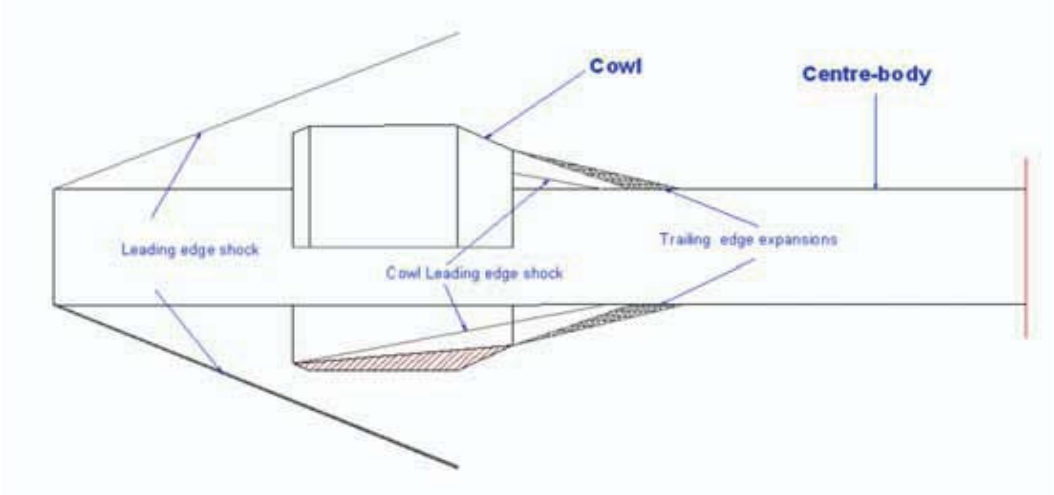

Facility. Tests were performed in the Imperial College Gun Tunnel. The tunnel is comprised of three components: a driver section, a piston driven section and an axisymmetric nozzle and dump-tank section. Burst disks that sequentially initiate the flow separate the sections. The nozzle, whose exit diameter is 350 mm, expands the flow to a nominal Mach number of 8.9 test rhombus extending 1.5 m into the tank. The tests were conducted at the highest of three possible pressure conditions to insure a high Reynolds number turbulent flow over the cylindrical centerbody. The resulting conditions in the test rhombus were: $ReU_\infty = 48 \times 10^6$/m, $T_{(0,\infty)} = 1150^\circ K$, and $P_{(0,\infty)} = 60.8\ MPa$. Nominal wall temperature was $T_{wall}=293^\circ K$. The total run-time was approximately 20 milliseconds, which includes a ramp-up to steady test conditions, steady conditions of 5 milliseconds and a ramp-down. The high-pressure condition leads to a favorable streamwise pressure gradient, $dp/dx<0$, in the test rhombus, and which is also measured on the test cylinder. (See Ref. B2-3 on the facility calibration.)

Measurements. Pressure measurements along the cylinder at three azimuthal angles were taken using Kulite QC series sensors mounted in modules inserted into a centerbody section. Care was taken to minimize the sensor response time. Cells were calibrated in situ by adjusting dump tank pressure. Heat transfer measurements were taken using “in-house designed” thin film resistance

temperature gauges mounted in modules that were inserted into a centerbody section. Manufacture and module mounting procedures are detailed in Ref. B2-1. The heat-transfer gauges were calibrated by wrapping the modules in protective latex, immersing them in water heated over an appropriate temperature range and then determining the corresponding output voltage. Estimates for the worst case scenario total errors in the pressure and heat-transfer measurements were reported as +/−2.3% and +8.7% to −2.2% respectively. Schlieren images of the flow field were recorded with a digital camera during all tests runs and used to visualize shock interaction structure. Oil flow photos were taken during the tests with separated flow to illustrate the formation of Goetler vortices. See Ref. B2-1.

Data tables. Below are data-tables, provided with permission of Dr. Richard Hillier of Imperial College and Neil Murray of ESTSC, that give wall pressures and heat transfer on the test cylinder surface for the three cases of a) Cylinder only, no cowl, b) attached SWTBLI interaction of Cowl-1, and c) separated SWTBLI of Cowl-2. The data tabulated herein was obtained from Prof. Hillier and represent the data symbols presented in figures from Refs. B2-1 and B2-3. The nominal tunnel conditions are given in Table B2-1. As pointed out in Ref. B2-1, a mild pressure gradient is present in the tunnel test section that needs to be accounted for in numerical simulations of these data. One method for accomplishing this is discussed later when baseline simulations are presented.

Note that in the tables, X is distance from cylinder leading edge, while X_{TE} is distance from Cowl trailing edge, $X_{TE}=(X-X_{gen,TE})$. R is radius from cylinder axis, thereby the distance in the flow measured normal to the cylinder is $Y=R-R_{cyl}$, where R_{cyl} =37.5mm.

Table B2-1: Nominal Tunnel Conditions

M_∞=8.9	ReU_∞=48 x10^6/m	$H_{0,\infty}$=1.19 MJ/kg
P_T=60.8 MPa	T_0=1150^{0}K	T_w=293^{0}K
U_∞=1499 m/s	ρ_∞ =0.1510 kg/m^3	T_∞=68.3^{0}K

Table B2-2: Shock Generator Geometry, R_{cyl}=37.5 mm.

Gen. Angle°	X_{gen} LE, mm	R_{gen} LE, mm	X_{gen} TE, mm	R_{gen} TE, mm
4.7	675	75.00	812.	63.74
10	675	75.00	760.	60.00

Table B2-3: Pressures Distribution Along Cylinder-Mallinson, No Cowl.

X, mm	Pw, KPa		X, mm	Pw, KPa		X, mm	Pw, KPa		X, mm	Pw, KPa
72.0	3.41		193.5	3.24		262.0	3.37		350.5	3.35
75.0	3.36		195.0	3.36		263.5	3.34		351.0	3.34
82.0	3.40		200.0	3.35		265.0	3.35		352.0	3.44
85.0	3.36		202.0	3.41		265.5	3.45		352.0	3.26
92.0	3.42		204.0	3.44		268.5	3.33		354.0	3.38
95.0	3.35		205.0	3.40		269.0	3.38		354.5	3.26
98.5	3.40		207.0	3.48		272.0	3.37		355.5	3.35
102.0	3.46		207.0	3.45		272.0	3.43		357.0	3.24
105.0	3.28		208.5	3.32		273.5	3.22		358.0	3.36
108.5	3.32		212.0	3.36		275.5	3.40		360.5	3.24
112.0	3.42		213.5	3.40		280.0	3.45		361.0	3.27
112.0	3.38		214.0	3.49		284.0	3.44		364.0	3.27
115.0	3.41		215.0	3.35		285.5	3.40		364.0	3.36
122.0	3.37		217.0	3.47		287.0	3.24		364.5	3.18
125.0	3.38		217.0	3.41		287.0	3.46		365.5	3.36
127.0	3.42		218.5	3.26		292.0	3.40		367.0	3.20
128.5	3.36		220.0	3.26		293.5	3.30		367.0	3.26
132.0	3.36		220.0	3.47		294.0	3.42		368.0	3.25
133.5	3.38		220.5	3.39		297.0	3.30		371.0	3.25
135.0	3.30		222.0	3.38		297.0	3.46		372.0	3.40
137.0	3.39		223.5	3.42		300.0	3.45		374.0	3.26
138.5	3.33		224.0	3.43		300.0	3.37		374.5	3.27
140.0	3.35		225.0	3.31		300.5	3.36		377.0	3.23
142.0	3.37		227.0	3.49		303.5	3.31		378.0	3.34
143.5	3.38		228.5	3.22		304.0	3.33		378.0	3.24
145.0	3.30		230.5	3.41		307.0	3.40		379.0	3.35
148.5	3.42		232.0	3.33		310.5	3.31		380.0	3.26
152.0	3.40		232.0	3.36		313.5	3.34		380.5	3.24
152.0	3.45		233.5	3.37		314.0	3.33		381.0	3.24
155.0	3.42		234.0	3.47		317.0	3.38		381.0	3.25
160.0	3.47		235.0	3.35		320.0	3.40		384.0	3.20
162.0	3.47		237.0	3.47		320.5	3.31		385.5	3.31
165.0	3.47		240.0	3.42		324.0	3.39		387.0	3.16
167.0	3.45		240.5	3.44		324.0	3.32		388.0	3.24
168.5	3.39		242.0	3.40		327.0	3.36		389.0	3.34
172.0	3.44		244.0	3.49		334.0	3.39		390.5	3.22
173.5	3.36		245.0	3.40		337.0	3.40		391.0	3.25
175.0	3.43		247.0	3.38		338.0	3.38		392.0	3.31
177.0	3.43		248.5	3.30		339.0	3.36		393.0	3.22
178.5	3.43		252.0	3.42		340.0	3.20		394.0	3.24
180.0	3.38		253.5	3.36		340.5	3.31		394.5	3.22
182.0	3.50		255.0	3.40		341.0	3.35		395.5	3.29
183.5	3.34		257.0	3.35		344.0	3.34		397.0	3.24
185.0	3.42		258.5	3.22		345.5	3.40		398.0	3.19
188.5	3.40		259.0	3.48		347.0	3.32		399.5	3.19
192.0	3.47		260.0	3.29		348.0	3.38		400.5	3.21
192.0	3.42		260.0	3.42		349.0	3.41		401.0	3.14

Table B2-3 Continued: Pressures Distribution Along Cylinder-Mallinson, No Cowl.

X, mm	Pw, KPa		X, mm	Pw, KPa		X, mm	Pw, KPa		X, mm	Pw, KPa
403.0	3.31		471.0	3.27		498.5	3.04		565.0	3.01
404.0	3.16		472.0	3.08		499.5	3.05		566.0	3.14
404.5	3.14		472.0	3.19		501.0	3.17		567.0	3.04
405.5	3.24		473.0	3.14		502.0	3.07		568.5	3.07
406.0	3.30		474.5	3.24		505.0	3.08		572.0	3.00
407.0	3.21		475.0	3.07		506.0	3.28		573.5	3.07
408.0	3.23		478.0	3.25		508.5	3.03		574.5	2.97
409.5	3.18		479.5	3.21		512.0	3.06		574.5	3.01
411.0	3.23		481.0	3.19		512.0	3.05		575.0	3.04
412.0	3.27		482.0	3.07		512.0	3.14		577.0	3.07
414.5	3.22		483.0	3.12		513.0	3.26		578.0	3.05
418.0	3.15		484.5	3.15		515.0	3.08		578.0	3.05
418.0	3.22		485.0	3.06		515.0	3.11		578.5	2.99
419.0	3.16		486.0	3.20		519.5	3.14		580.0	3.01
419.5	3.18		486.0	3.12		522.0	3.06		582.0	3.05
421.0	3.23		488.0	3.28		523.0	3.20		583.5	3.07
421.0	3.19		488.5	3.13		525.0	3.07		585.0	2.99
425.5	3.20		489.5	3.20		526.0	3.03		588.0	2.95
426.0	3.31		491.0	3.15		526.0	3.14		588.0	3.07
428.0	3.18		492.0	3.06		527.0	3.07		588.5	2.99
429.0	3.13		494.5	3.14		528.5	3.09		592.0	3.05
431.0	3.18		495.0	3.10		529.5	3.22		592.0	2.98
432.0	3.14		496.0	3.11		532.0	3.04		593.5	2.95
432.0	3.31		496.0	3.06		533.5	3.11		594.5	3.01
433.0	3.16		496.0	3.04		535.0	3.09		595.0	3.04
434.5	3.24		496.0	3.11		537.0	3.05		595.0	3.02
435.5	3.18		496.0	3.12		538.0	3.10		598.0	2.98
438.0	3.26		496.0	3.16		538.5	3.02		598.0	2.99
439.5	3.19		496.0	3.06		539.5	3.18		599.5	2.97
441.0	3.24		496.0	3.15		540.0	3.02		599.5	2.97
443.0	3.12		496.0	3.15		542.0	3.06		600.0	3.01
444.5	3.15		496.0	3.07		543.5	3.11		602.0	2.99
445.5	3.11		496.0	3.10		545.0	3.07		604.5	3.05
446.0	3.15		496.0	3.07		546.0	3.10		605.0	3.01
448.0	3.17		496.0	3.14		548.5	3.01		606.0	3.08
449.5	3.17		496.0	3.07		552.0	3.08		607.0	3.00
451.0	3.20		496.0	3.11		552.0	3.02		608.0	3.02
452.0	3.16		496.0	3.17		553.5	3.02		608.0	3.03
454.5	3.14		496.0	3.05		554.5	3.00		608.5	3.03
458.0	3.24		496.0	3.11		554.5	2.98		609.5	2.97
458.0	3.19		496.0	3.03		555.0	3.01		609.5	2.96
459.5	3.15		496.0	3.08		555.0	3.08		612.0	2.96
461.0	3.22		498.0	3.22		560.0	3.06		613.5	2.93
461.0	3.28		488.5	3.13		562.0	3.08		614.5	3.01
466.0	3.17		489.5	3.20		564.5	3.06		615.0	3.01
468.0	3.29		491.0	3.15		564.5	3.04		617.0	2.97

Table B2-3 Concluded: Pressures Distribution Along Cylinder-Mallinson, No Cowl.

X, mm	Pw, KPa		X, mm	Pw, KPa		X, mm	Pw, KPa		X, mm	Pw, KPa
618.0	3.00		645.0	2.94		680.0	2.98		723.0	2.91
618.0	3.00		647.0	2.98		681.0	2.97		726.0	2.93
618.0	3.06		648.0	3.02		683.0	2.98		728.0	2.96
618.5	2.93		648.5	2.94		684.5	3.01		729.5	2.96
619.5	3.06		649.5	3.01		686.0	2.95		731.0	2.88
619.5	3.04		651.0	2.98		686.0	2.94		731.0	2.95
620.0	2.94		651.0	2.98		687.0	2.95		738.0	2.90
620.0	2.93		652.0	2.94		688.0	2.96		739.5	2.96
621.0	3.00		653.5	2.91		689.5	2.88		740.0	2.86
621.0	2.98		654.5	2.87		691.0	2.91		741.0	2.86
622.0	2.99		655.0	2.95		693.5	2.89		741.0	2.92
623.5	2.93		657.0	2.97		694.5	2.94		746.0	2.98
625.0	2.96		658.0	2.98		697.0	2.92		753.0	2.92
628.0	3.02		658.0	2.98		698.0	2.92		763.0	2.90
628.5	2.84		658.5	2.99		698.0	3.00		766.0	2.85
631.0	3.02		659.5	2.95		699.5	2.93		766.0	2.83
631.0	3.01		660.0	2.94		700.0	2.89		766.0	2.87
632.0	2.97		660.0	2.90		700.0	2.95		766.0	2.94
632.0	2.92		661.0	2.90		701.0	2.91		780.0	2.79
633.0	3.05		661.0	2.89		701.0	2.93		786.0	2.88
633.0	2.99		661.0	2.98		701.0	3.01		786.0	2.92
633.5	2.92		662.0	2.96		703.5	2.95		806.0	2.85
634.5	2.93		663.5	2.91		706.0	2.97		846.0	2.77
635.0	2.97		665.0	2.90		706.0	2.95		846.0	2.85
635.0	2.92		668.0	2.96		708.0	2.98		817.0	2.93
638.0	3.00		668.5	2.95		711.0	2.90		827.0	2.84
639.5	3.00		671.0	3.02		711.0	3.02		837.0	2.91
640.0	2.96		672.0	2.91		713.0	2.95		807.0	2.95
641.0	2.94		673.0	3.01		713.5	2.83		817.0	2.92
642.0	2.96		673.5	2.96		718.0	2.93		827.0	2.90
643.0	2.97		674.5	2.97		719.5	2.96		837.0	2.86
640.0	2.96		675.0	2.87		720.0	2.93		827.0	2.94
643.0	2.97		678.0	2.95		721.0	2.82		837.0	2.92
644.5	2.97		679.5	2.89		721.0	2.89			

Table B2-4: Heating Distribution Along Cylinder-Mallinson, No Cowl.

X, mm	Qw, W/cm²		X, mm	Qw, W/cm²		X, mm	Qw, W/cm²		X, mm	Qw, W/cm²
20.0	5.69		112.0	4.90		144.5	9.63		183.5	10.22
20.0	5.89		112.0	5.28		144.5	9.37		183.5	10.28
25.0	5.13		115.0	5.46		145.0	9.32		183.5	9.95
25.0	5.38		115.0	5.65		147.5	9.77		183.5	10.12
30.0	4.93		115.0	5.24		147.5	9.71		189.5	10.09
30.0	4.98		115.0	5.99		147.5	9.88		189.5	10.25
35.0	4.26		118.0	5.74		147.5	9.59		192.5	10.12
35.0	4.40		118.0	5.93		148.0	10.36		192.5	10.25
40.0	4.14		118.0	6.10		150.5	10.50		195.5	10.08
40.0	4.19		121.0	5.66		150.5	10.49		195.5	10.18
45.0	4.08		121.0	6.05		150.5	10.44		198.5	9.77
45.0	4.18		124.0	6.63		150.5	10.19		198.5	9.70
50.0	3.98		124.0	7.13		151.0	10.66		201.5	9.94
50.0	4.05		124.0	7.14		151.0	9.77		201.5	9.76
55.0	3.67		127.0	6.81		153.5	10.26		204.5	9.86
55.0	3.69		127.0	7.47		153.5	10.40		204.5	10.31
60.0	3.73		127.0	7.37		153.5	10.23		207.5	10.09
60.0	3.78		129.5	7.10		153.5	9.94		207.5	9.97
65.0	3.76		129.5	7.46		154.0	10.70		220.0	9.77
65.0	3.84		129.5	7.23		154.0	10.10		220.0	9.81
70.0	3.66		129.5	7.09		154.0	9.83		220.0	9.98
70.0	3.72		130.0	7.99		156.5	10.37		223.0	9.71
88.0	3.26		130.0	8.12		156.5	10.47		223.0	9.75
88.0	3.27		132.5	7.60		156.5	10.23		223.0	9.93
91.0	3.38		132.5	7.81		156.5	10.00		226.0	9.67
91.0	3.34		132.5	7.78		157.0	10.52		226.0	9.71
94.0	3.51		132.5	7.48		159.5	9.99		226.0	9.83
94.0	3.44		133.0	8.44		159.5	10.42		229.0	9.55
97.0	3.66		135.5	8.21		160.0	10.81		229.0	9.59
97.0	3.62		135.5	8.54		160.0	10.20		229.0	9.66
100.0	3.84		135.5	8.31		163.0	10.51		232.0	9.45
100.0	3.88		135.5	8.02		163.0	10.03		232.0	9.51
100.0	3.76		136.0	8.56		165.5	10.17		232.0	9.60
100.0	3.99		138.5	8.76		165.5	10.67		235.0	9.58
103.0	4.04		138.5	9.08		166.0	10.44		235.0	9.54
103.0	4.39		138.5	8.84		166.0	10.34		235.0	9.63
103.0	3.96		138.5	8.63		168.5	10.53		238.0	9.44
103.0	4.53		139.0	9.52		168.5	10.34		238.0	9.32
106.0	4.34		139.0	8.22		169.0	10.40		238.0	9.42
106.0	4.57		141.5	9.09		171.5	9.93		241.0	9.42
106.0	4.24		141.5	9.46		171.5	10.28		241.0	9.54
106.0	4.82		141.5	9.24		172.0	10.47		241.0	9.61
109.0	4.83		141.5	8.96		174.5	10.09		244.0	9.24
109.0	4.35		142.0	9.64		174.5	10.27		244.0	9.14
109.0	4.68		142.0	9.76		175.0	10.04		244.0	9.28
109.0	4.57		142.0	9.30		178.0	10.45		247.0	9.17
112.0	5.05		144.5	9.48		180.5	10.08		247.0	9.00
112.0	5.02		144.5	9.69		180.5	10.29		247.0	9.15

Table B2-4 Continued: Heating Distribution Along Cylinder-Mallinson, No Cowl.

X, mm	Qw, W/cm^2		X, mm	Qw, W/cm^2		X, mm	Qw, W/cm^2		X, mm	Qw, W/cm^2
250.0	9.06		333.0	8.25		392.5	7.14		441.0	7.23
250.0	9.18		339.0	8.18		395.5	7.27		441.0	7.30
256.0	8.90		342.0	7.92		395.5	7.11		441.0	7.09
256.0	8.82		342.0	7.98		398.5	7.21		444.0	7.30
259.0	9.25		348.0	8.02		398.5	7.10		444.0	7.13
259.0	9.17		351.0	8.14		404.5	7.45		444.0	7.10
262.0	8.99		353.5	7.75		404.5	7.25		444.0	6.83
262.0	8.99		353.5	7.82		407.5	7.47		447.0	7.18
265.0	8.72		353.5	7.65		407.5	7.40		447.0	7.09
265.0	8.80		354.0	8.23		407.5	7.12		447.0	7.02
271.0	8.88		356.5	7.76		413.5	7.29		447.0	6.72
271.0	8.92		356.5	7.76		416.5	7.32		450.0	7.08
274.0	8.88		356.5	7.59		419.5	7.39		450.0	6.77
274.0	8.61		357.0	7.99		420.0	7.27		456.0	7.19
274.0	8.76		359.5	7.74		420.0	7.33		456.0	6.87
280.0	8.93		359.5	7.76		420.0	7.45		459.0	6.93
283.0	8.91		359.5	7.64		420.0	7.24		459.0	6.69
286.0	8.62		360.0	8.21		422.5	7.19		462.0	6.93
288.0	8.95		362.5	7.66		423.0	7.32		462.0	6.66
288.0	8.57		362.5	7.69		423.0	7.27		465.0	6.87
289.0	8.82		362.5	7.55		423.0	7.40		465.0	6.63
291.0	8.94		363.0	7.99		423.0	7.23		471.0	6.95
291.0	8.79		365.5	7.60		425.5	7.28		471.0	6.78
292.0	8.89		365.5	7.67		426.0	7.20		474.0	7.02
294.0	8.90		365.5	7.55		426.0	7.34		474.0	7.03
294.0	8.79		366.0	7.97		426.0	7.38		474.0	6.82
295.0	8.66		368.5	7.61		426.0	7.20		474.0	6.64
297.0	8.76		368.5	7.69		428.5	7.16		480.0	7.01
297.0	8.69		368.5	7.59		429.0	7.38		480.0	6.92
298.0	8.64		371.5	7.52		429.0	7.27		483.0	6.71
300.0	8.73		371.5	7.57		429.0	7.32		483.0	6.64
300.0	8.56		371.5	7.47		429.0	7.18		486.0	6.97
303.0	8.79		374.5	7.70		431.5	7.19		486.0	7.02
303.0	8.55		374.5	7.73		432.0	7.24		488.0	6.76
306.0	8.63		374.5	7.64		432.0	7.35		488.0	6.82
306.0	8.37		377.5	7.40		432.0	7.27		489.0	6.97
309.0	8.78		377.5	7.51		432.0	7.09		489.0	6.79
309.0	8.47		377.5	7.38		435.0	7.51		491.0	6.78
312.0	8.44		380.5	7.34		435.0	7.35		491.0	6.81
312.0	8.48		380.5	7.44		435.0	7.31		492.0	6.63
315.0	8.31		380.5	7.27		435.0	7.05		492.0	6.70
315.0	8.38		383.5	7.53		438.0	6.98		494.0	6.77
318.0	8.22		383.5	7.35		438.0	6.83		494.0	6.80
324.0	8.53		389.5	7.58		438.0	7.19		495.0	6.98
327.0	8.46		389.5	7.40		438.0	6.95		495.0	6.79
330.0	8.23		392.5	7.32		441.0	7.28		497.0	6.71

Table B2-4 Concluded: Heating Distribution Along Cylinder-Mallinson, No Cowl.

X, mm	Qw, W/cm^2		X, mm	Qw, W/cm^2		X, mm	Qw, W/cm^2		X, mm	Qw, W/cm^2
497.0	6.76		565.5	6.38		636.5	6.04		725.5	5.74
498.0	7.01		565.5	6.41		636.5	6.08		728.5	5.80
498.0	6.85		566.0	6.44		639.5	6.04		728.5	5.75
500.0	6.67		568.5	6.38		639.5	6.04		731.5	5.71
500.0	6.74		568.5	6.38		642.5	6.04		731.5	5.71
503.0	6.69		568.5	6.40		642.5	6.00		734.5	5.83
503.0	6.75		571.5	6.25		645.5	6.01		734.5	5.80
506.0	6.59		571.5	6.28		645.5	5.99		737.5	5.62
506.0	6.66		571.5	6.31		648.5	6.04		737.5	5.63
509.0	6.79		574.5	6.37		648.5	6.02		740.5	5.58
509.0	6.81		574.5	6.42		651.5	5.94		740.5	5.59
512.0	6.55		574.5	6.48		651.5	5.93		743.5	5.66
512.0	6.60		577.5	6.16		654.5	6.09		749.5	5.80
515.0	6.52		577.5	6.22		654.5	6.06		752.5	5.66
515.0	6.49		577.5	6.20		657.5	5.90		755.5	5.65
518.0	6.56		580.5	6.09		657.5	5.86		758.5	5.65
524.0	6.65		580.5	6.15		660.5	5.86		764.5	5.75
527.0	6.42		580.5	6.09		660.5	5.74		767.5	5.73
530.0	6.36		583.5	6.24		663.5	5.80		767.5	5.65
533.0	6.33		583.5	6.15		669.5	5.86		773.5	5.65
539.0	6.55		589.5	6.36		672.5	5.74		776.5	5.74
542.0	6.42		589.5	6.29		675.5	5.70		779.5	5.79
542.0	6.38		592.5	6.14		678.5	5.67		782.5	5.66
548.0	6.47		592.5	6.12		684.5	5.83		785.5	5.73
551.0	6.57		595.5	6.14		687.5	5.83		788.5	5.63
553.5	6.40		595.5	6.09		687.5	5.75		791.5	5.62
553.5	6.45		598.5	6.11		693.5	5.90		804.7	5.80
553.5	6.39		598.5	6.04		696.5	5.87		808.0	5.85
554.0	6.59		604.5	6.30		699.5	5.92		809.8	5.81
556.5	6.35		604.5	6.18		702.5	5.72		816.5	5.86
556.5	6.45		607.5	6.00		705.5	5.80		819.8	5.85
556.5	6.43		607.5	6.17		708.5	5.81		821.3	5.79
557.0	6.57		607.5	6.11		711.5	5.90		823.1	5.76
559.5	6.36		613.5	6.17		713.5	5.64		828.0	5.76
559.5	6.40		616.5	6.17		713.5	5.77		829.8	5.76
559.5	6.41		619.5	6.21		716.5	5.67		831.3	5.72
560.0	6.60		622.5	6.01		716.5	5.74		833.1	5.69
562.5	6.34		625.5	6.13		719.5	5.69		834.6	5.88
562.5	6.37		628.5	6.05		719.5	5.74		836.4	5.85
562.5	6.43		631.5	6.13		722.5	5.67		838.0	5.71
563.0	6.40		633.5	6.04		722.5	5.74		839.8	5.59
565.5	6.32		633.5	6.07		725.5	5.74			

Table B2-5: Pressure Distribution-Murray 4.7^0 Cowl-1.

X_{TE}, mm	Pw, KPa		X_{TE}, mm	Pw, KPa		X_{TE}, mm	Pw, KPa
-5.0	2.97		48.0	13.51		67.0	20.46
-5.0	2.95		49.0	13.56		67.0	20.86
-5.0	3.03		49.0	12.48		68.0	22.74
5.0	2.93		49.0	13.09		68.0	21.71
5.0	2.92		51.0	14.55		68.0	21.79
5.0	2.97		51.0	13.68		69.0	22.87
15.0	2.84		51.0	14.47		69.0	21.43
15.0	2.90		52.0	14.94		69.0	21.78
15.0	2.94		52.0	14.20		71.0	23.41
25.0	2.91		52.0	14.33		71.0	22.51
25.0	2.86		53.0	15.43		71.0	23.23
25.0	2.92		53.0	15.00		72.0	24.05
35.0	3.01		53.0	15.03		72.0	22.90
35.0	2.91		54.0	15.94		72.0	22.92
35.0	2.93		54.0	15.22		73.0	24.56
36.0	2.96		54.0	15.69		73.0	23.67
36.0	2.95		55.0	16.27		73.0	23.50
36.0	3.04		55.0	15.99		74.0	24.55
37.0	3.14		55.0	16.24		74.0	23.74
37.0	2.98		56.0	16.29		74.0	24.43
37.0	3.06		56.0	15.46		75.0	24.86
38.0	4.43		56.0	15.91		75.0	24.45
38.0	4.66		57.0	16.55		75.0	24.86
38.0	3.93		57.0	16.05		76.0	25.00
39.0	4.00		57.0	16.31		76.0	24.19
39.0	3.72		58.0	17.69		76.0	24.46
39.0	3.65		58.0	17.51		77.0	25.11
41.0	5.89		58.0	17.24		77.0	24.87
41.0	4.89		59.0	17.66		77.0	25.02
41.0	4.72		59.0	17.04		78.0	25.31
42.0	6.10		59.0	17.14		78.0	25.02
42.0	6.23		61.0	18.41		78.0	24.52
42.0	5.07		61.0	18.04		79.0	25.74
43.0	7.24		61.0	18.36		79.0	25.24
43.0	8.12		62.0	18.99		79.0	24.99
43.0	6.98		62.0	18.44		81.0	25.61
44.0	9.93		62.0	18.13		81.0	25.69
44.0	8.63		63.0	19.64		81.0	25.68
44.0	8.00		63.0	19.22		82.0	26.00
45.0	11.10		63.0	18.96		82.0	25.78

Table B2-5 Concluded: Pressure Distribution-Murray 4.7^0 Cowl-1.

X_{TE}, mm	Pw, KPa		X_{TE}, mm	Pw, KPa		X_{TE}, mm	Pw, KPa
86.0	27.39		105.0	27.45		118.0	23.07
86.0	26.98		105.0	27.09		119.0	22.81
86.0	26.50		106.0	27.67		119.0	22.09
87.0	27.99		106.0	27.53		119.0	22.02
87.0	26.63		106.0	27.19		120.0	22.37
87.0	26.76		107.0	27.39		120.0	21.51
88.0	27.53		107.0	26.96		120.0	21.63
88.0	26.72		107.0	27.17		121.0	21.87
88.0	26.37		108.0	26.66		121.0	20.80
90.0	27.88		108.0	26.97		121.0	20.90
90.0	27.05		108.0	27.64		122.0	21.45
90.0	27.01		109.0	26.41		122.0	20.78
92.0	28.34		109.0	26.65		122.0	20.90
92.0	27.24		109.0	26.69		123.0	21.12
92.0	27.20		110.0	26.02		123.0	20.33
94.0	28.32		110.0	26.15		123.0	20.48
94.0	27.52		110.0	26.31		124.0	20.62
94.0	27.22		111.0	25.49		124.0	19.93
95.0	28.74		111.0	25.28		124.0	19.85
95.0	27.27		111.0	25.55		125.0	20.19
95.0	27.09		112.0	25.13		125.0	19.33
96.0	27.91		112.0	25.29		125.0	19.87
96.0	27.91		112.0	25.61		126.0	19.50
96.0	27.28		113.0	24.77		126.0	19.26
97.0	28.37		113.0	24.81		126.0	19.02
97.0	27.44		113.0	25.15		127.0	19.26
97.0	27.47		114.0	24.30		127.0	18.63
98.0	27.82		114.0	24.38		127.0	18.79
98.0	27.43		114.0	24.40		128.0	18.67
98.0	27.06		115.0	23.76		128.0	18.60
100.0	28.07		115.0	23.64		128.0	18.97
100.0	27.74		115.0	24.44		129.0	18.44
100.0	27.46		116.0	24.17		129.0	18.33
102.0	28.27		116.0	23.17		129.0	18.16
102.0	27.75		116.0	23.04		130.0	18.09
102.0	27.45		117.0	23.86		130.0	17.76
104.0	28.10		117.0	22.48		130.0	17.83
104.0	27.84		117.0	22.80		131.0	17.69
104.0	27.37		118.0	23.07		131.0	17.26
105.0	28.28		118.0	22.42		131.0	17.23

Table B2-6: Heating Distribution–Murray 4.7⁰ Cowl-1.

X, mm	Qw, W/cm²		X, mm	Qw, W/cm²		X, mm	Qw, W/cm²
-5.5	6.06		24.4	5.87		54.4	25.30
-5.5	5.95		24.4	5.82		54.4	25.11
-5.5	6.08		24.4	5.84		54.4	25.07
-4.0	5.94		26.0	5.79		55.9	25.58
-4.0	5.71		26.0	5.66		55.9	25.58
-4.0	5.90		26.0	5.66		55.9	25.42
-2.2	5.87		27.8	5.68		57.7	26.62
-2.2	5.70		27.8	5.50		57.7	26.26
-2.2	5.88		27.8	5.58		57.7	26.55
-0.7	5.96		29.3	6.01		59.3	27.12
-0.7	5.89		29.3	5.90		59.3	27.26
-0.7	5.99		29.3	5.88		59.3	27.07
1.1	6.02		31.1	5.96		61.1	28.44
1.1	5.82		31.1	5.81		61.1	28.07
1.1	5.94		31.1	5.87		61.1	28.17
2.6	5.96		32.6	5.80		66.3	35.57
2.6	5.80		32.6	5.71		66.3	34.80
2.6	5.98		32.6	5.67		66.3	36.95
4.5	5.98		34.4	5.70		68.1	37.21
4.5	5.71		34.4	5.20		68.1	36.31
4.5	5.89		34.4	5.31		68.1	37.06
6.0	6.04		36.0	5.26		69.7	35.47
6.0	5.77		36.0	4.64		69.7	34.57
6.0	5.96		36.0	4.61		69.7	36.30
7.8	5.99		37.8	7.72		71.4	36.60
7.8	5.65		37.8	7.72		71.4	36.05
7.8	5.91		37.8	5.10		71.4	36.18
9.3	5.89		39.3	7.45		73.0	38.10
9.3	5.68		39.3	13.63		73.0	37.86
9.3	5.80		39.3	8.93		73.0	38.85
11.1	5.85		41.1	14.45		74.7	39.32
11.1	5.62		41.1	19.38		74.7	39.23
11.1	5.80		41.1	18.83		74.7	38.49
16.0	5.79		45.9	24.59		76.3	37.64
16.0	5.74		45.9	22.32		76.3	37.56
16.0	5.75		45.9	23.73		76.3	38.00
17.8	5.80		47.7	24.86		78.1	38.68
17.8	5.70		47.7	23.57		78.1	38.47
17.8	5.78		47.7	23.96		78.1	37.46
19.3	5.87		49.3	23.79		79.7	39.36
19.3	5.63		49.3	22.64		79.7	39.62
19.3	5.66		49.3	23.67		79.7	39.56
21.1	5.72		51.1	24.26		81.4	40.54
21.1	5.59		51.1	23.78		81.4	40.70
21.1	5.75		51.1	24.17		81.4	39.02
22.6	6.09		52.6	24.59		83.0	43.09
22.6	5.77		52.6	24.04		83.0	43.17
22.6	5.79		52.6	24.44		83.0	43.63

Table B2-6 Concluded: Heating Distribution–Murray 4.7⁰ Cowl-1.

X, mm	Qw, W/cm²		X, mm	Qw, W/cm²
84.7	43.99		111.4	36.21
84.7	44.57		113.0	36.74
84.7	43.02		113.0	36.21
86.3	39.90		113.0	36.27
86.3	39.70		114.7	36.00
86.3	40.44		114.7	36.23
88.1	40.68		114.7	34.56
88.1	40.91		116.3	36.23
88.1	39.44		116.3	35.85
93.0	40.28		116.3	36.27
93.0	37.18		118.0	35.47
93.0	39.72		118.0	35.78
94.7	38.49		118.0	34.15
94.7	38.27		122.9	31.69
94.7	38.48		122.9	30.91
96.3	40.69		122.9	31.28
96.3	40.79		124.7	31.06
96.3	40.51		124.7	30.92
98.1	41.33		124.7	29.62
98.1	42.17		126.3	29.65
98.1	39.50		126.3	29.14
99.6	43.55		126.3	29.39
99.6	43.51		128.0	28.79
99.6	43.88		128.0	29.02
101.4	43.99		128.0	27.73
101.4	44.88		129.6	28.47
101.4	42.69		129.6	27.76
103.0	41.64		129.6	28.10
103.0	41.42		131.4	27.87
103.0	41.74		131.4	27.73
104.7	41.14		131.4	26.53
104.7	41.71		132.9	26.82
104.7	39.77		132.9	26.16
106.3	44.33		132.9	26.71
106.3	43.97		134.7	26.19
106.3	43.89		134.7	26.07
108.0	43.48		134.7	25.09
108.0	43.78		136.3	25.88
108.0	41.38		136.3	27.45
109.6	38.47		136.3	25.53
109.6	38.05		138.0	25.18
109.6	38.27		138.0	25.13
111.4	37.82		138.0	24.06
111.4	37.91			

Table B2-7: Pressure Distribution–Murray 10^0 Cowl-2.

X_{TE}, mm	Pw, KPa		X_{TE}, mm	Pw, KPa		X_{TE}, mm	Pw, KPa
-18.2	2.91		-5.2	2.94		7.8	9.88
-18.2	3.00		-5.2	2.98		8.8	10.03
-18.2	2.93		-4.2	3.00		8.8	10.48
-17.2	2.93		-4.2	2.98		8.8	10.54
-17.2	3.00		-4.2	3.14		9.8	10.43
-17.2	2.93		-3.2	3.01		9.8	10.91
-16.2	2.93		-3.2	3.20		9.8	11.08
-16.2	3.00		-3.2	3.67		10.8	11.04
-16.2	2.93		-2.2	3.02		10.8	11.01
-15.2	2.97		-2.2	3.58		10.8	11.09
-15.2	2.97		-2.2	3.69		11.8	11.49
-15.2	2.92		-1.2	3.64		11.8	11.76
-14.2	2.94		-1.2	3.96		11.8	11.91
-14.2	3.00		-1.2	3.97		12.8	11.95
-14.2	2.93		-0.2	3.80		12.8	12.21
-13.2	2.95		-0.2	4.16		12.8	12.24
-13.2	3.00		-0.2	4.82		13.8	12.15
-13.2	2.94		0.8	4.18		13.8	12.46
-12.2	2.93		0.8	4.26		13.8	12.61
-12.2	3.01		0.8	4.75		14.8	12.71
-12.2	2.97		1.8	4.72		14.8	12.65
-11.2	2.94		1.8	4.95		14.8	12.80
-11.2	3.02		1.8	5.77		15.8	12.99
-11.2	2.95		2.8	4.90		15.8	12.95
-10.2	2.95		2.8	5.47		15.8	12.97
-10.2	3.00		2.8	5.87		16.8	13.42
-10.2	2.92		3.8	5.24		16.8	13.18
-9.2	2.88		3.8	5.87		16.8	13.17
-9.2	2.94		3.8	6.52		17.8	13.45
-9.2	2.86		4.8	6.35		17.8	13.30
-8.2	2.93		4.8	6.86		17.8	13.44
-8.2	2.94		4.8	7.49		18.8	13.31
-8.2	2.92		5.8	7.01		18.8	13.34
-7.2	2.94		5.8	7.50		18.8	13.54
-7.2	2.95		5.8	8.34		19.8	13.55
-7.2	2.97		6.8	8.26		19.8	13.60
-6.2	2.94		6.8	9.24		19.8	13.38
-6.2	2.94		6.8	9.76		20.8	13.53
-6.2	3.00		7.8	8.84		20.8	13.58
-5.2	2.93		7.8	9.85		20.8	13.34

Table B2-7 Continued: Pressure Distribution–Murray 10^0 Cowl-2.

X_{TE}, mm	Pw, KPa		X_{TE}, mm	Pw, KPa		X_{TE}, mm	Pw, KPa
21.8	13.22		34.8	27.16		47.8	58.56
21.8	13.64		34.8	28.55		48.8	59.13
21.8	13.37		35.8	29.56		48.8	56.80
22.8	13.67		35.8	29.94		48.8	60.66
22.8	13.99		35.8	30.94		49.8	62.00
22.8	13.90		36.8	30.61		49.8	60.52
23.8	13.95		36.8	31.44		49.8	63.36
23.8	14.38		36.8	31.62		50.8	63.10
23.8	14.27		37.8	32.71		50.8	61.66
24.8	15.04		37.8	33.29		50.8	66.59
24.8	15.04		37.8	34.50		51.8	64.22
24.8	15.04		38.8	35.22		51.8	64.69
25.8	14.78		38.8	36.32		51.8	65.88
25.8	15.38		38.8	36.32		52.8	66.25
25.8	16.08		39.8	38.22		52.8	65.66
26.8	16.34		39.8	37.55		52.8	68.61
26.8	16.90		39.8	38.72		53.8	68.35
26.8	17.64		40.8	38.95		53.8	67.69
27.8	17.69		40.8	38.81		53.8	69.31
27.8	17.69		40.8	40.93		54.8	69.83
27.8	18.89		41.8	40.51		54.8	68.32
28.8	18.83		41.8	40.86		54.8	70.55
28.8	18.98		41.8	41.98		55.8	70.92
28.8	20.06		42.8	43.38		55.8	69.25
29.8	19.69		42.8	43.61		55.8	72.04
29.8	20.25		42.8	46.74		56.8	71.39
29.8	21.81		43.8	46.15		56.8	69.20
30.8	21.34		43.8	46.38		56.8	70.75
30.8	21.51		43.8	48.53		57.8	70.42
30.8	22.17		44.8	47.87		57.8	68.55
31.8	22.11		44.8	47.99		57.8	70.75
31.8	22.06		44.8	50.90		58.8	72.26
31.8	22.73		45.8	51.25		58.8	68.02
32.8	24.24		45.8	51.45		58.8	69.77
32.8	24.20		45.8	54.14		59.8	70.66
32.8	25.46		46.8	53.55		59.8	66.74
33.8	26.12		46.8	53.50		59.8	67.19
33.8	26.20		46.8	55.12		60.8	68.92
33.8	27.20		47.8	55.43		60.8	65.86
34.8	26.95		47.8	55.84		60.8	68.73

Table B2-7 Concluded: Pressure Distribution–Murray 10^0 Cowl-2.

X_{TE}, mm	Pw, KPa		X_{TE}, mm	Pw, KPa		X_{TE}, mm	Pw, KPa
61.8	68.27		69.8	52.55		77.8	42.50
61.8	69.82		69.8	52.80		78.8	41.29
61.8	69.06		70.8	52.58		78.8	41.29
62.8	65.14		70.8	51.64		78.8	40.74
62.8	64.43		70.8	53.60		79.8	39.89
62.8	65.71		71.8	53.94		79.8	39.02
63.8	63.56		71.8	52.43		79.8	38.13
63.8	62.70		71.8	52.12		80.8	39.09
63.8	63.44		72.8	49.14		80.8	38.30
64.8	61.73		72.8	49.14		80.8	38.55
64.8	61.61		72.8	48.78		81.8	39.39
64.8	61.89		73.8	48.68		81.8	40.11
65.8	60.08		73.8	47.47		81.8	39.40
65.8	59.82		73.8	46.93		91.8	29.74
65.8	61.29		74.8	47.52		91.8	29.39
66.8	59.05		74.8	46.71		91.8	29.47
66.8	58.02		74.8	45.28		101.8	22.59
66.8	59.75		75.8	45.53		101.8	22.05
67.8	56.53		75.8	44.88		101.8	22.20
67.8	56.17		75.8	44.82		111.8	17.65
67.8	58.09		76.8	44.57		111.8	17.22
68.8	56.64		76.8	43.09		111.8	17.78
68.8	55.37		76.8	43.81		121.8	13.92
68.8	56.09		77.8	42.53		121.8	14.07
69.8	53.83		77.8	41.75		121.8	14.10

Table B2-8: Heating Distribution–Murray 10^0 Cowl-2.

X, mm	Qw, W/cm²		X, mm	Qw, W/cm²		X, mm	Qw, W/cm²
-51.6	6.17		-21.0	5.55		1.6	5.22
-51.6	5.90		-21.0	5.97		2.8	9.10
-51.6	6.26		-19.3	5.93		2.8	10.80
-49.9	6.20		-19.3	5.73		2.8	14.84
-49.9	6.00		-19.3	5.72		3.3	5.19
-49.9	6.12		-14.2	6.35		3.3	8.16
-44.8	5.85		-14.2	5.65		3.3	8.15
-44.8	5.62		-14.2	6.47		4.5	12.69
-44.8	6.01		-12.5	6.27		4.5	15.05
-43.1	5.89		-12.5	6.01		4.5	15.23
-43.1	5.74		-12.5	6.34		5.0	10.97
-43.1	5.81		-10.8	5.86		5.0	13.81
-41.4	6.02		-10.8	5.68		5.0	12.92
-41.4	5.69		-10.8	5.89		5.8	9.19
-41.4	6.08		-9.1	5.91		5.8	12.10
-39.7	6.02		-9.1	5.72		5.8	9.19
-39.7	5.84		-9.1	5.79		6.2	13.92
-39.7	5.86		-7.4	5.92		6.2	13.92
-38.0	6.19		-7.4	5.63		6.2	15.01
-38.0	5.94		-7.4	5.72		6.7	12.90
-38.0	6.33		-5.7	5.88		6.7	16.50
-36.3	6.17		-5.7	5.67		6.7	15.77
-36.3	6.03		-5.7	5.61		7.9	15.32
-36.3	6.05		-5.2	6.21		7.9	14.88
-34.6	5.83		-5.2	6.51		7.9	14.93
-34.6	5.61		-5.2	6.51		8.4	15.32
-34.6	6.01		-4.0	6.20		8.4	15.32
-32.9	5.84		-4.0	5.78		8.4	15.66
-32.9	5.75		-4.0	5.98		9.2	15.37
-32.9	5.71		-3.5	6.32		9.2	15.76
-31.2	6.14		-3.5	6.32		9.2	14.97
-31.2	5.92		-3.5	6.32		9.6	15.37
-31.2	6.32		-2.3	5.83		9.6	14.33
-29.5	6.19		-2.3	5.10		9.6	13.62
-29.5	6.01		-2.3	5.15		10.1	15.67
-29.5	6.03		-1.8	6.07		10.1	14.94
-27.8	5.83		-1.8	6.43		10.1	14.59
-27.8	5.72		-1.8	5.87		11.3	14.57
-27.8	5.99		-0.6	4.96		11.3	14.00
-26.1	5.90		-0.6	5.34		11.3	13.98
-26.1	5.75		-0.6	8.07		12.6	14.83
-26.1	5.79		-0.1	5.99		12.6	13.67
-24.4	5.80		-0.1	5.26		12.6	13.37
-24.4	5.58		-0.1	5.17		15.2	13.94
-24.4	5.92		1.1	5.99		15.2	12.64
-22.7	5.91		1.1	8.73		15.2	12.89
-22.7	5.66		1.1	8.44		16.0	15.88
-22.7	5.70		1.6	5.45		16.0	15.31
-21.0	5.83		1.6	5.65		16.0	14.65

Table B2-8 Concluded: Heating Distribution–Murray 10^0 Cowl-2.

X, mm	Qw, W/cm²		X, mm	Qw, W/cm²		X, mm	Qw, W/cm²
16.9	13.50		36.4	44.38		56.8	87.54
16.9	11.41		36.4	45.49		57.7	90.74
16.9	11.09		37.3	45.44		57.7	91.54
18.6	12.88		37.3	46.43		57.7	91.47
18.6	12.74		37.3	46.72		59.4	79.88
18.6	13.04		39.0	48.77		59.4	84.54
19.4	13.49		39.0	48.52		59.4	82.44
19.4	13.27		39.0	48.62		60.2	80.69
19.4	12.77		39.8	56.04		60.2	84.02
20.3	12.72		39.8	56.04		60.2	82.10
20.3	11.74		39.8	58.32		61.1	81.58
20.3	12.59		40.7	52.24		61.1	83.70
22.0	13.41		40.7	53.60		61.1	82.05
22.0	13.83		40.7	53.28		62.8	93.77
22.0	14.32		43.2	56.47		62.8	99.29
23.7	16.47		43.2	59.02		62.8	95.50
23.7	15.85		43.2	59.16		63.6	78.85
23.7	17.30		45.8	68.10		63.6	81.61
25.4	19.68		45.8	69.91		63.6	79.74
25.4	18.78		45.8	68.45		64.5	94.76
25.4	19.16		46.6	64.92		64.5	97.73
26.2	19.68		46.6	66.86		64.5	95.11
26.2	19.62		46.6	67.92		66.2	80.59
26.2	21.66		47.5	73.33		66.2	84.82
27.1	23.50		47.5	75.37		66.2	82.61
27.1	22.22		47.5	73.71		67.0	80.43
27.1	24.15		49.2	71.78		67.0	84.55
28.8	28.55		49.2	72.87		67.0	82.13
28.8	27.52		49.2	71.50		67.9	80.73
28.8	28.14		50.0	72.11		67.9	83.98
29.6	28.79		50.0	74.42		67.9	81.66
29.6	27.95		50.0	74.84		69.6	75.74
29.6	29.81		50.9	76.00		69.6	82.40
30.5	29.68		50.9	76.11		69.6	78.32
30.5	31.48		50.9	76.35		70.4	70.04
30.5	35.31		52.6	77.11		70.4	73.36
32.2	36.17		52.6	82.27		70.4	70.87
32.2	35.90		52.6	78.31		71.3	76.02
32.2	36.41		53.4	73.06		71.3	79.55
33.0	37.65		53.4	73.06		71.3	76.65
33.0	37.65		53.4	73.06		73.8	78.13
33.0	39.23		54.3	83.79		73.8	81.79
33.9	40.61		54.3	84.27		73.8	79.04
33.9	39.53		54.3	83.10		77.2	65.83
33.9	41.23		56.0	87.40		77.2	69.44
35.6	42.75		56.0	92.67		77.2	66.08
35.6	41.81		56.0	88.94		80.6	60.84
35.6	42.50		56.8	87.32		80.6	63.97
36.4	42.99		56.8	89.40		80.6	61.20

Baseline Computations. Selected computations follow that provide a baseline for those wanting to compute the experiments documented above. The baseline is intended to facilitate and gage new code development and turbulence model improvements. These computations were previously obtained and published by NASA during their assessment of uncertainty related to hypersonic simulations of SWBLI. See Ref. B2-4.

Although the flow is axisymmetric, all solutions provided made use of the 3D formulation of DPLR. The grid for the separated case made use of 5 blocks having 512 cells between the test cylinder and shock generator, with a total of 1696 cells streamwise. A quarter-plane (90°) grid was used for the axisymmetric problem with cells placed every 10°. The spacing of the first cell off the cylinder surface was at $y_1^+ \cong 0.01$. Transition was specified to agree with the location and extent observed in the wall heating data from Ref. B2-1.

The facility calibration data presented by Mallinson et al. was used in the baseline DPLR solutions to account for the "weak" favorable pressure gradient in the facility test section, present at the high Reynolds number condition used for these test data. The flow angle at the inlet face of the computational domain was calculated from a curve fit of flow deflection angle (figure 14 of Ref. B2-3) at the nozzle exit plane. The divergence angle may be described by $\alpha \approx A * R$, where A=5°/meter, $R = \text{sqrt}(y^2 + z^2)$ is the distance off-centerline at the X-station of the cylinder leading edge. As the freestream is not at uniform conditions, the "nominal test conditions" are not used, but rather the computational domain inlet conditions are adjusted to best match the measured wall pressure over the test cylinder. These computational domain inlet conditions were adjusted to M_i=8.85 with total pressure of 60MPa resulting in U_i=1498.57 m/sec, T_i=69 °K, and ρ_i =0.15509 kg/m^3. The flow angularity is then accounted for in the DPLR solutions, presented herein, by use of a specified pointwise boundary condition at the inlet face of the computational domain by $u_i=U_i*\cos(\alpha)$, $v_i=U_i*\sin(\alpha)*\cos(\text{atan}(y/z))$, and $w_i=U_i*\sin(\alpha)*\sin(\text{atan}(y/z))$, where y and z are for the center of each cell face of the inlet computational domain. A simple fortran program to provide the DPLR pointwise boundary condition file, given the grid to be used, is included on the companion DVD.

Keyes viscosity relationship for Nitrogen, N_2, was used for all computations, where:

$$\mu = A\, T^{0.5}/(1.0+(B/T)*10^{(-C/T)})$$

Keyes viscosity constants for molecular Nitrogen (N_2) are: A =1.418 10^{-6}, B =116.4 K, and C = 5.0 K; while for dry air, they are A =1.458 10^{-6}, B =122.1 K, and C = 5.0 K. The units for dynamic viscosity are kg/(m-sec) (also Pa-sec, or equivalently N-sec/m^2), and temperature is specified in degrees Kelvin.

Example DPLR input files, inlet pointwise boundary condition files and ascii plot3d grid files may be found on the companion DVD for each case considered. For these cases, the nominal freestream conditions appearing in the DPLR input deck are not used as they are overwritten by the values appearing in the pointwise boundary condition files.

Figures B2-1 and B2-2 depict the wall pressure and wall heating, respectively, from DPLR solutions for the test cylinder without the impinging shock Cowl. Presented are the results from DPLR solutions obtained with both: a) the nominal uniform freestream test conditions; and, b) the pointwise inlet boundary condition accounting for the diverging nozzle streamlines as described above. The pointwise inlet boundary condition improves agreement between the RANS solution results and experiment in the wall pressure, but with residual discrepancies in wall heating over the length of the cylinder. Note that X is the distance from the cylinder leading edge.

Figures B2-3 and B2-4 compare the experimental and DPLR results for the wall pressure and wall heating, respectively, for the attached SWTBLI of Cowl-1. There is agreement between the solution results with the experiment for both pressure and heating levels, and also for shock impingement location. Note that XTE is the distance from the cowl trailing edge.

Figures B2-5 and B2-6 compare the experimental and DPLR results for the wall pressure and wall heating, respectively, for the separated SWTBLI of Cowl-2. The agreement between the solution results with the experiment is not as satisfactory as for the attached case.

For more discussion comparing the DPLR solutions with the experiment, see Ref. B2-4.

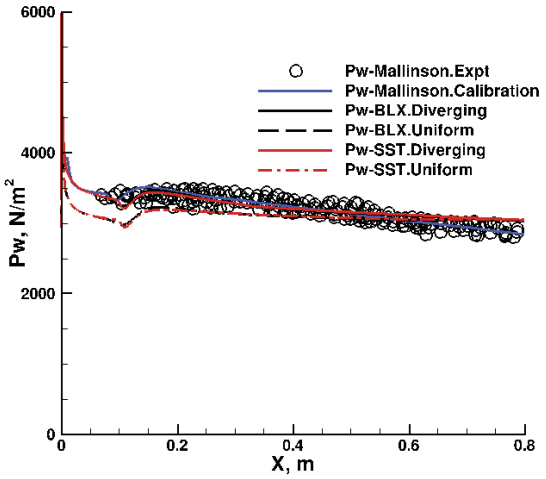

Figure B2-1. Wall Pressure-Mallinson Cyl.

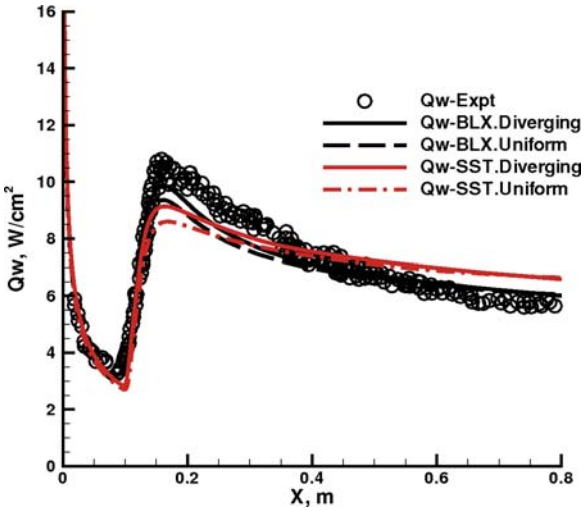

Figure B2-2. Wall Heating-Mallinson Cyl.

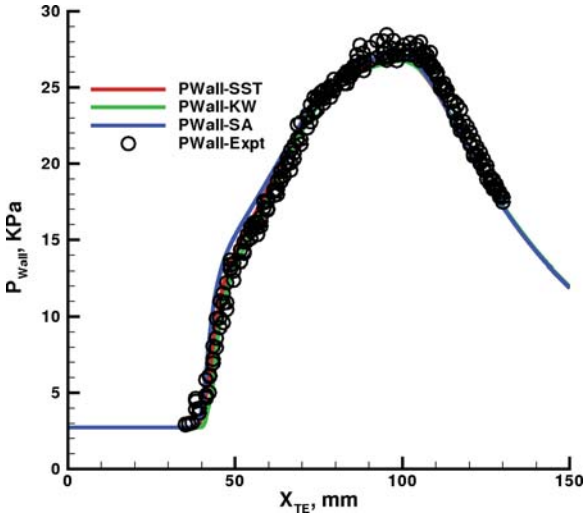

Figure B2-3. Wall Pressure-Murray 4.7° Cowl-1.

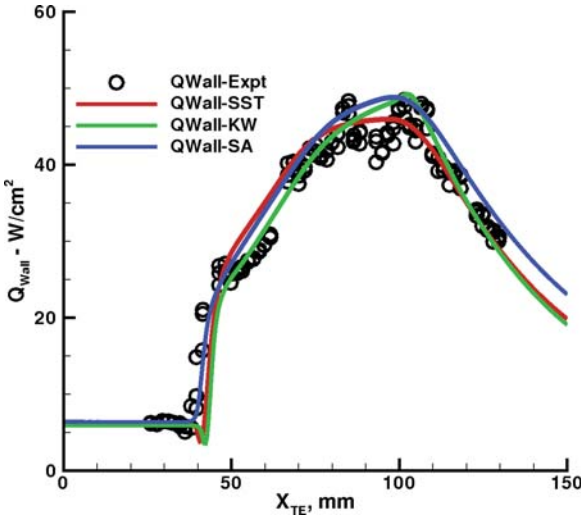

Figure B2-4. Wall Heating-Murray 4.7° Cowl-1.

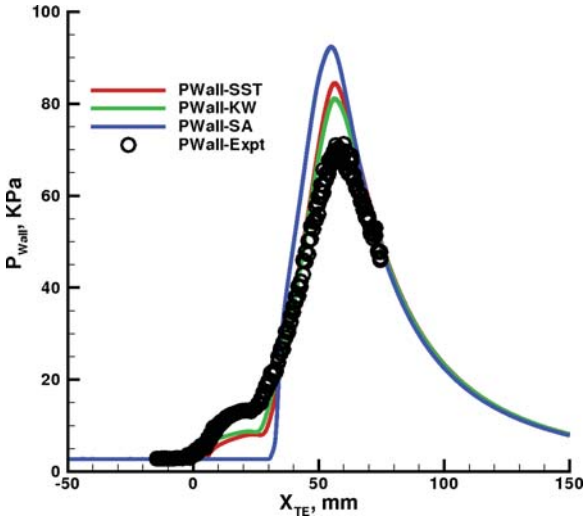

Figure B2-5. Wall Pressure-Murray 10° Cowl-2.

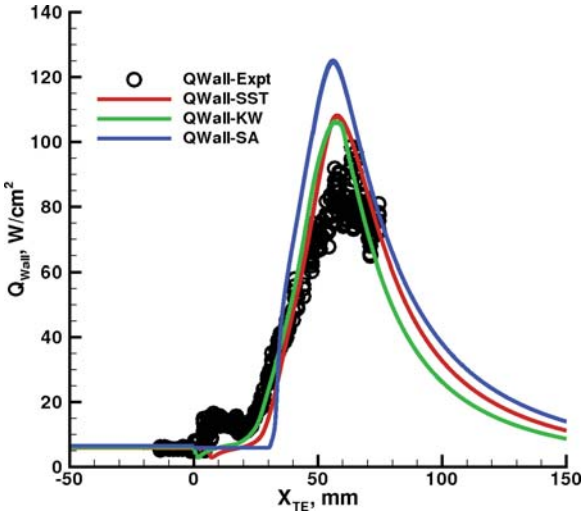

Figure B2-6. Wall Heating-Murray 10° Cowl-2.

B3. Kussoy and Horstman - 2D Impinging Shock

Ref. B3-1. Kussoy, M.I. and Horstman, K.C., Documentation of Two- and Three-Dimensional Shock-Wave/Turbulent-Boundary-Layer Interaction Flows at Mach 8.2, NASA TM 103838, May 1991.

Ref. B3-2. Bose, D., Brown, J.L., Prabhu, D.K., Gnoffo, P.A., Johnston, C.O. and Hollis, B., "Uncertainty Assessment of Hypersonic Aerothermodynamics Prediction Capability," AIAA Paper 2011-3141, 42nd AIAA Thermophysics Conference, Honolulu, Hawaii, June 27-30, 2011.

Ref. B3-3. Brown, J.L., "Shock Wave Impingement on Boundary Layers at Hypersonic Speeds: Computational Analysis and Uncertainty", AIAA Paper 2011-3143, 42nd AIAA Thermophysics Conference, Honolulu, Hawaii, June 27-30, 2011.

General description. Experiments were conducted in the now decommissioned Ames 3.5 foot Hypersonic wind tunnel using dry Air at nominal Mach number of 8.2. Nominal test conditions were P_0 =60 atm., T_0 = 1166^0 K, and free stream Reynolds number of $5x10^6$ per meter. In the test section, a wedge was mounted above an instrumented flat plate test bed and positioned to generate a shockwave that impinged on the test plate. The data include surface pressure and heat transfer distributions as well a mean flow field survey in the undisturbed boundary layer on the plate in the absence of the wedge apparatus. Data users are encouraged to consult the cited Ref. B3-1 for a complete discussion of these data.

Experimental arrangement. The experimental geometry and wedge shock generator orientations are shown in Fig. 1 below taken from Ref. B3-1. The test plate was 76cm wide and 220 cm long. It was water-cooled and the nominal wall temperature was 300^0 K. The wall temperature increased by about 5^0K during the test runs, with cooling turned off for the heat transfer runs.

Three wedges with angles, $\theta_m = 5^0, 10^0$, and 15^0, were used to generate impinging shocks. These un-instrumented wedges were 76 cm wide, 61 cm long, and 5 cm thick at the rear. They were supported over the test bed by two thin plates (one on each side) that held the wedge so that its leading edge was 10.16 cm from the flat plate surface. The rear support plates had slots, which allowed the wedge to be rotated with respect to the flat plate in order to set various wedge angles, θ.

θ (deg)	θ_m	θ^*	X_0 (cm)
5	5	0	104-124
8	10	2	119-135
9	10	1	119-135
10	10	0	124-140
11	15	4	130-145

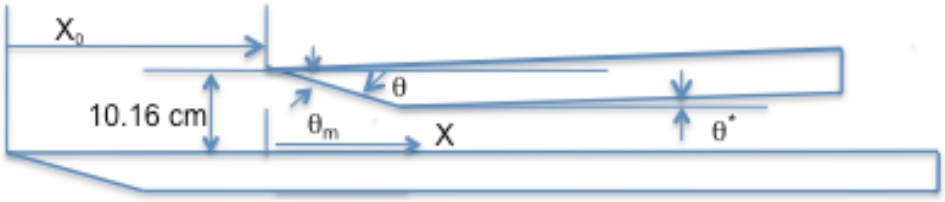

Figure B3-1. Kussoy Wedge geometry and orientation.

To obtain improved spatial resolution data through the interaction region, the wedge was moved between tunnel runs in the stream-wise direction, x_0, while the instrumentation ports on the flat plate remain fixed. As a consequence of this wedge movement, the incident shock-wave impingement point increased about 15% in a distance corresponding to the difference between the farthest upstream and downstream positioning of the wedge. Associated with this increased boundary layer run, the boundary layer thickness also increased slightly at the beginning of the impingement interaction. It was noted that this had little effect on the experimental results provided they were compared at an equivalent distance from the wedge leading edge. X, as reported in the tables, is measured along the test surface, not from the test surface leading edge, but from the projection of the shock generator leading edge normal onto the test flat plate, as shown in Fig. B3-1. The total running length for a boundary layer at a specified X-position on the flat plate is thus, $X_r=X+X_0$.

Facility. The tests were performed in the Ames Research Center 3.5 Foot Wind tunnel. (Presently inoperable.) This blow-down tunnel consisted of high- pressure cylindrical storage tanks, a ceramic pebble bed heater to prevent air liquefaction, an axisymmetric nozzle with an exit diameter of 1.067 meters, a large free-jet test section and diffuser, and four large diameter evacuated spheres that collected the blown air. Test times were in the order of 3 minutes. The open jet design allowed models to remain outside the stream until the required flow conditions were established. Models were then rapidly inserted, and just as rapidly retracted prior to tunnel shutdown. The test core diameter was approximately 0.6 m. Useful test time

was three minutes. Run to run variations in pressure and Mach number was less than 0.5%. The wind tunnel total temperature varied up to 50^0 K from run to run and, in addition, during a single run it varied about 50^0 K over the 3-min test time. These variations required special data reduction procedures described in Ref. B3-1.

Measurements. Natural transition to turbulent flow was stated to occur on the test plate between 50 and 100 cm from the leading edge (100 cm representing the end of transition). Two dimensionality of the flow was verified with surface oil flow streak photographs and with pressure and heat transfer measurements across 18 cm of the span, obtained by rotating the instrumentation port normal to the stream flow direction at the 160 and 190 cm locations.

The undisturbed boundary layer was measured at 187 cm from the plate leading edge. Pitot pressure and total and static temperatures were measured using a survey mechanism. For the flow field quantities, the estimated uncertainties are given as: $\pm$2% for the total temperature, $\pm$ 10% for static pressure, $\pm$6% for the static temperature, $\pm$12% for the density, $\pm$3% for the velocity, and $\pm$5% for the pitot pressure. The uncertainty in Y was $\pm$0.02cm. Static pressure was assumed constant across the boundary layer to obtain the inferred profile data for the undisturbed flat plate boundary layer. (See Ref. B3-1 for discussion and justification.)

Surface pressures and heat transfer were measured along the test plate surface using instrumentation ports fitted flush into the test plate. The surface static pressure taps were 0.16 cm in diameter and connected with short lengths of stainless steel tubing (10 to 15 cm long) to individual strain gauge differential pressure transducers (PSI brand) that were water-cooled. Estimated pressure measurement uncertainty was quoted as $\pm$10%. The heat transfer rates were measured by two means: a transient thin-skin method; and, a thermopile method. The transient thin-skin method made use of chromel-constantan thermocouples spot welded to the test bed, and relied on a 10 − 50 deg K temperature rise (with cooling disconnected) during a 20-second heat-transfer run. The thermopile method made use of Schmidt-Boelter gauges, measuring a temperature difference across a known substrate. Surface heat transfer uncertainty due to variations in total temperature of up to 50 deg K or about 0.5% was corrected, by a simple procedure described in Ref. B3-1. Overall uncertainty in Heat Transfer included uncorrected lateral conduction effects and is cited to be ±10%. Pitot and static pressure surveys were reported for the test plate in the absence of the wedge shock generator apparatus. For these measurements x_0 was 187 cm and downstream of the location for the experiments with the wedge shock generators. Skin friction, obtained with the Van Driest II formulation, and boundary layer properties were tabulated for this location to provide evidence of a fully developed un-tripped boundary layer.

Data tables. The data below are taken from the tables given in Ref. B3-1.

Table B3-1. Undisturbed Flat Plate Boundary Layer, x = 187 cm.

M_∞ =8.18	U_∞ = 1446 m/sec	T_w =300 °K
p_∞= 430 N/m^2	T_∞ =81 °K	ρ_∞= 0.0187 kg/m^3
Re_∞/m = 4.9 x 10^6	$Re\delta_o$ =1.8 x 10^5	$Re\theta_o$ =4600
δ_0 = 3.7 cm	δ^*_0 = 1.59 cm	θ_0 = 0.094 cm
$Q_{w\infty}$=1.04 W/cm^2 (x=162cm)	τ_W = 19.6 N/m^2	cf_∞= 9.8 x 10^{-4} (x=187cm)

Table B3-2. Upstream boundary layer, x= 187cm.

Y, cm	M	p/p_∞	ρ/ρ_∞	T/T_∞	u/u_∞	$\rho u/(\rho u)_\infty$	$T0/T0_\infty$
0.00	0.000	1.00	0.270	3.699	0.000	0.000	0.270
0.07	1.777	1.00	0.213	4.705	0.481	0.102	0.555
0.14	2.069	1.00	0.195	5.138	0.584	0.114	0.682
0.20	2.647	1.00	0.237	4.217	0.678	0.161	0.721
0.28	3.083	1.00	0.266	3.756	0.746	0.199	0.773
0.36	3.409	1.00	0.295	3.390	0.784	0.231	0.798
0.43	3.558	1.00	0.301	3.323	0.810	0.244	0.828
0.50	3.747	1.00	0.333	3.002	0.811	0.270	0.808
0.71	4.068	1.00	0.345	2.897	0.864	0.298	0.877
0.92	4.422	1.00	0.386	2.593	0.889	0.343	0.894
1.12	4.750	1.00	0.419	2.388	0.916	0.384	0.922
1.32	5.106	1.00	0.453	2.205	0.947	0.429	0.956
1.52	5.461	1.00	0.504	1.982	0.960	0.484	0.963
1.72	5.774	1.00	0.560	1.785	0.963	0.539	0.956
1.92	6.101	1.00	0.600	1.668	0.984	0.590	0.981
2.13	6.411	1.00	0.671	1.490	0.977	0.656	0.959
2.32	6.689	1.00	0.705	1.419	0.995	0.701	0.983
2.51	7.009	1.00	0.768	1.302	0.998	0.767	0.981
2.71	7.246	1.00	0.820	1.220	0.999	0.819	0.977
3.04	7.617	1.00	0.865	1.156	1.023	0.884	1.012
3.38	7.978	1.00	0.944	1.060	1.025	0.968	1.011
3.73	8.180	1.00	1.000	1.000	1.021	1.021	1.000
4.07	8.180	1.00	0.995	1.005	1.024	1.019	1.004

Table B3-3. (a) Surface Pressures, Wedge Angle = 5^0

X, cm	p/p_∞		X, cm	p/p_∞		X, cm	p/p_∞
31.36	0.998		46.60	3.210		56.76	6.016
32.36	1.038		47.60	3.645		57.76	6.161
33.36	1.064		48.60	3.968		58.76	6.306
34.35	1.006		49.59	4.242		59.75	6.387
35.35	1.074		50.59	4.419		60.75	6.516
36.38	1.089		51.62	4.823		61.78	6.613
37.36	1.094		52.60	4.952		62.76	6.677
38.36	1.043		53.60	5.194		63.76	6.774
39.36	1.032		54.60	5.323		64.76	6.871
40.36	1.036		55.60	5.548		65.76	6.952
41.36	1.043		56.60	5.629		66.76	7.048
42.36	1.264		57.60	5.903		67.76	7.065
43.35	1.845		58.59	6.016		68.75	7.113
44.35	2.321		59.59			69.75	7.113
45.35	3.434		60.59	6.258		70.75	7.161
46.35			61.59			71.75	7.177
47.35	4.226		62.59	6.516		72.75	7.161

Table B3-3. (b) Surface Heat Transfer, Wedge Angle = 5^0

Thermocouples

X, cm	Q/Q_∞		X, cm	Q/Q_∞		X, cm	Q/Q_∞
36.44	0.94		46.60	2.81		56.76	4.02
37.42	0.92		47.58	3.21		57.74	4.16
38.43	0.93		48.59	3.54		58.75	4.27
39.41	0.95		49.57	3.71		59.73	4.37
40.37	0.94		50.53	3.85		60.69	4.45
41.36	0.94		51.52	3.86		61.68	4.51
42.36	0.95		52.52	4.03		62.68	4.52
43.37	0.97		53.53	4.03		63.69	4.58
45.39	1.50		55.55	4.26		65.71	4.67
46.39	2.10		56.55	4.28		66.71	4.69
47.39	2.71		57.55	4.30		67.71	4.50
49.65	3.61		59.81	4.55		69.97	4.62
50.40	3.75		60.56	4.46		70.72	4.61
52.44	4.00		62.60	4.61		72.76	4.47

Schmidt-Boelter gauges

X, cm	Q/Q_∞		X, cm	Q/Q_∞		X, cm	Q/Q_∞
36.34	1.07		46.50	2.80		56.66	4.79
38.14	0.96		48.30			58.46	4.64
39.94			50.10	3.96		60.26	
41.74	0.97		51.90	3.95		62.06	4.73
43.54	1.01		53.70			63.86	5.33
45.34	1.53		55.50	4.28		65.66	5.16
47.14	2.68		57.30	4.61		67.46	5.30
48.94	3.52		59.10	4.84		69.26	4.72
50.74	3.41		60.90	4.73		71.06	4.79
52.54	3.76		62.70	5.06		72.86	5.78

Table B3-4. (a) Surface Pressure, Wedge Angle = 8^0

X, cm	p/p_∞		X, cm	p/p_∞
26.28	1.01		41.52	13.07
27.28	1.00		42.52	13.60
28.28	1.01		43.52	14.24
29.27	1.02		44.51	14.38
30.27	1.11		45.51	14.37
31.30	1.52		46.54	13.42
32.28	1.83		47.52	12.08
33.28	2.75		48.52	10.80
34.28	4.18		49.52	9.62
35.28			50.52	
36.28	7.56		51.52	7.75
37.28	8.89		52.52	6.95
38.27	10.11		53.51	6.31
39.27	11.22		54.51	5.71
40.27	12.30		55.51	5.24
41.27	13.19		56.51	4.83
42.27	13.62		57.51	4.43

Table B3-4. (b) Surface Heat Transfer, Wedge Angle = 8^0

Thermocouples

X, cm	Q/Q_∞		X, cm	Q/Q_∞
26.28	0.99		41.52	8.99
27.26	1.01		42.50	9.49
28.27	1.01		43.51	9.82
29.25	1.01		44.49	9.64
30.21	0.98		45.45	9.72
31.20	0.88		46.44	9.48
32.20	0.91		47.44	8.66
33.21	1.38		48.45	7.71
35.23	5.08		50.47	6.26
36.23	6.62		51.47	5.73
37.23	7.04		52.47	4.93
39.49	8.31		54.73	4.17
40.24	8.33		55.48	3.74
42.28	9.20		57.52	3.25

Schmidt-Boelter gauges

X, cm	Q/Q_∞		X, cm	Q/Q_∞
26.18	1.27		41.42	8.73
27.98	1.14		43.22	8.87
29.78	3.41		45.02	0.00
31.58	0.00		46.82	7.78
33.38	0.00		48.62	7.75
35.18	5.71		50.42	5.93
36.98	7.73		52.22	5.16
38.78	8.74		54.02	3.00
40.58	8.83		55.82	3.75
42.38	9.65		57.62	5.16

Table B3-5. (a) Surface Pressure, Wedge Angle = 9^0

X, cm	p/p_∞		X, cm	p/p_∞
26.28	1.01		41.52	18.68
27.28	1.05		42.52	19.17
28.28	1.21		43.52	19.17
29.27	1.48		44.51	17.86
30.27	1.86		45.51	15.99
31.30	2.34		46.54	14.00
32.28	3.19		47.52	12.29
33.28	5.08		48.52	10.87
34.28	7.29		49.52	9.65
35.28			50.52	
36.28	11.26		51.52	7.80
37.28	12.97		52.52	7.01
38.27	14.53		53.51	6.39
39.27	15.71		54.51	5.82
40.27	16.77		55.51	5.39
41.27	17.42		56.51	5.00
42.27	18.07		57.51	4.61

Table B3-5. (b) Surface Heat Transfer, Wedge Angle = 9^0

Thermocouples

X, cm	Q/Q_∞		X, cm	Q/Q_∞
26.28	1.18		41.52	11.53
27.26	1.24		42.50	12.12
28.27	1.14		43.51	12.12
29.25	0.99		44.49	11.13
30.21	0.97		45.45	10.14
31.20	1.33		46.44	9.39
32.20	2.38		47.44	8.32
33.21	4.44		48.45	7.44
35.23	8.33		50.47	5.93
36.23	9.21		51.47	5.44
37.23	9.01		52.47	4.69
39.49	11.04		54.73	4.04
40.24	10.84		55.48	3.58
42.28	11.75		57.52	3.17

Schmidt-Boelter gauges

X, cm	Q/Q_∞		X, cm	Q/Q_∞
26.18	1.27		41.42	8.73
27.98	1.14		43.22	8.87
29.78	3.41		45.02	0.00
31.58	0.00		46.82	7.78
33.38	0.00		48.62	7.75
35.18	5.71		50.42	5.93
36.98	7.73		52.22	5.16
38.78	8.74		54.02	3.00
40.58	8.83		55.82	3.75
42.38	9.65		57.62	5.16

Table B3-6. (a) Surface Pressure, Wedge Angle = 10^0

X, cm	p/p_∞		X, cm	p/p_∞		X, cm	p/p_∞
21.20	1.040		21.20	1.048		41.52	21.396
22.20	0.985		22.20	1.016		42.52	21.396
23.20	1.018		23.20	1.008		43.52	19.480
24.19	1.037		24.19	1.018		44.51	17.085
25.19	1.000		25.19	1.108		45.51	14.946
26.22	1.152		26.22	1.468		46.54	12.998
27.20	1.392		27.20	1.855		47.52	11.305
28.20	1.790		28.20	2.274		48.52	9.932
29.20	2.081		29.20	2.710		49.52	8.814
30.20	2.726		30.20	0.000		50.52	7.888
31.20	3.597		31.20	4.774		51.52	7.074
32.20	5.452		32.20	6.677		52.52	6.435
33.19	7.726		33.19	8.903		53.51	5.860
34.19	9.048		34.19	11.113		54.51	4.615
35.19	12.290		35.19	13.274		55.51	4.950
36.19	14.629		36.19	15.419		56.51	4.678

Table B3-6. (b) Surface Heat Transfer, Wedge Angle = 10^0

Thermocouples

X, cm	Q/Q_∞		X, cm	Q/Q_∞		X, cm	Q/Q_∞
21.20	1.01		21.20	0.94		41.52	13.61
22.18	1.03		22.18	0.93		42.50	13.61
23.19	1.05		23.19	0.95		43.51	12.71
24.17	1.00		24.17	0.96		44.49	11.31
25.13	1.01		25.13	0.95		45.45	9.98
26.12	1.01		26.12			46.44	9.71
27.12	0.89		27.12	0.88		47.44	7.79
28.13	0.87		28.13	0.72		48.45	6.29
30.15	1.76		30.15	1.42		50.47	5.53
31.15	3.14		31.15	2.39		51.47	4.76
32.15	5.21		32.15	4.39		52.47	4.46
34.41	9.04		34.41	8.73		54.73	3.82
35.16	9.37		35.16	9.15		55.48	3.47
37.20	10.86		37.20	10.60		57.52	2.98

Schmidt-Boelter gauges

X, cm	Q/Q_∞		X, cm	Q/Q_∞		X, cm	Q/Q_∞
21.10	1.34		21.10	0.92		41.42	10.81
22.90	1.21		22.90			43.22	15.21
24.70			24.70	0.94		45.02	8.88
26.50	1.19		26.50	0.95		46.82	6.91
28.30	1.12		28.30			48.62	
30.10	1.98		30.10	1.26		50.42	4.81
31.90	5.18		31.90	3.45		52.22	4.37
33.70	10.56		33.70	6.90		54.02	3.82
35.50	10.36		35.50	8.18		55.82	3.25
37.30	10.36		37.30	9.79		57.62	3.07

Table B3-7. (a) Surface Pressure, Wedge Angle = 11^0

X, cm	p/p_∞		X, cm	p/p_∞
16.12	1.040		31.36	21.420
17.12	1.068		32.36	20.325
18.12	1.302		33.36	18.136
19.11	1.635		34.35	16.104
20.11	1.968		35.35	14.024
21.14	2.381		36.38	12.336
22.12	2.984		37.36	10.819
23.12	3.825		38.36	9.600
24.12	4.952		39.36	8.599
25.12			40.36	
26.12	8.746		41.36	6.957
27.12	11.016		42.36	6.379
28.11	13.270		43.35	5.863
29.11	15.524		44.35	5.410
30.11	17.937		45.35	5.019
31.11	19.683		46.35	4.784
32.11	19.365		47.35	4.346

Table B3-7. (b) Surface Heat Transfer, Wedge Angle = 11^0

Thermocouples

X, cm	Q/Q_∞		X, cm	Q/Q_∞
16.12	1.06		31.36	13.77
17.10	1.03		32.34	13.13
18.11	1.02		33.35	11.85
19.09	0.90		34.33	10.22
20.05	0.96		35.29	9.08
21.04	1.34		36.28	8.37
22.04	1.88		37.28	7.39
23.05	2.68		38.29	6.62
25.07	5.96		40.31	5.31
26.07	7.95		41.31	4.90
27.07	9.08		42.31	4.30
29.33	11.66		44.57	3.64
30.08	11.96		45.32	3.27
32.12	12.17		47.36	2.89

Schmidt-Boelter gauges

X, cm	Q/Q_∞		X, cm	Q/Q_∞
16.02	1.06		31.26	12.27
17.82	0.92		33.06	10.61
19.62	0.00		34.86	6.49
21.42	1.29		36.66	6.95
23.22	2.80		38.46	0.00
25.02	5.44		40.26	5.33
26.82	8.26		42.06	4.56
28.62	9.69		43.86	2.60
30.42	10.74		45.66	3.44
32.22	11.45		47.46	4.62

Baseline Computations. A single baseline computation is provided for the 100 case to facilitate and gage new code development and turbulence model improvements. This computation was previously obtained and published by NASA during the uncertainty assessment related to hypersonic SWBLI simulations. See Ref. B3-3.

DPLR solutions were accomplished with a 5-block grid (4 blocks having 96x3x128 cells each, and one block of 192x3x32), with $y_1^+ \cong 0.15$. Transition was set at $x_{tr} \cong 0.4$ meters from the flat plate leading edge. This is somewhat upstream of the cited experimental transition ($0.5 < x_{tr} < 1.0$ meters), but yielded improved agreement as to the boundary layer properties immediately upstream of the interaction. The total enthalpy for this experiment is well below that required for dissociation and the dry air working fluid is treated as a perfect gas. Keyes dynamic viscosity equation for dry air is used due to the low free-stream temperature. Fig. B3-2 provides comparison of the computed boundary layer with measured data for velocity and temperature through the boundary layer on the test surface upstream of the interaction at $X \cong 187$ cm past the shock generator leading edge. Fig. B3-3 and B3-4 compare computed results for several turbulence models with experimental measurements for the wall pressure and wall heat transfer as normalized by the upstream boundary layer values of $P_\infty = 430$ Pa, and $Q_\infty = 10.4$ W/cm^2. The reader can refer to Ref. B3-3 for details on implementation of various production term options in DPLR. The interaction does not develop a plateau region of constant pressure post-reattachment, likely due to the short length of the shock generator. Brown, Ref B3-3, suggests for this flow that the expansion fan off the trailing edge of the shock generator prematurely terminates the full development of the interaction in the post-reattachment region. For a more complete discussion, see Ref. B3-3.

DPLR grids and input decks, showing modeling options, for the 10^0 case are included in the companion DVD.

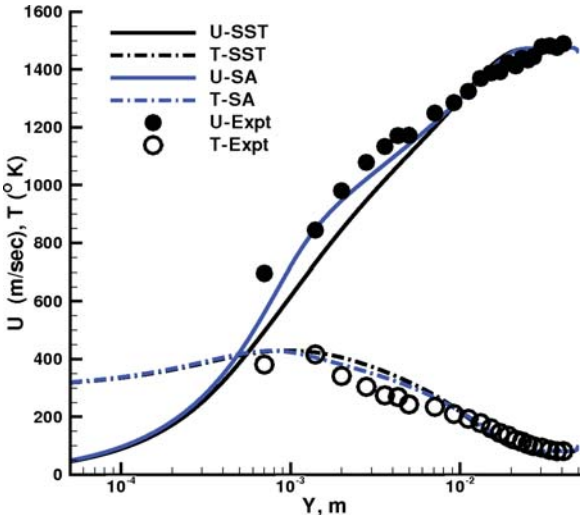

Figure B3-2. Kussoy 10° Upstream Boundary Layer.

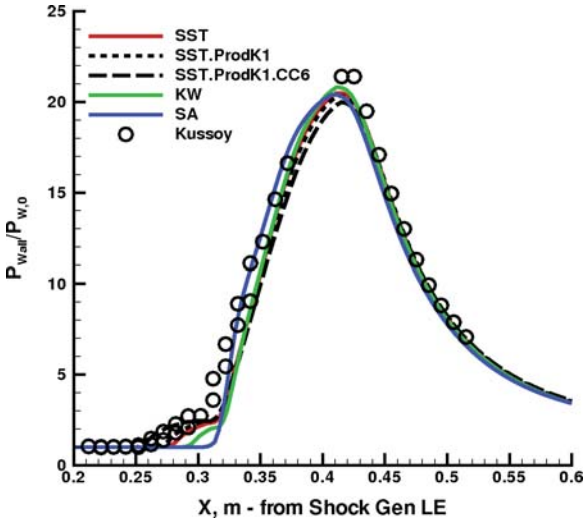

Figure B3-3. Kussoy 10° Wall Pressure.

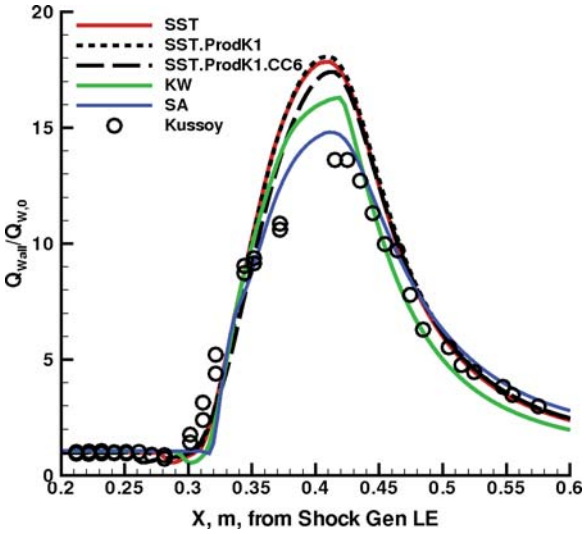

Figure B3-4. Kussoy 10° Wall Heating.

B4. Holden, et al. – 2D Impinging Shock

Ref. B4-1. Holden, M., MacLean, M., Wadhams, T. and Mundy, E., "Experimental Studies of Shock Wave/Turbulent Boundary Layer Interaction in High Reynolds Number Supersonic and Hypersonic Flows to Evaluate the Performance of CFD Codes", AIAA Paper 2010-4468, 40th Fluid Dynamics Conference and Exhibit, Chicago, Illinois, June 28 – July 1, 2010.

Ref. B4-2. Anon, "Large Energy National Shock Tunnel (LENS)", CALSPAN-UB Research Center, Accession no 5690, Dec. 1, 1990.

Ref. B4-3. Gnoffo, P.A., Berry, S.A. and Van Norman, J.W. "Uncertainty Assessments of 2D and Axisymmetric Hypersonic Shock Wave – Turbulent Boundary Layer Interaction Simulations at Compression Corners", AIAA Paper 2011-3142, 42nd AIAA Thermophysics Conference, Honolulu, Hawaii, June 27-30, 2011.

Ref. B4-4. Brown, J.L., "Shock Wave Impingement on Boundary Layers at Hypersonic Speeds: Computational Analysis and Uncertainty", AIAA Paper 2011-3143, 42nd AIAA Thermophysics Conference, Honolulu, Hawaii, June 27-30, 2011.

General description. Holden provided NASA reexamined data for an impinging shock experiment that was a separated flow case. The tests were performed at a nominal Mach number of 11 and at high Reynolds numbers resulting in very substantial length of naturally developing turbulent boundary layer flow ahead of the interaction region. The experiments were performed in air in the CUBRC shock tunnel complex described in Ref's. B4-1 and B4-2. Other data for various angles were reported elsewhere, but not provided herein. The shock angle of incidence was sufficient to cause separation in the interaction zone.

Experimental arrangement. The impinging shock experimental arrangement is shown below. The 20^0 -wedge shock generator was positioned above the plate and it generated a region of separated flow in the interaction zone.

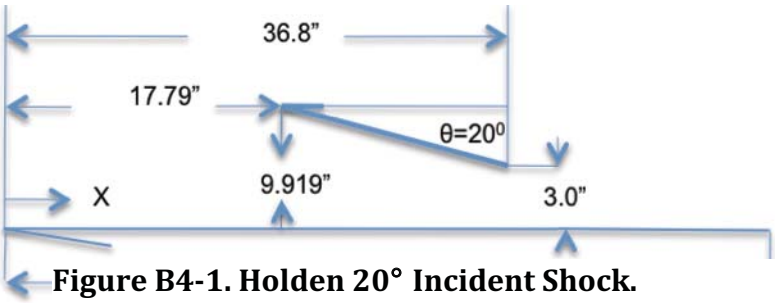

Figure B4-1. Holden 20° Incident Shock.

Facility. The experimental data were obtained in the CUBRC shock tunnel facilities. See Ref. B4-1 and Appendix A2 for more description details.

Measurements. The plate was instrumented with piezoelectric pressure gages, thin film heat transfer gages and floating balance piezoelectric skin friction gages. Surface pressures, heat transfer and skin friction were reported and are given in Table B4-2 below. Accuracy of the pressure measurements was estimated as $\pm$ 3%, heat transfer as $\pm$ 5%, and skin friction between $\pm$ 7 to $\pm$12%. (See Refs. B4-1 and B4-3.)

Test conditions were M=11.4, ρ_∞= .08910 kg/m^3, T_∞= 63^{0}K, and U_∞=1814 m/s. Wall temperature was 300^{0}K. Free stream dynamic pressure and stagnation enthalpy were accurate to $\pm$ 5% and Mach number to $\pm$ 1.5%. Measured separation for this case was X~34.80 in., based on interpolation of the wall shear stress data.

Working fluid for this experiment was dry Air.

Data tables. The data were published in Ref. B4-1 and recommended to NASA for their uncertainty studies. X is from the leading edge of the test flat plate.

Table B4-1- Holden 20^0 Incident Shock (Run 49, Mach=11.4), Wall Pressures.

X, in	P, psia		X, in	P, psia
32.53	0.241		43.02	29.40
35.02	0.323		43.67	21.50
36.72	1.35		44.31	16.40
37.31	1.25		44.94	12.20
37.75	5.26		45.59	9.33
38.27	17.50		46.22	7.72
38.82	21.90		47.50	4.81
39.56	27.20		48.79	3.96
41.78	26.80		50.07	2.89
42.38	27.10		51.36	1.87

Table B4-2- Holden 20^0 Incident Shock (Run 49, Mach=11.4), Wall Heat Transfer.

X, in	Qw, Btu/ft²-sec		X, in	Qw, Btu/ft²-sec		X, in	Qw, Btu/ft²-sec
32.52	5.16		39.13	254.00		43.02	190.00
34.02	5.04		39.28	248.00		43.67	148.00
35.04	4.25		39.42	254.00		44.31	126.00
35.93	10.00		39.59	221.00		44.94	87.80
36.13	11.10		39.68	235.00		45.59	70.90
36.48	13.20		39.89	233.00		46.22	58.70
36.69	13.60		40.36	214.00		46.87	50.30
37.56	30.40		40.56	201.00		47.50	40.60
37.76	50.00		41.01	197.00		48.79	35.60
38.08	92.40		41.66	196.00		50.07	23.60
38.61	220.00		41.85	186.00		51.36	16.80
38.82	218.00		42.50	189.00			

Table B4-2- Holden 20^0 Incident Shock (Run 49, Mach=11.4), Wall Shear Stress.

X, in	τ_w, psi
32.53	0.00662
36.72	-0.00562
37.21	-0.00481
37.75	-0.05000
38.27	-0.01550
39.56	0.400
40.48	0.485
42.39	0.413
45.27	0.181
47.19	0.127

Baseline Computations. Computations follow that provide a baseline for those wanting to compute the experiments documented above. The baseline is intended to facilitate and gage new code development and turbulence model improvements. The DPLR solutions provided in this section have not been published previously. They are based on the 'standard' SST and KW model implementations described in Ref. B4-4. Similar solutions, using a modified SST model are provided by MacLean in Ref. B4-1.

DPLR solutions for the 20^0 case were accomplished with a 4-block grid (3 blocks having 512x3x512 cells each, and one block of 512x3x64), with $y_1^+ \cong 0.05$. Transition was set to occur over the interval of $x_{tr} \cong 0.2$-0.38 meters (8-16 inches) from the flat plate leading edge, in the simulations, based on flat plate data at similar conditions, with $Re\Theta$ for transition in the range 800-1000. The total enthalpy for this experiment is below that required for dissociation and the dry air working fluid is treated as a perfect gas. Keyes dynamic viscosity equation for dry air is used due to the low free-stream temperature.

Figs. B4-2, B4-3 and B4-4 compare computed results for the 'standard' (see Ref B4-4) version of the SST and KW turbulence models with experimental measurements for the wall pressure, wall heat transfer and wall shear stress. The data in these figures are converted to metric units to conform to the DPLR solution output. The interaction does not develop a plateau region of constant pressure post-reattachment, likely due to the short length of the shock generator. Brown, Ref B4-4, suggests for this type of impinging shock flow that the expansion fan off the trailing edge of the shock generator prematurely terminates the full development of the interaction in the post-reattachment region. In this, the Holden impinging shock experiment is similar to the experiments of Kussoy and of Murray, but differs with the long-generator Schülein experiment, which does exhibit full development of the interaction region with attendant constant pressure plateau in the post-reattachment region. For a more complete discussion, see Ref. B4-4.

DPLR grids and input decks, showing modeling options, for the 20^0 case are included in the companion DVD.

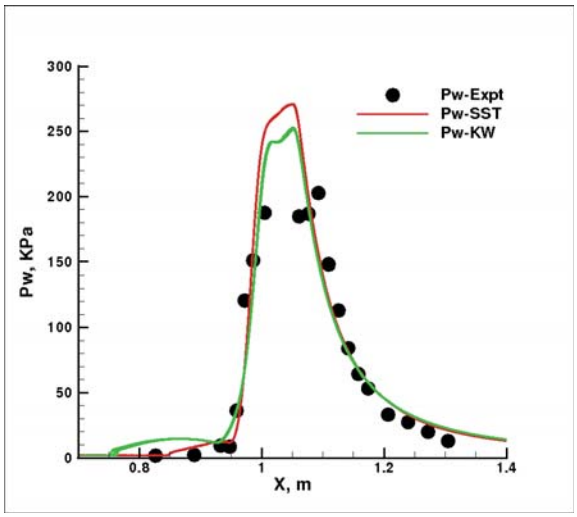

Figure B4-2. Holden 20° Wall Pressure.

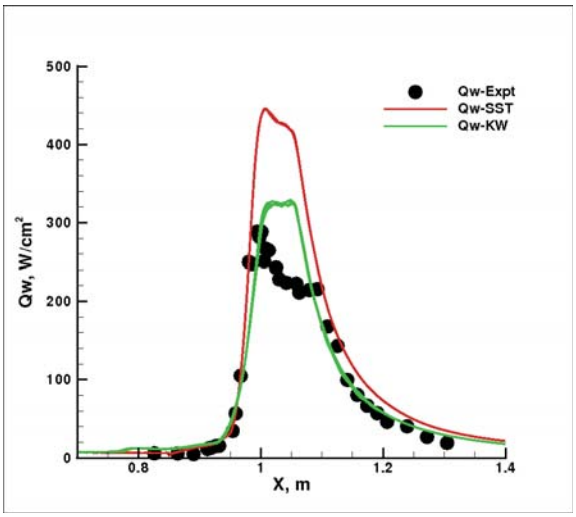

Figure B4-3. Holden 20° Wall Heating.

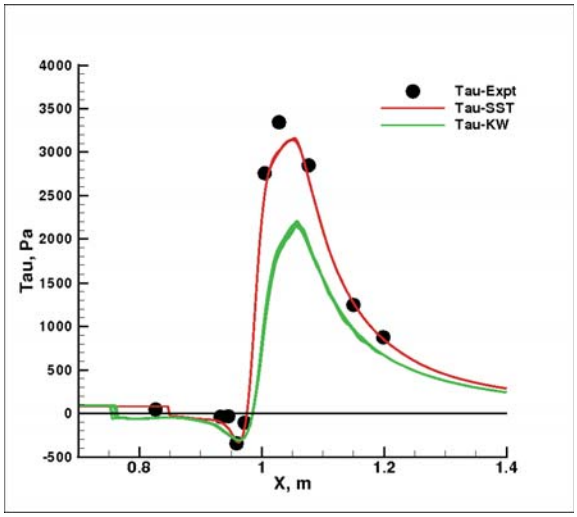

Figure B4-4. Holden 20° Wall Shear Stress.